



**INFLUENCE OF MACH NUMBER AND DYNAMIC PRESSURE ON CAVITY  
TONES AND FREEDROP TRAJECTORIES**

THESIS

Justin D. Merrick, Second Lieutenant, USAF

AFIT-ENY-14-M-36

**DEPARTMENT OF THE AIR FORCE  
AIR UNIVERSITY**

***AIR FORCE INSTITUTE OF TECHNOLOGY***

**Wright-Patterson Air Force Base, Ohio**

DISTRIBUTION STATEMENT A:  
APPROVED FOR PUBLIC RELEASE; DISTRIBUTION UNLIMITED

The views expressed in this thesis are those of the author and do not reflect the official policy or position of the United States Air Force, the Department of Defense, or the United States Government.

This material is declared a work of the U.S. Government and is not subject to copyright protection in the United States.

AFIT-ENY-14-M-36

INFLUENCE OF MACH NUMBER AND DYNAMIC PRESSURE ON CAVITY  
TONES AND FREEDROP TRAJECTORIES

THESIS

Presented to the Faculty  
Department of Aeronautical and Astronautical Engineering  
Graduate School of Engineering and Management  
Air Force Institute of Technology  
Air University  
Air Education and Training Command  
in Partial Fulfillment of the Requirements for the  
Degree of Master of Science in Aeronautical Engineering

Justin D. Merrick, B.S.A.E.  
Second Lieutenant, USAF

March 2014

DISTRIBUTION STATEMENT A:  
APPROVED FOR PUBLIC RELEASE; DISTRIBUTION UNLIMITED

INFLUENCE OF MACH NUMBER AND DYNAMIC PRESSURE ON CAVITY  
TONES AND FREEDROP TRAJECTORIES

Justin D. Merrick, B.S.A.E.  
Second Lieutenant, USAF

Approved:

\_\_\_\_\_  
//signed//  
Mark F. Reeder, PhD (Chairman)

\_\_\_\_\_  
12 Mar 2014  
Date

\_\_\_\_\_  
//signed//  
Capt Christopher L. Martin, PhD (Member)

\_\_\_\_\_  
12 Mar 2014  
Date

\_\_\_\_\_  
//signed//  
Maj James Rutledge, PhD (Member)

\_\_\_\_\_  
12 Mar 2014  
Date



**Abstract**

Weapons release at supersonic speeds from an internal weapons bay is a highly desirable capability. To ensure a successful release at multiple Mach numbers, the aerodynamic environment must be well-understood and repeatable, with a robust system for safe testing of store separation. For this reason, experimental methods were used to investigate the characteristics of a scaled WICS bay with a length-to-depth ratio of 4.5 at multiple Mach numbers and stagnation pressures. Three new nozzles were designed, manufactured, and characterized for the AFIT small supersonic tunnel, yielding freestream Mach numbers of 2.22, 1.84, and 1.43. In addition, a control valve was reconfigured to achieve stagnation pressures as low as 1.0 psia. These nozzles were then used in conjunction with piezoresistive pressure transducers and high-speed Schlieren photography to capture the time-varying pressure signal and spectra of the cavity. Resonant frequencies from these tests matched very well with analytically predicted results for the Mach 2.3 and Mach 1.9 nozzles. The Mach 1.5 nozzle posed some difficulties for the configuration tested due to shocks reflecting into the cavity. The Mach 2.3 nozzle was utilized in freedrop testing of a 1:20 scaled sphere and compared to computational simulations. The computational solution was obtained using the OVERFLOW solver with incorporated 6DOF motion and the DDES/SST hybrid turbulence model. Analysis of the Schlieren video generated by the experimental tests allowed direct comparison of computational and experimental trajectories. Measured trajectories compared closely to computational trajectories, especially for the lowest stagnation pressure settings, where heavy Mach scaling yielded operationally relevant results, despite the small scale of the tests.

## **Acknowledgements**

First, I'd like to thank my research advisor, Dr. Mark Reeder, for his guidance and support. Whether by countering my naivete with realistic expectations, maintaining an unquenchable optimism when waiting for parts, or putting aside his work at a moment's notice to assist in problem-solving, without his untiring efforts, this thesis would not have been possible. I would also like to thank Rudy Johnson from the Air Force Research Laboratory for his help in framing the scope of this research.

I would like to thank Chris Zickefoose, Wilbur Lacy, John Hixenbaugh, and the laboratory support staff for their assistance throughout the experimental stage of my research. Their technical expertise was invaluable.

I would like to thank Brian Crabtree and Chris Harkless of the AFIT model shop, without whom my research would never have gotten off the ground. Their dedication to precision and timeliness is without peer.

I would like to thank Captain Chris Martin, Major Darrell Crowe, and Mr. Dave Doak for their efforts in helping me complete the computational stage of my research. I would also like to thank Dr. Robert Nichols of the University of Alabama-Birmingham and Lieutenant Commander Thomas Flora. Without their previous efforts, the computational portion of my research would not have gotten off the ground.

Finally, I would like to thank the friends, family, and colleagues who took time from their busy schedules to help me improve the quality of this research.

Justin D. Merrick

## Table of Contents

	Page
Abstract . . . . .	iv
Acknowledgements . . . . .	v
Table of Contents . . . . .	vi
List of Figures . . . . .	ix
List of Tables . . . . .	xiii
List of Abbreviations . . . . .	xv
List of Symbols . . . . .	xvi
 I. Introduction . . . . .	 1
1.1 Motivation . . . . .	1
1.1.1 Advantages of Internal Stores . . . . .	1
1.1.2 Disadvantages of Internal Stores . . . . .	2
1.2 Problem Statement . . . . .	3
1.3 Research Objectives . . . . .	3
 II. Background . . . . .	 5
2.1 Cavity Flow . . . . .	5
2.2 Scaling Laws . . . . .	7
2.2.1 Froude Scaling . . . . .	9
2.2.2 Heavy Mach Scaling . . . . .	10
2.2.3 Light Mach Scaling . . . . .	11
2.3 Store Separation . . . . .	12
2.4 Computational Analysis of Cavity Flows and Store Separation . . . . .	14
2.4.1 Turbulence Modeling in Cavity Flows . . . . .	15
2.4.2 Overset Grid Techniques . . . . .	16
2.4.3 OVERFLOW Solver . . . . .	18
 III. Methodology . . . . .	 21
3.1 Experimental Setup . . . . .	21

	Page
3.1.1 Supersonic Variable-Density Blowdown Tunnel . . . . .	21
3.1.2 Faceplate . . . . .	23
3.1.3 Regulating Valve . . . . .	24
3.1.4 Nozzle Block . . . . .	25
3.1.5 Test Section and Cavity . . . . .	30
3.1.6 Data Acquisition . . . . .	35
3.2 Experimental Methodology . . . . .	36
3.2.1 Procedures . . . . .	36
3.2.2 Data Reduction . . . . .	38
3.3 Computational Methodology . . . . .	42
3.3.1 Grid Generation . . . . .	42
3.3.2 Boundary Conditions . . . . .	43
3.3.3 Initial Conditions . . . . .	47
IV. Results . . . . .	50
4.1 Nozzle Characterization . . . . .	50
4.1.1 Mach 3.0 . . . . .	50
4.1.2 Mach 2.3 . . . . .	53
4.1.3 Mach 1.9 . . . . .	56
4.1.4 Mach 1.5 . . . . .	58
4.2 Cavity Environment . . . . .	63
4.2.1 Mach 3.0 . . . . .	63
4.2.2 Mach 2.3 . . . . .	66
4.2.3 Mach 1.9 . . . . .	70
4.2.4 Mach 1.5 . . . . .	72
4.3 Drop Testing . . . . .	75
4.3.1 Experimental . . . . .	75
4.3.2 Computational . . . . .	83
4.3.3 Trajectory Comparison . . . . .	88
4.3.4 Heavy Mach Scaling . . . . .	89
V. Conclusions . . . . .	93
5.1 Nozzle and Cavity Characterization . . . . .	93
5.2 Store Separation . . . . .	95
5.3 Future Opportunities . . . . .	97
Appendix A: Nozzle Design Code . . . . .	99
Appendix B: Transducer Calibrations . . . . .	104

	Page
Appendix C: Flow Conditions Code . . . . .	107
Appendix D: Rossiter Modes Code . . . . .	109
Appendix E: Boundary Layer Code . . . . .	110
Appendix F: Rossiter Mode Results . . . . .	112
Appendix G: Detailed Drawings of Nozzle Blocks . . . . .	117
Appendix H: Trajectory Plotting Code . . . . .	123
Appendix I: Heavy Mach Scaling Codes . . . . .	127
Appendix J: Cavity Analysis Code . . . . .	133
Bibliography . . . . .	137

## List of Figures

Figure	Page
2.1 Generic rectangular cavity with important geometric features labeled . . . . .	5
2.2 Store axis system . . . . .	8
2.3 Example of Pitch Bifurcation . . . . .	14
3.1 Key components of AFIT SVDB wind tunnel (Not to scale; some detail not shown) . . . . .	21
3.2 Low stagnation pressure setup . . . . .	25
3.3 Multiple views of the assembled Mach 1.5 nozzle block . . . . .	29
3.4 Multiple views of the assembled Mach 1.9 nozzle block . . . . .	29
3.5 Multiple views of the assembled Mach 2.3 nozzle block . . . . .	30
3.6 Two views of the test section . . . . .	31
3.7 Location of Transducer Mounts in Cavity [1] . . . . .	32
3.8 Two views of the fill block outside the tunnel (flow from left) . . . . .	33
3.9 Two views of the fill block installed in the test section . . . . .	34
3.10 Release mechanism in the open and closed positions . . . . .	35
3.11 Boundary Layer Thickness Parameter vs. Mach number, reprinted from Rogers and Davis [2] . . . . .	41
3.12 Computational Domain with detail showing <i>Bay</i> , <i>Yin</i> , and <i>Yang</i> grids . . . . .	44
3.13 Boundary Condition Locations of <i>Plate</i> Grid . . . . .	45
3.14 Line of interest for BC201 boundary condition . . . . .	46
3.15 Residuals during ramp down from Mach 3.0 to Mach 2.22 . . . . .	48
4.1 Normalized PDF of Mach 3 Nozzle Tests . . . . .	52
4.2 Qualitative determination of Mach number for Mach 3 nozzle using Schlieren photography . . . . .	52

Figure	Page
4.3 Normalized PDF of Mach 2.3 Nozzle Tests . . . . .	54
4.4 Qualitative determination of Mach number for Mach 2.3 nozzle using Schlieren photography . . . . .	55
4.5 Qualitative Boundary Layer Estimation for Mach 2.22 . . . . .	55
4.6 Normalized PDF of Mach 1.9 Nozzle Tests . . . . .	57
4.7 Qualitative determination of Mach number for Mach 1.9 nozzle using Schlieren photography . . . . .	58
4.8 Qualitative Boundary Layer Estimation for Mach 1.84 . . . . .	58
4.9 Normalized PDF of Mach 1.5 Nozzle Tests . . . . .	60
4.10 Time History of Mach number for $P_0 = 6psi$ . . . . .	61
4.11 Normal Shock across static port for Mach 1.5 nozzle at $P_0 = 6psi$ . . . . .	61
4.12 Qualitative Boundary Layer Estimation for Mach 1.43 . . . . .	62
4.13 Cavity Spectra for all Mach 2.96 Tests . . . . .	64
4.14 Rossiter modes for individual Mach 2.96 Tests . . . . .	65
4.15 Cavity Spectra for all Mach 2.22 Tests . . . . .	67
4.16 Rossiter modes for individual Mach 2.22 Tests . . . . .	68
4.17 Cavity Spectra for all Mach 1.84 Tests . . . . .	70
4.18 Rossiter modes for individual Mach 1.84 Tests . . . . .	71
4.19 Cavity Spectra for all Mach 1.43 Tests . . . . .	73
4.20 Rossiter modes for individual Mach 1.43 Tests . . . . .	74
4.21 X-Z Plane Trajectory for Test 5 ( $P_t = 3.73$ ) . . . . .	78
4.22 X-Z Plane Trajectory for Test 6 ( $P_t = 3.68$ ) . . . . .	78
4.23 X-Z Plane Trajectory for Test 13 ( $P_t = 1.45$ ) . . . . .	78
4.24 X-Z Plane Trajectory for Test 15 ( $P_t = 1.12$ ) . . . . .	79
4.25 X-Z Plane Trajectory for Test 18 ( $P_t = 1.05$ ) . . . . .	79

Figure	Page
4.26 X-Z Plane Trajectory for Test 19 ( $P_t = 0.93$ ) . . . . .	80
4.27 X-Z Plane Trajectory for Test 22 ( $P_t = 1.00$ ) . . . . .	80
4.28 X-Z Plane Trajectory for Test 23 ( $P_t = 0.75$ ) . . . . .	81
4.29 X-Z Plane Trajectory for Test 24 ( $P_t = 1.22$ ) . . . . .	81
4.30 X-Z Plane Trajectory for Test 25 ( $P_t = 1.21$ ) . . . . .	82
4.31 Bow shock on the lower half of a sphere . . . . .	82
4.32 Computational X-Z Plane Trajectory at $P_t = 3.5$ . . . . .	83
4.33 Computational X-Z Plane Trajectory at $P_t = 2.0$ . . . . .	84
4.34 Computational X-Z Plane Trajectory at $P_t = 1.0$ . . . . .	84
4.35 Computational Z-Trajectory vs. time . . . . .	85
4.36 Residuals of $P_t = 3.5$ Computational Run . . . . .	86
4.37 Residuals of $P_t = 2.0$ Computational Run . . . . .	86
4.38 Residuals of $P_t = 1.0$ Computational Run . . . . .	87
4.39 Comparison of Computational and Experimental Trajectories for $P_t = 3.5$ . . .	88
4.40 Comparison of Computational and Experimental Trajectories for $P_t = 1.0$ . . .	89
B.1 1-1: Cavity Front . . . . .	104
B.2 1-2: Low Pressure Diaphragm Setup . . . . .	104
B.3 1-3: Stagnation Chamber . . . . .	105
B.4 2-1: Vacuum Valve . . . . .	105
B.5 2-2: Cavity Back Wall . . . . .	106
B.6 2-3: High Pressure Diaphragm Setup . . . . .	106
G.1 Representative Drawing of Nozzle Block from Multiple Views (Mach 1.5) . . .	118
G.2 Drawing of Mach 1.5 Nozzle Contour . . . . .	119
G.3 Drawing of Mach 1.9 Nozzle Contour . . . . .	120
G.4 Drawing of Mach 2.3 Nozzle Contour . . . . .	121



Figure	Page
G.5 Representative Drawing of Nozzle Sidewall (Mach 2.3) . . . . .	122

## List of Tables

Table	Page
3.1 Mach Number Correlations for Isentropic Air . . . . .	27
3.2 Computational Domain Information . . . . .	43
3.3 <i>Plate</i> grid Boundary Conditions . . . . .	46
3.4 OVERFLOW Solver Settings . . . . .	48
3.5 Initial Flow Parameters . . . . .	49
3.6 Non-dimensional Mass Properties . . . . .	49
4.1 Flow properties for Mach 3 Nozzle Experiments . . . . .	51
4.2 Flow properties for Mach 2.3 Nozzle Experiments . . . . .	54
4.3 Flow properties for Mach 1.9 Nozzle Experiments . . . . .	56
4.4 Flow properties for Mach 1.5 Nozzle Experiments . . . . .	59
4.5 Flow Conditions for Mach 2.96 Cavity Tests . . . . .	64
4.6 Average Difference per Rossiter Mode for Mach 2.96 . . . . .	66
4.7 Flow Conditions for Mach 2.22 Cavity Tests . . . . .	67
4.8 Average Difference per Rossiter Mode for Mach 2.22 . . . . .	69
4.9 Flow Conditions for Mach 1.84 Cavity Tests . . . . .	72
4.10 Average Difference per Rossiter Mode for Mach 1.84 . . . . .	72
4.11 Flow Conditions for Mach 1.43 Cavity Tests . . . . .	73
4.12 Average Difference per Rossiter Mode for Mach 1.43 . . . . .	75
4.13 Flow Conditions for Sphere Drop Tests . . . . .	76
4.14 Sphere Heavy Mach Scaling. $M=2.22$ , $h=10,000$ ft, $1/20$ scale . . . . .	90
4.15 Sphere Heavy Mach Scaling. $M=2.22$ , $h=20,000$ ft, $1/20$ scale . . . . .	91
4.16 Sphere Heavy Mach Scaling. $M=2.22$ , $h=30,000$ ft, $1/20$ scale . . . . .	92
F.1 Comparison of Observed and Predicted Rossiter Modes for Mach 2.96 . . . . .	112

Table	Page
F.2 Comparison of Observed and Predicted Rossiter Modes for Mach 2.22 . . . . .	113
F.3 Comparison of Observed and Predicted Rossiter Modes for Mach 1.84 . . . . .	115
F.4 Comparison of Observed and Predicted Rossiter Modes for Mach 1.43 . . . . .	116

## List of Abbreviations

Abbreviation	Page
CFD	Computational Fluid Dynamics . . . . . 15
DNS	Direct Numerical Simulation . . . . . 15
RANS	Reynolds-Averaged Navier-Stokes . . . . . 16
LES	Large-Eddy Simulation . . . . . 16
DES	Detached Eddy Simulation . . . . . 16
SPL	Sound Pressure Level . . . . . 16
SA	Spalart-Almaras . . . . . 16
SST	Shear Stress Transport . . . . . 16
DDES	Delayed Detached Eddy Simulation . . . . . 16
6DOF	six degree-of-freedom . . . . . 18
ADI	Alternating Direction Implicit . . . . . 18
LU-SGS	Lower Upper-Symmetric Gauss Seidel . . . . . 18
SSOR	Successive Symmetric Over-Relaxation . . . . . 18
SVDB	Supersonic Variable-Density Blowdown . . . . . 21
AFRL	Air Force Research Laboratory . . . . . 28
TGF	Trisonic Gas Facility . . . . . 28
WICS	Weapons Internal Carriage and Separation . . . . . 30
RP	Rapid Prototyping . . . . . 32
CSV	Comma Separated Value . . . . . 42
PDF	Probability Density Function . . . . . 51

## List of Symbols

Symbol	Page
$()'$	Fluctuating flow quantity . . . . . 16
$()'$	sub-scale parameter . . . . . 10
$()^*$	non-dimensional quantity . . . . . 20
$()_t$	Total quantity . . . . . 40
$()_\infty$	freestream quantity . . . . . 8
$()_{ref}$	reference quantity for non-dimensionalization . . . . . 20
$A$	Area of a 2D nozzle . . . . . 26
$A^*$	Area of the throat of a 2D nozzle . . . . . 26
$C_A$	store axial-force coefficient . . . . . 8
$C_N$	store normal-force coefficient . . . . . 8
$C_m$	store pitching-moment coefficient . . . . . 8
$C_{m_q}$	store pitch damping derivative . . . . . 8
$F_{EJ}$	ejector force . . . . . 8
$I$	store moment of inertia in the pitch plane . . . . . 8
$I_{chim}$	chimera array . . . . . 19
$L$	cavity length (ft) . . . . . 7
$L/D$	cavity length to depth ratio . . . . . 5
$M$	Mach Number . . . . . 26
$M_\infty$	freestream Mach number . . . . . 7
$R_{air}$	Ideal gas constant for air . . . . . 40
$Re$	Reynolds number . . . . . 40
$S$	store reference area . . . . . 8
$Str$	Strouhal number . . . . . 7

$T$	Temperature . . . . .	40
$U_{\infty}$	freestream streamwise velocity (ft/s) . . . . .	7
$V$	velocity . . . . .	8
$\Delta\tau$	pseudo-time . . . . .	19
$\Theta$	Expansion Angle . . . . .	27
$\beta$	phase delay constant . . . . .	7
$\ddot{()}$	second derivative with respect to time (acceleration) . . . . .	8
$\dot{()}$	first derivative with respect to time (velocity) . . . . .	8
$\frac{D[.]}{Dt}$	Material Derivative . . . . .	8
$\gamma$	Ratio of Specific Heats . . . . .	26
$\lambda$	model scale factor . . . . .	10
$\mu$	viscosity . . . . .	8
$\nu$	Prandtl Angle . . . . .	27
$\nu$	ratio of velocities $V'_{\infty}/V_{\infty}$ . . . . .	10
$\overline{()}$	Mean flow quantity . . . . .	16
$\rho$	density . . . . .	10
$\sigma$	ratio of densities $\rho'_{\infty}/\rho_{\infty}$ . . . . .	10
$\theta$	store pitch-attitude . . . . .	8
$\vec{E}, \vec{F}, \vec{G}$	flux vectors . . . . .	19
$\vec{q}$	vector of conserved variables . . . . .	19
$\zeta, \eta, \xi$	computational space coordinates . . . . .	19
$a$	Speed of sound . . . . .	40
$d$	store reference diameter . . . . .	8
$e_0$	total energy . . . . .	19
$f$	modal frequency (Hz) . . . . .	7
$g$	acceleration due to gravity . . . . .	8

$k_c$	convection velocity ratio $\left(\frac{U_c}{U_\infty}\right)$ . . . . .	7
$m$	store mass . . . . .	8
$n$	mode number . . . . .	7
$p, P$	pressure . . . . .	8
$q_\infty$	freestream dynamic pressure . . . . .	8
$t$	time . . . . .	19
$u, v, w$	velocity components . . . . .	8
$x, y, z$	Cartesian space coordinates . . . . .	8
$x_{EJ}$	distance from store CG to line of action for ejector force . . . . .	8

# INFLUENCE OF MACH NUMBER AND DYNAMIC PRESSURE ON CAVITY TONES AND FREEDROP TRAJECTORIES

## I. Introduction

### 1.1 Motivation

Internal carriage of weapons began during World War I but was popularized in the United States by the Martin B-10. Since then, all of the United States' heavy bombers have had internal weapons carriage. As the manufacturing and design of weapons and aircraft improved, lighter aircraft have also been equipped with internal carriage capabilities. In 1977, Lockheed demonstrated the viability of a stealth aircraft with *Have Blue*, leading to the production of the F-117 Nighthawk. The F-117 became the first fighter with dedicated internal weapons bays. Since then, all new production stealth aircraft have had internal carriage of weapons, including the F-22 and F-35.

Many of the aircraft equipped with internal carriage, including the F-22 and B-1, have supersonic capabilities. However, current technology requires weapon releases to be conducted at transonic speeds or below due to the volatile nature of flow in and around weapons bays. This speed requirement causes a large increase in aircraft vulnerability. By understanding the phenomena present in cavity flows, engineering advances may be made that could potentially allow for the release of weapons at supersonic speeds. This "full envelope" release capability would drastically reduce the potential threat to US aircraft and crew and give the US a tactical advantage over adversaries.

#### *1.1.1 Advantages of Internal Stores.*

The internal carriage of stores provides an array of tactical and operational advantages to the warfighter. Initially, internal carriage was used for drag reduction purposes, allowing



aircraft like the B-10, and later many other bombers, to increase their range and cruising speed. While this trend of internal carriage has long been a staple of bomber design, only in the past few decades has it risen to prominence among fighter aircraft. Internal carriage is of great importance to a stealthy aircraft as the pylons, fins, guidance packages and weapon fuselages associated with external carriage all have a significant impact on the radar cross section of an aircraft. Additionally, the heating and aerodynamic loads associated with external weapons carriage at high speeds can damage weapons and equipment. These impacts are significant enough that all fifth generation US aircraft have internal weapons carriages.

### ***1.1.2 Disadvantages of Internal Stores.***

While internal carriage provides some significant benefits, there are some critical challenges as well. These difficulties include a weight and drag penalty, an acoustical resonance problem, as well as store separation difficulties. While the weight and drag penalty can be somewhat mitigated, the latter two problems are still a current area of investigation.

With external stores, the volume dedicated to the weapons is removed after the weapon is dropped. This results in a decrease in weight and frontal area when the stores separate from the aircraft. Internal stores see a similar reduction in weight but do not see the same decrease in frontal area due to the fixed volume of the weapons bay. This increased frontal area can be largely overcome by increases in thrust and by judicious placement of aircraft components [3].

Acoustical resonance in weapons bays is caused by the unique flowfield that flow past a cavity creates. This flowfield results in periodic, high-amplitude pressure waves that are detrimental to both weapon and cavity components. The fins and guidance packages utilized by precision guided weapons, as well as the pylons, hinges, and structural components of the weapons bay, can be sensitive to the unsteady forces produced by these

waves. Understanding the cause and effects of this phenomenon is of utmost importance to the effective carriage of modern weapons.

## **1.2 Problem Statement**

The growing number of airframes utilizing internal carriage of weapons and the trend of designing lighter and less stable weapons accentuates the unsteady and sometimes violent nature of cavity flows. Coupling this with supersonic speeds yields an environment that may be destructive and dangerous to weapons and airframes. Modeling this cavity correctly, in both computational and experimental configurations, is of vital importance to understanding the driving acoustic and aerodynamic processes and how to mitigate the effects of these processes. Scaled drop testing is a useful tool to determine the trajectory and pitch response of weapons in a frugal and easily iterated environment. However, it requires a balancing of aerodynamic and inertial forces that can be difficult to achieve.

Additionally, the varying capabilities of modern aircraft ensure that accurate modeling of weapons bays at varying supersonic speeds is an important piece of understanding the challenges that face potential full scale store separations. By accurately and repeatably producing multiple Mach numbers the acoustical phenomena of the cavity can be verified and scaled drop testing can be examined for a range of realistic speeds and operating conditions.

## **1.3 Research Objectives**

Previous research at AFIT has led to assessments of the dynamics of an inertially simple shape free-dropped from a cavity into Mach 3 flow through both experimental and computational techniques. Limits on tunnel performance forced some test points to be conducted only computationally and limited all supersonic tests to Mach 3 flow. The objective of this research is to expand the capabilities of the AFIT small supersonic wind tunnel through the fabrication and characterization of new supersonic nozzles for nominal

Mach numbers of 1.5, 1.9, and 2.3. Additionally, characterization of the acoustic cavity environment at these speeds will be conducted and compared against analytical predictions.

The secondary goal will be to utilize the capabilities gained through these tests into freedrop testing of an inertially simple shape, the sphere. A vacuum pump will be used in an attempt to scale dynamic pressures to the levels only attained computationally in prior testing. This drop testing will be conducted on one or more of the new nozzles and be complemented by computational analysis at the corresponding speed and dynamic pressures.

A tertiary goal uses the data gained by the experimental scaled drop testing to generate a two dimensional trajectory of the store flight in order to compare this data with the computational data. This will allow the two methods to be verified against each other and may provide insight on the strengths and weaknesses of each.

## II. Background

The problem of store separation from a cavity at supersonic speeds can be broken down into three main components. These are the cavity flow features, the scaling laws applicable to the store, and finally the correlation between these two separate disciplines within store separation.

### 2.1 Cavity Flow

The ratio of length to depth ( $L/D$ ) in a cavity is the primary differentiator characterizing cavity flows. The length is measured from the leading edge to the trailing edge of the cavity. The depth is measured from the cavity floor (or ceiling) to the freestream flow. Figure 2.1 shows a generic rectangular cavity with geometric features labeled. The  $L/D$  is important because it determines the basic flow structure within the cavity. A deep cavity is one in which the  $L/D < 1$  while a shallow cavity is one in which the  $L/D > 1$  [4]. Similarly a cavity may be open, closed, or transitional. An open cavity is one in which  $L/D < 10$  while a closed cavity is one in which  $L/D > 13$ . A transitional cavity occupies the space between the two,  $10 < L/D < 13$  [5]. Typically, weapons bays are classified as shallow, open cavities and so the flow mechanics of this type of cavity is of special importance to this investigation.

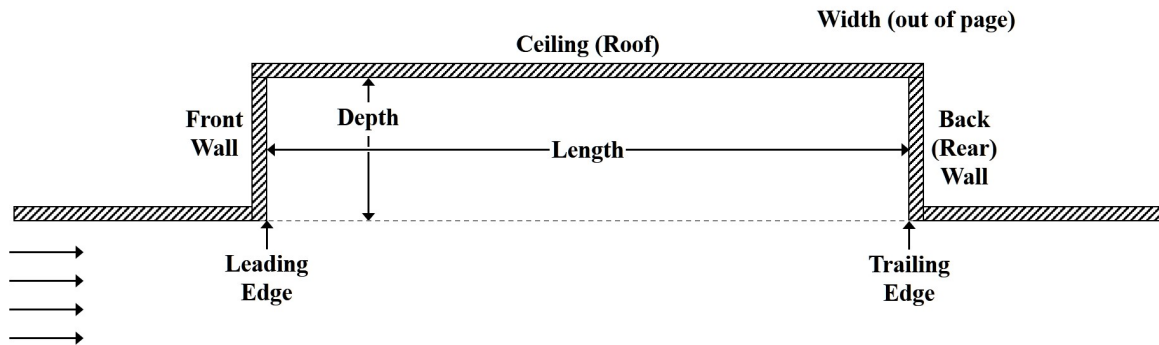


Figure 2.1: Generic rectangular cavity with important geometric features labeled

Cavity flows produce self-sustaining oscillations which can be categorized into three types: fluid-dynamic oscillations, fluid-resonant oscillations, and fluid-elastic oscillations. Rockwell and Naudascher [4] provides a thorough review of the three categories. For a weapons bay, fluid-resonant oscillations dominate the flow because the frequency of the oscillations corresponds to a wavelength smaller than the length of the bay. These oscillations are produced by a shear layer forming between the moving flow of the freestream and the relatively quiescent flow within the cavity. This free shear layer produces vortical structures, which grow with distance downstream, causing the shear layer to widen. When the shear layer reaches the trailing edge of the cavity, it has grown sufficiently to the point where the vortical structures impinge upon the back wall of the cavity, leading to oscillations in the flow within the closed geometry of the cavity. This oscillation leads to changes in pressure consistent with the frequency of the impingement of the vortical structures. This pressure wave then propagates upstream in the low speed environment of the cavity, forcing the initial instabilities of the shear layer to correspond with the downstream vortical structures. When the wave reaches the upstream edge of the cavity, it is reflected back downstream until it reaches the trailing edge once more. Here the mass is expelled and the pressure wave reflects back towards the leading edge of the cavity, again drawing mass into the cavity. The action of the pressure wave traveling through the cavity and the mass exchange at the trailing edge can be thought of as a feedback mechanism and is the primary source of the self-sustaining, highly periodic fluid-resonant oscillations [4, 6].

In shallow cavity flows, the oscillations caused by the feedback mechanism occur at multiple frequencies for a given Mach number. These frequencies are the Rossiter modes and can be predicted semi-empirically by Equation 2.1, Rossiter's original relationship between the Strouhal number and the freestream Mach number. To create this relationship, Rossiter assumed a constant temperature across the cavity and freestream. This limits the

range of Mach number range over which Equation 2.1 can accurately predict the frequency of oscillation. Heller, Holmes, and Covert [7] modified this relationship to account for the difference in temperature, and thus speed of sound, in the cavity and the freestream, yielding Equation 2.2. This equation yields accurate mode prediction through Mach 3. In both equations, the values of the constants are  $\beta = 0.25$  and  $k_c = 0.57$ . The value  $k_c = 0.57$  was assumed by Rossiter and determined to be appropriate for thin initial boundary layers, but should decrease as the thickness of the boundary layer increases. This value has been accepted to provide accurate results by multiple sources [7, 8]. After determining  $k_c$ , the phase constant  $\beta$  was found to correspond to a quarter of one vortex wavelength, leading to a value of 0.25, as noted above [8].

$$Str = \frac{fL}{U_\infty} = \frac{n - \beta}{M_\infty + \frac{1}{k_c}}, \quad n = 1, 2, 3... \quad (2.1)$$

$$Str = \frac{fL}{U_\infty} = \frac{n - \beta}{\frac{M_\infty}{\sqrt{1 + \frac{1}{2}(\gamma - 1)M_\infty^2}} + \frac{1}{k_c}}, \quad n = 1, 2, 3... \quad (2.2)$$

## 2.2 Scaling Laws

In freedrop testing, it is desirable to achieve similarity between the scaled model and a full size test article. Specifically, similarity of geometry, mass properties, physics, time, kinematics, and dynamics are desired. By applying non-dimensional analysis to the governing equations for store translation (Equation 2.3), rotation (Equation 2.4), and fluid flow in the longitudinal direction (Equation 2.5), in accordance with Figure 2.2, non-dimensional parameters emerge that provide similarity between full scale store testing and scaled model testing. These parameters are well known and include Mach number, Reynolds number, Strouhal number, Froude number, Euler number, Newton number, and the relative density [9, 10]. Unfortunately, it is impossible to match all of these conditions for total similarity. Instead, three scaling models have been developed which are considered

the best achievable compromise: Froude Scaling, Heavy Mach Scaling, and Light Mach Scaling [9].

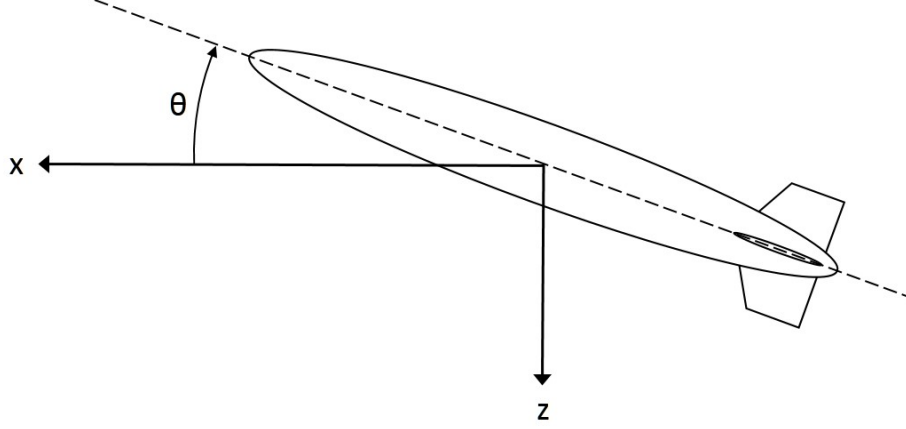


Figure 2.2: Store axis system

$$\ddot{x} = -[C_A \cos \theta + C_N \sin \theta] \frac{q_\infty S}{m} + \frac{F_{EJ}}{m} \sin \theta \quad (2.3a)$$

$$\ddot{z} = -[C_N \cos \theta - C_A \sin \theta] \frac{q_\infty S}{m} + \frac{F_{EJ}}{m} \cos \theta + g \quad (2.3b)$$

$$\ddot{\theta} = \left[ C_m + C_{m_q} \frac{d\dot{\theta}}{2V_\infty} \right] \frac{q_\infty S d}{I} - \frac{F_{EJ} x_{EJ}}{I} \quad (2.4)$$

$$\frac{D\rho u}{Dt} = -\frac{\partial p}{\partial x} + \mu \left( \frac{\partial^2 u}{\partial x^2} + \frac{\partial^2 u}{\partial y^2} + \frac{\partial^2 u}{\partial z^2} \right) + \frac{1}{3} \mu \frac{\partial}{\partial x} \left( \frac{\partial u}{\partial x} + \frac{\partial v}{\partial y} + \frac{\partial w}{\partial z} \right) \quad (2.5)$$

Marshall [10] arrives at these three scaling schemes through the simplification of Equation 2.3 and Equation 2.4. Specifically he makes the assumption that angular motion is of a small enough magnitude that the normal-force and pitching-moment coefficients,  $C_N$  and  $C_m$ , vary linearly with angle of attack. This assumption also suggests that the axial-force coefficient,  $C_A$ , and pitch-damping derivative,  $C_{m_q}$ , are constant. By further

assuming that the flowfield vertical variations, and hence the normal-force and pitching-moment coefficients, can be represented by incremental values of angle of attack and pitching moment, shown in Equation 2.6, Marshall is able to effectively reduce the problem to two dimensions, vertical translation and pitch. These equations are given in Equation 2.7.

$$C_N = C_{N_\alpha} \left( \theta + \frac{\dot{z}}{V_\infty} + \Delta\alpha \right) \quad (2.6a)$$

$$C_m = C_{m_\alpha} \left( \theta + \frac{\dot{z}}{V_\infty} + \Delta\alpha \right) + \Delta C_m \quad (2.6b)$$

$$\frac{\ddot{z}}{g} = 1 - \left[ C_{N_\alpha} \left( \theta + \frac{\dot{z}}{V_\infty} + \Delta\alpha \right) \cos \theta - C_A \sin \theta \right] \frac{q_\infty S}{mg} + \frac{F_{EJ}}{mg} \cos \theta \quad (2.7a)$$

$$\ddot{\theta} = \left[ C_{m_\alpha} \left( \theta + \frac{\dot{z}}{V_\infty} + \Delta\alpha \right) + \Delta C_m + C_{m_q} \frac{d\dot{\theta}}{2V_\infty} \right] \frac{q_\infty S d}{I} - \frac{F_{EJ} x_{EJ}}{I} \quad (2.7b)$$

Deslandes and Donauer [9] arrives at the scaling schemes in a slightly different manner, by non-dimensionalizing Equation 2.5 as well as Equation 2.8, a different form of Equation 2.3a, in order to obtain the non-dimensional parameters desired for similarity. In the end, both approaches yield very similar results. However, the form of the scaling laws used by Marshall is more useful for this research as it allows for transparent manipulation of the scaled to freestream dynamic pressures.

$$m(\dot{u} + qw - rv) = -C_A S q_\infty - mg \sin \theta \quad (2.8)$$

### 2.2.1 Froude Scaling.

The relationships between scaled and full-size quantities for Froude Scaling are given by Equation 2.9. Froude Scaling is named because the velocity scaling given by Equation 2.9g is derived from ensuring the full-size and scaled Froude number is equal. This means that unless the acceleration due to gravity can be significantly increased, the



scaled velocity will be much lower than the full-size test velocity. If compressibility effects are negligible, then this velocity reduction is an acceptable compromise. If compressibility effects are non-negligible, such as in transonic or supersonic flight, then scaling the velocity is an unacceptable compromise. This makes Froude Scaling ideal for small-scale testing when full-scale releases occur at low, subsonic Mach numbers, where compressibility is not a factor [10].

$$z' = z\lambda \quad (2.9a)$$

$$\theta' = \theta \quad (2.9b)$$

$$m' = m\sigma v^2 \lambda^2 \frac{g}{g'} \quad (2.9c)$$

$$I' = I\sigma v^2 \lambda^4 \frac{g}{g'} \quad (2.9d)$$

$$F'_{EJ} = F_{EJ}\sigma v^2 \lambda^2 \quad (2.9e)$$

$$x'_{EJ} = x_{EJ}\lambda \quad (2.9f)$$

$$V'_\infty = V_\infty \sqrt{\lambda \frac{g'}{g}} \quad (2.9g)$$

$$t' = t \frac{\lambda}{v} \quad (2.9h)$$

### 2.2.2 Heavy Mach Scaling.

The relationships between scaled and full-size quantities for Heavy Mach Scaling are given by Equation 2.10. Heavy Mach Scaling matches the flight Mach number, making it useful for compressible flowfields, including supersonic flow. The heavy portion of the name derives from the simplified mass and moment of inertia relationships shown in Equation 2.11, which show that the scaled mass and moment of inertia are a function of not only the model scale factor,  $\lambda$ , but also the ratio of scaled to freestream dynamic pressures,  $q'_\infty/q_\infty$ . This relationship means that in order to match the model density to the store density, the wind tunnel dynamic pressure,  $q'_\infty$ , must be significantly reduced. If this reduction is not achieved, then the model acts much lighter than the store. If this

reduction is achieved, the amplitude of the model's pitch oscillations becomes larger than normal, due to the pitch damping term being reduced by a factor of  $\lambda^{1/2}$  [10]. Despite this pitch amplification, Heavy Mach Scaling has been shown by Deslandes and Donauer [9] to provide the most accurate translational trajectory information for the store. For this reason it is heavily used, though it is often difficult to achieve the high model density necessary to scale properly.

$$z' = z\lambda \quad (2.10a)$$

$$\theta' = \theta \quad (2.10b)$$

$$m' = m\sigma v^2 \lambda^2 \frac{g}{g'} \quad (2.10c)$$

$$I' = I\sigma v^2 \lambda^4 \frac{g}{g'} \quad (2.10d)$$

$$F'_{EJ} = F_{EJ}\sigma v^2 \lambda^2 \quad (2.10e)$$

$$x'_{EJ} = x_{EJ}\lambda \quad (2.10f)$$

$$V'_\infty = V_\infty \sqrt{\frac{T'_\infty}{T_\infty}} \quad (2.10g)$$

$$t' = t \sqrt{\lambda \frac{g}{g'}} \quad (2.10h)$$

$$m' = m \frac{q'_\infty}{q_\infty} \lambda^2 \quad (2.11a)$$

$$I' = I \frac{q'_\infty}{q_\infty} \lambda^4 \quad (2.11b)$$

### 2.2.3 *Light Mach Scaling.*

The relationships between scaled and full-size quantities for Light Mach Scaling are given by Equation 2.12. Light Mach Scaling matches flight Mach number, just as Heavy Mach Scaling does, making it useful for compressible flow situations. It also seeks to alleviate the increase in store density caused by Heavy Mach Scaling in order to create an accurate pitch response. This is achieved by assuming that the acceleration due to

gravity can be arbitrarily increased for the scaled experiment in the manner shown in Equation 2.13. The compromise caused by this increase is that the vertical acceleration is no longer accurate. This causes the vertical displacement to be too small, and while the observed trajectory can be modified to account for this error, it is not a perfect correction. Marshall [10] also discusses compensating Light Mach Scaling by modifying the ejection force, and Deslandes and Donauer [9] points out that the necessarily small scale of wind tunnel drop tests requires a very large increase in ejector force that the model may not be able to structurally withstand. It is also important to note that while the magnitude of the model's pitch response is more accurate for Light Mach Scaling, the frequency content of the response has shown to be insufficient [9].

$$z' = z\lambda \quad (2.12a)$$

$$\theta' = \theta \quad (2.12b)$$

$$m' = m\sigma\lambda^3 \quad (2.12c)$$

$$I' = I\sigma\lambda^5 \quad (2.12d)$$

$$F'_{EJ} = F_{EJ}\sigma v^2\lambda^2 \quad (2.12e)$$

$$x'_{EJ} = x_{EJ}\lambda \quad (2.12f)$$

$$V'_\infty = V_\infty \sqrt{\frac{T'_\infty}{T_\infty}} \quad (2.12g)$$

$$t' = t_\nu^\lambda \quad (2.12h)$$

$$g' = g \frac{v^2}{\lambda} \quad (2.13)$$

### 2.3 Store Separation

Store separation has traditionally been studied from the perspective of an external store being carried on a pylon under the wing or fuselage. This exposes the store to the freestream flow. The freestream environment, as a generality, is also quasi-steady. This means

that using time-averaged data to determine separation characteristics and aerodynamic forces acting on the external store entails an acceptable level of accuracy from a time-accurate accounting of the forces and moments. Conversely, internal store carriage exposes the store to the resonant flow of the cavity and the turbulent flow of the shear layer in addition to the freestream flow. The highly unsteady, volatile nature of these flow regimes creates unpredictability in the separation characteristics which can lead to a variety of store trajectories. Johnson, Stanek, and Grove [11] discusses this phenomenon, calling the worst case a "pitch bifurcation" where, depending on the cavity and shear layer environment at the time of drop, one drop will separate properly, exiting the shear layer into the freestream with a nose down pitch, while the other will exit the shear layer with a nose up attitude, causing the store to climb back towards the aircraft, possibly resulting in a collision. An illustration of this effect is shown in Figure. 2.3. Coley and Lofthouse [12] conducted 6-DOF computational tests with a Mk.82 500-lb. bomb in several configurations within a cavity and showed that the forces and moments acting on the store within the cavity and within the shear layer are of a very similar spectra to the pressure oscillations within the cavity.

The negative effects of cavity flow on stores within the cavity is well-documented. The high unsteady pressure levels have damaged aircraft bulkheads and destroyed weapon components [13]. The dramatic trajectory deviations now being observed are a more recent development assisted by recent trends in aircraft and weapon design. With aircraft such as the F-22 having the capability to supercruise, and an increased emphasis on stealth, dropping weapons from an internal weapons bay at speeds greater than Mach 1 has become essential to future and current aircraft. At the same time, increasing the accuracy and controllability of weapons to reduce collateral damage has driven weapons designers to design smaller, lighter stores that are less stable than their predecessors. The emphasis on speed and stealth, combined with the the need for lower collateral damage has created a

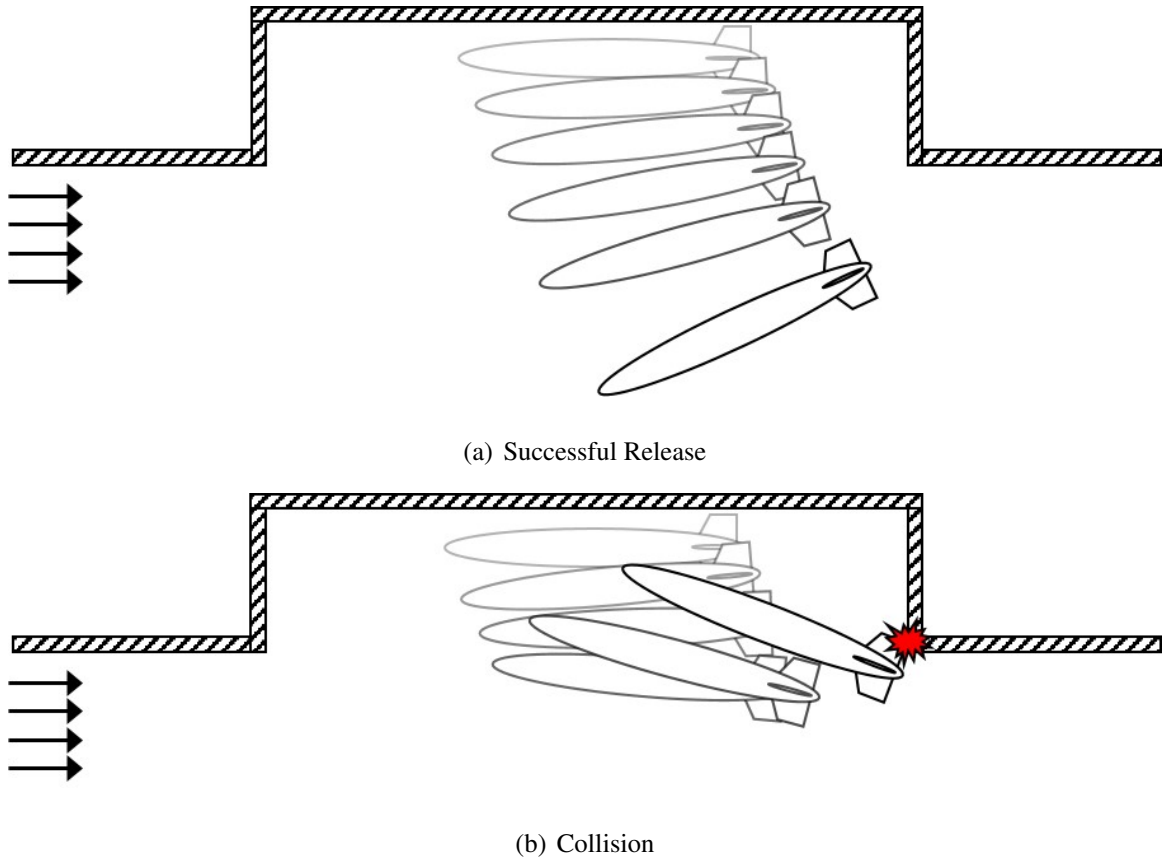


Figure 2.3: Example of Pitch Bifurcation

perfect storm of store and aircraft characteristics to drive dramatic trajectory deviations. In the past, spoilers on the B-1, B-2, F-117, and F-22 have been used to disrupt the shear layer and allow the store to separate successfully. These spoilers are limited to one design Mach number for peak effectiveness and become much less effective at speeds greater than Mach 1 [13].

## 2.4 Computational Analysis of Cavity Flows and Store Separation

The quasi-steady nature of external store separation and the ease with which initial conditions can be changed lends computational fluid dynamics (CFD), an enormous advantage for certifying and analyzing store separation problems. The major limit in CFD is computational expense. To run at small enough spatial and temporal scales to capture the

full spectrum of turbulence, known as Direct Numerical Simulation (DNS), is prohibitively expensive for all but the smallest of applications. In order to decrease the expense of CFD, larger temporal and spatial scales are used and the governing equations modified to exclude viscous effects, or to provide an empirically based model to determine the effects of the turbulence scales not resolved by the larger spatial and temporal scales. While this compromise means that the results are typically less accurate, modern CFD methods for analyzing unsteady flows are often utilized. Cavity flow simulations can provide a sufficient level of correlation between the computational and experimental results. Another limit to CFD is grid complexity. When a geometry has a large number of features that disrupt the flow, the grid must be refined in the area around those features. However, when grids reach a certain geometric complexity, the number of iterations necessary to gain convergence causes the simulation to be too expensive. The modern CFD method of overset or chimera gridding reduces this expense.

#### ***2.4.1 Turbulence Modeling in Cavity Flows.***

Turbulence modeling is based on the decomposition of primitive flow variables into a mean component and a fluctuating component, such as in Equation 2.14. When this decomposition is applied to the Navier-Stokes equations, and the results are Reynolds-Averaged, the Reynolds-Averaged Navier-Stokes (RANS) equations result [14]. The RANS equations contain an extra term, often called the Reynolds stress, that creates a closure problem in the equations. To account for this problem, a plethora of turbulence models have been created, each with specific strengths and weaknesses and each adapted best to a particular range of flow situations. Due to increases in computational power, more accurate and generalized simulations have become possible. One example of this is Large-Eddy Simulation (LES). LES is based on the idea that by directly simulating the largest eddy sizes and modeling all the smaller turbulent scales, computational cost can be reduced without sacrificing a great deal of accuracy. LES can typically be applied for

applications an order of magnitude larger than DNS, but still requires very refined grids and a great deal of computational expense. For this reason, hybrid RANS-LES models have become very popular in modern CFD codes. These models use RANS equations in the boundary layer and LES away from the wall. This results in increased accuracy over RANS models, while keeping the cost low enough to be applicable to engineering flows. Of these hybrid schemes, Detached Eddy Simulation (DES) is among the most popular and is commonly used in weapons bay flows. A thorough study of turbulence models as they relate to the spectrum and sound pressure level (SPL) of weapons bays has been conducted by a number of authors including Nichols and Westmoreland [15], Nichols [16], Zhang et al [5], Rizzetta and Visbal [17], and Rokita and Arieli [18]. These authors and others have analyzed models including Baldwin-Lomax, Spalart-Almaras (SA),  $k - \omega$ , Shear Stress Transport (SST), and Delayed DES (DDES) with various corrections. By far the most thorough of these analyses is Nichols [16], and his findings recommend the SST DDES model for weapons bay flows.

$$u = \bar{u} + u' \quad (2.14)$$

#### ***2.4.2 Overset Grid Techniques.***

Overset gridding, also called chimera gridding, is a modern CFD technique used to reduce the grid size and complexity necessary to resolve the flow around complex geometries. This is achieved by using multiple overlapping grids to describe the geometry. The main features that overset gridding adds to a CFD solver are hole-cutting, intergrid boundary point determination, and donor point interpolation. When two grids overlap, one grid, usually a background grid, has a “hole” cut in it. This is achieved through multiplying the governing equation by an array of the same size as the grid containing a 1 where a cell should be solved, and a 0 where a cell should not be solved [19]. This array is known as the chimera array [19]. Several methods exist to create this array, including the surface normal

vector test, the vector intersection test, and X-ray hole cutting. X-ray hole cutting is a more modern technique that creates an optimal hole cut [19, 20].

After this array is created, the intergrid boundary points must be determined, both for the background grid and the overlapping grid. This is known as ensuring domain connectivity and is the primary cost associated with implementing an overset grid solver. Both the computational and Cartesian spatial coordinates of each intergrid boundary point must be determined in order to ensure domain connectivity. The Inside/Outside test, gradient search method (also known as stencil walking), or spatial partitioning are all methods of determining domain connectivity. By intelligently combining these methods, efficient and fast methods of determining intergrid boundary points can be derived. Domain connectivity allows an overset solution to be solved by interpolating values between a donor grid's boundary points and a recipient grid and back to the donor grid as necessary to achieve convergence [19].

The complicated nature of overset gridding and the importance of carefully keeping track of the computational and Cartesian spatial coordinates of intergrid boundary points necessitates that overset grids currently contain only structured grids. At first glance, this might make it seem as if overset gridding is computationally inefficient. However, the complexity and density of a hybrid or unstructured grid necessary to resolve something like a store in a weapons bay requires a vast amount of time to incorporate the proper grid densities in all areas of interest. Furthermore, this grid would then only be applicable to a single store type in this weapons bay and with the store only at a single spatial coordinate. The most powerful advantage of overset gridding is that the overlapping grids can be easily swapped, allowing a single background grid, such as the weapons bay, to be used in testing a multitude of stores. Furthermore, by pairing the CFD results with a 6-degree-of-freedom (6DOF) solver, dynamic simulations, such as the release of a weapon, can be modeled



using the same grids for all spatial orientations of the weapon. This can be achieved simply by modifying the chimera array and reestablishing domain connectivity.

### **2.4.3 *OVERFLOW Solver.***

The OVERFLOW 2.1 code is a three-dimensional time-marching implicit Navier-Stokes CFD code developed by NASA [21]. Its capabilities include six degree-of-freedom (6DOF) modeling, a variety of inviscid flux algorithms and implicit solution algorithms, one- and two-equation turbulence models, a plethora of boundary conditions, a grid assembly code, and collision detection and modeling. OVERFLOW uses structured overset grid systems in two primary modes. In OVERFLOW mode, the code uses only the supplied grids in the solution, while in OVERFLOW-D mode, the user supplies near-body grids and the code generates Cartesian outer grids and uses the resulting product for solution.

The code contains a number of implicit solvers and includes the option to use sub-iterations as well as Low-Mach preconditioning for some schemes. Some of the included implicit solvers are Alternating Direction Implicit (ADI) Beam-Warming, Steger-Warming, Lower Upper-Symmetric Gauss Seidel (LU-SGS), and Successive Symmetric Over-Relaxation (SSOR). Flora [1] and Kraft [22] utilize the SSOR solver.

OVERFLOW has a variety of turbulence models. Included are the Baldwin-Lomax algebraic model, the SA 1-equation transport model, the  $k-\omega$  2-equation transport model, and the SST 2-equation transport model. Most important are the SA DES and DDES hybrid RANS/LES and SST DES and DDES 2-equation hybrid RANS/LES models. The inclusion of the SST DDES model and the 6DOF simulation capabilities make OVERFLOW ideal for the task of modeling weapons bay flows.

OVERFLOW solves the full Navier-Stokes equations in a generalized coordinate system, shown in Equation 2.15. The quantity  $q$  represents the vector of conserved variables as shown in Equation 2.16. Equation 2.17 shows the linearized Euler implicit form of Eq 2.15, including sub-iterations, as used by OVERFLOW. The viscous and

inviscid fluxes are contained in the term  $RHS$  and are shown in Equation 2.18 [21]. The OVERFLOW User's Manual [21] contains a more detailed discussion of the code's features and their implementation.

$$\frac{\partial \vec{q}}{\partial t} + \frac{\partial \vec{E}}{\partial \xi} + \frac{\partial \vec{F}}{\partial \eta} + \frac{\partial \vec{G}}{\partial \zeta} = 0 \quad (2.15)$$

$$\vec{q} = \forall \begin{bmatrix} \rho \\ \rho u \\ \rho v \\ \rho w \\ \rho e_o \end{bmatrix} \quad (2.16)$$

$$\begin{aligned} & \left[ I_{chim} + \frac{\Delta t}{(1 + \Theta) \Delta \tau} + \frac{\Delta t}{1 + \Theta} (\partial_\xi A + \partial_\eta B + \partial_\zeta C) \right] \Delta q^{n+1, M+1} = \\ & - \left[ (q^{n+1, m} - q^n) - \frac{\Theta}{1 + \Theta} \Delta q^n + \frac{\Delta t}{1 + \Theta} RHS^{n+1, m} \right] \end{aligned} \quad (2.17)$$

$$RHS = \frac{\partial \vec{E}}{\partial \xi} + \frac{\partial \vec{F}}{\partial \eta} + \frac{\partial \vec{G}}{\partial \zeta} \quad (2.18)$$

One of the most powerful tools in OVERFLOW, and what makes it so attractive for store separation problems, is its built-in 6DOF solver. Through the use of the *Scenario.xml* and *Config.xml* input files, the initial position, mass, and motion properties of any grid described in the grid input file, *grid.in*, can be manipulated. The *Config.xml* file contains information about the positions of the grids relative to each other, their initial conditions (velocity, rotation), and their motion (stationary, prescribed, 6DOF). The *Scenario.xml* file contains information about the non-dimensional mass properties of the grids, including the mass, moments of inertia, and the gravity constant. The equations for these properties are given in Equation 2.19. These files are used by the Geometry Manipulation Protocol (GMP) in concert with the OVERFLOW solver to produce 6DOF motion [21].

$$g^* = g \frac{L_{ref}}{V_{ref}^2} \quad (2.19a)$$

$$m^* = \frac{m}{\rho_\infty L_{ref}^3} \quad (2.19b)$$

$$I_{zz}^* = \frac{I_{zz}}{\rho_\infty L_{ref}^5} \quad (2.19c)$$

### III. Methodology

### 3.1 Experimental Setup

Testing was conducted at the AFIT Supersonic Variable-Density Blowdown (SVDB) wind tunnel, detailed in 3.1.1. In order to prepare the tunnel for testing, the capabilities of the SVDB were augmented through the production of three new supersonic nozzles, the production of a new interface between the stagnation chamber and the nozzle section, and the creation of a cavity fill block in order to characterize the flow from the new nozzles. Additionally, the existing National Instruments LabView interface was modified to include the automatic collection of frequency spectrum data.

### 3.1.1 *Supersonic Variable-Density Blowdown Tunnel.*

The SVDB tunnel is located in the AFIT high-speed aerodynamics laboratory and is a combination pull-down and blow-down facility. Figure 3.1 graphically depicts the key components of the tunnel, with numbers of the list below corresponding to the illustration.

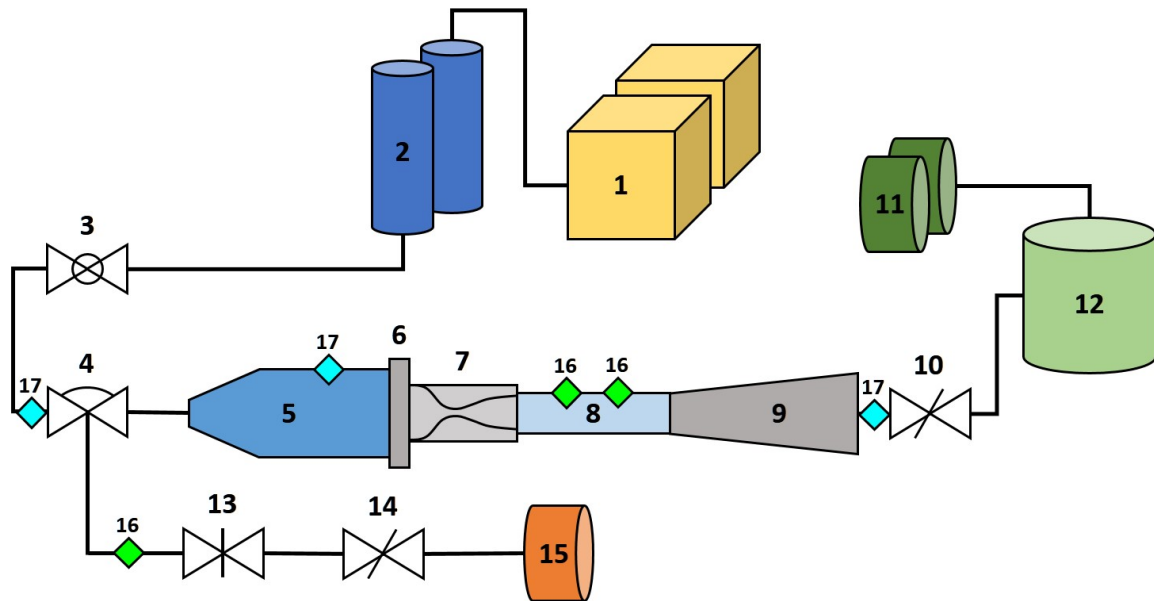


Figure 3.1: Key components of AFIT SVDB wind tunnel (Not to scale; some detail not shown)

1. High pressure compressors - Two Ingersoll Rand® Model UP6-50PE-200 compressors supply air up to 170 CFM at 180 psig.
2. Air dryers - Donaldson® Regenerative Air Dryers remove moisture from the compressed air to prevent tunnel icing and clouding.
3. Pressure-side valve - El-O-Matic® ball type valve controls the high pressure air supply to the tunnel.
4. Regulating valve - Pressure controlled Leslie diaphragm-type valve allows for pressure in the stagnation chamber and test section to be altered.
5. Stagnation chamber - Cylindrical chamber conditions flow upstream of the nozzle. Stagnation conditions are taken via a 8350C-50 Endevco® dynamic pressure transducer and a thermocouple.
6. Faceplate - Two mesh grids smooth the flow prior to entry into the nozzle. Further information is contained in 3.1.2.
7. Nozzle block - Various freestream Mach numbers can be discretely set using interchangeable nozzle blocks designed nominally for Mach 1.5, 1.9, 2.3, and 3.0 flow. Further discussion of the nozzles can be found in 3.1.4.
8. Test Section - A custom acrylic test section was designed with a cavity of dimensions 6.75”L x 1.75”W x 1.5” D, yielding an L/D of 4.5. Removable sidewalls allow for easy access to interior of test section. Further information can be found in 3.1.5.
9. Diffuser - An adjustable ramp diffuser allows control of downstream throat condition to ensure consistent, supersonic flow in the test section.
10. Vacuum-side valve - A Butterfly type valve isolates vacuum conditions required to attain sub-atmospheric stagnation pressures.

11. Vacuum pumps - A two-stage Stokes<sup>®</sup> Microvac vacuum pump draws a near vacuum on the pull-down side of the system.
12. Vacuum tank - Tank drawn down by vacuum pumps to charge the flow through the test section.
13. Needle Valve - Needle valve allowing precise control over low pressure side of Regulating Valve.
14. Vacuum Regulating Valve - Ball valve that controls the amount of vacuum applied to the low pressure side of Regulating Valve.
15. Roughing Pump - Vacuum pump that lowers Regulating valve pressure below atmospheric. More information can be found in 3.1.3.
16. Low Pressure Transducers - Endevco<sup>®</sup> 8530C-15 piezoresistive pressure transducers. More information can be found in 3.1.6.
17. High Pressure Transducers - Endevco<sup>®</sup> 8530C-50 piezoresistive pressure transducers. More information can be found in 3.1.6.

### ***3.1.2 Faceplate.***

The faceplate serves as an interface between the stagnation chamber and the nozzle block. It restricts the flow to a six inch long by two-and-a-half inch wide opening and provides flow control through the use of mesh screens. The faceplate is a one inch thick aluminum disk nineteen inches in diameter and is secured to the stagnation chamber using twelve one inch diameter bolts and a matching O-ring to ensure an airtight fit. The screens are attached to the stagnation chamber side of the faceplate. The screens utilized are two stainless steel uniform mesh screens with a bar diameter of 0.0059 inches and a spacing of 0.0295 inches. The screens are placed 1.772 inches apart. This distance yields a freestream turbulence of approximately two percent by the time flow reaches the second

screen. The location of the screens on the upstream side of the faceplate allow a similar distance between the second screen and the test section, once again yielding an approximate freestream turbulence level of two percent by the time flow enters the nozzle block [23].

### ***3.1.3 Regulating Valve.***

The Regulating valve's primary purpose is to ensure a steady flow of high pressure air from the compressors to the stagnation chamber. One side of the diaphragm is connected to the stagnation chamber while the other can be connected to multiple pressure sources. This side of the valve will be referred to as the pressure side. Initially, the pressure side was connected to the high pressure line via a manually operated valve. This valve was used to apply higher than atmospheric pressure to the pressure side of the diaphragm valve, allowing for higher than atmospheric stagnation pressures. While most effective at higher pressures, this setup is viable down to atmospheric pressure, where the valve is entirely closed. This corresponded with stagnation pressures no lower than 3.5 psia. In order to drive the stagnation pressure lower, the setup described in 3.1.1 and shown in Figure 3.1 was implemented. This includes the use of a small vacuum pump connected with a series of valves and tubes to the pressure side of the diaphragm. When the roughing pump is switched on, it evacuates air from the first section of tube. To tightly control the pressure applied to the diaphragm, the first section of tubing is terminated in the Vacuum Regulating Valve described in 3.1.1. This valve is opened slightly to allow it to evacuate air from the rest of the tubing. This results in a near vacuum on the pressure side of the diaphragm, too low of a pressure to allow the tunnel to operate properly. To control this, the Needle Valve described in 3.1.1 is used. This valve is connected to the pressure side line on one side and open to atmosphere on the other. By opening the valve, air at atmospheric pressure is introduced to the system, allowing precision control over the pressure applied to the pressure side of the diaphragm. This setup is instrumented with an Endevco® 8530C-15

piezoresistive pressure transducer, discussed further in 3.1.6. This low stagnation pressure setup is shown in Figure 3.2.

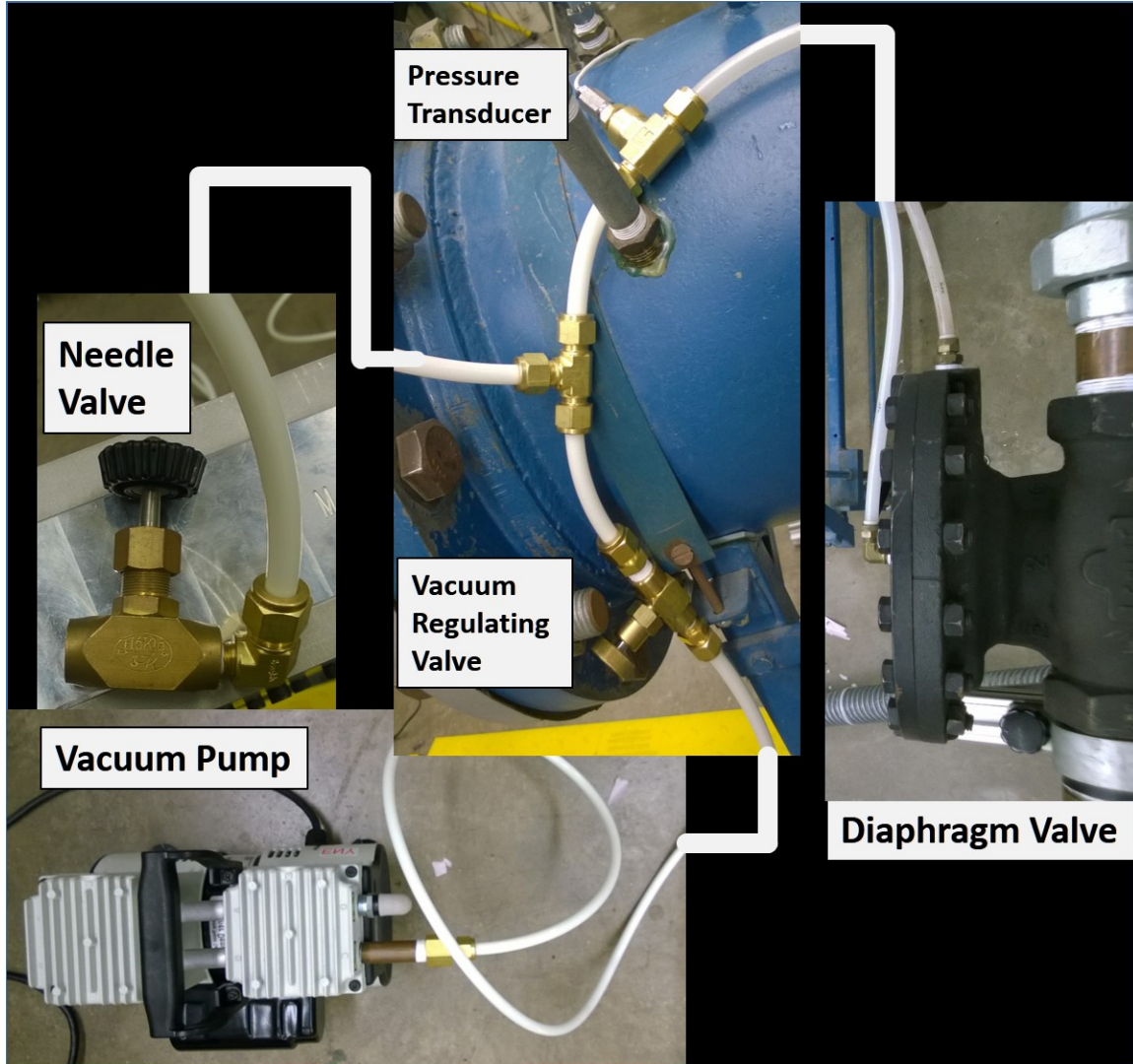


Figure 3.2: Low stagnation pressure setup

#### **3.1.4 Nozzle Block.**

The current capabilities of the SVDB tunnel include a nozzle block designed to produce Mach 3 flow. In order to investigate the effects of Mach number on Heavy



Mach Scaling and store separation, three additional nozzles were designed to provide Mach numbers of 1.5, 1.9, and 2.3.

The relations of flow quantities in supersonic flow are well understood, as are the effects of shockwaves on supersonic flow. By assuming isentropic flow through a 2D nozzle, a valid assumption if there are no shockwaves in the nozzle, then the ratio of throat area to test section area is given by Eq 3.1. This equation fixes the throat area of the nozzle required to reach a specific Mach number, given the test section area. Table 3.1 shows the area ratios for the Mach numbers of interest.

$$\frac{A^*}{A} = M \left[ \frac{2}{\gamma + 1} \left( 1 + \frac{\gamma - 1}{2} M^2 \right) \right]^{-\frac{\gamma + 1}{2(\gamma - 1)}} \quad (3.1)$$

Several methods exist to generate the curve between the throat, where the flow reaches Mach 1, and the test section, where the flow should reach the design Mach number. Most of these methods stem from the method of characteristics, originally put forth by Prandtl and Buseman [24]. The general theory of this method is that an initial curve is assumed and a final curve is determined that results in uniform and parallel flow into the test section. To do this, the Prandtl angle for the terminal Mach number is found,  $\nu_t$ . Then, starting at the throat, the flow field is described by the Prandtl angle,  $\nu$ , and the expansion angle,  $\Theta$ . Once this is achieved, the inflection point of the final curve is defined where  $\Theta + \nu = \nu_t$  and all expansion waves upstream of this point are reflected, while all expansion waves downstream of this point are terminated. In this fashion, the final curve, which is unique to the particular length, initial curve, and initial wave angles chosen, is determined. This method is graphical and time-intensive in nature, so several other methods have been created, both graphically and analytically, that improve upon this original method. Puckett's Method is an example of a more efficient graphical technique, while Foelsch's Method is analytical in nature and well suited to creating traditional nozzle designs [25–27]. Modern digital computers make numerically solving the method of characteristics a

Table 3.1: Mach Number Correlations for Isentropic Air

M	$p/p_t$	$A/A^*$	$\nu$	$\mu$
1.50	0.2724	1.1762	11.905	41.81
1.90	0.1492	1.5555	23.586	31.76
2.30	0.0800	2.1931	34.283	25.77

relatively simple task and many open-source programs exist to generate nozzle contours based on these solutions.

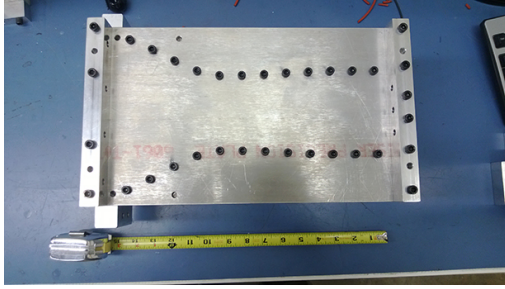
Nozzle design is a balance between too long and too short. A minimum length nozzle, characterized by an initial expansion angle of  $\frac{1}{2}\nu_t$ , is called so because it describes a nozzle that is of minimum length to not produce shock waves or expansion waves outside of the nozzle. However, minimum length nozzles can have non-uniform flow into the test section. A nozzle design that is too long is similarly undesirable. In a long nozzle, the boundary layer can build to undesirable thicknesses, causing unrealistic flow situations in the test section and introducing an unwanted level of uncertainty and turbulence.

Rather than beginning with an initial curve and perform one of the nozzle contour generation algorithms, the Air Force Research Laboratory (AFRL) Trisonic Gas Facility (TGF) was contacted to obtain nozzle contours that were well documented and suitable for use in the SVDB facility. By matching the contours downstream of the throat, and hence Mach number, the new nozzles offer a means of testing at scaled down conditions matching those of the TGF, which will provide long-term advantages to other research. Once the contours were obtained, substantial scaling and alteration had to be performed in order to match the specifications of the SVDB. The contours were scaled to match 1.25 inches above centerline at the downstream exit. This corresponds to the 2.5 inch height of the test section of the SVDB when used in a symmetrical nozzle. Next, the portion of the nozzle upstream of the throat had to be matched to the size of the SVDB. Minimal

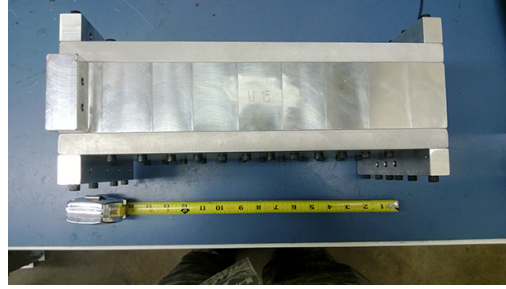
length difference was desired between the 14 inch Mach 3 nozzle currently in use and the new nozzles. Initially an algorithm was created using MATLAB<sup>®</sup> which would generate a sinusoid of sufficient period and magnitude to minimize the error between the new curve and the contours given for the first few points upstream of the throat. This curve was then adjoined to the data set of points describing the divergent portion of the nozzle to create a nozzle approximately 18 inches in length. A sinusoid was chosen in order to ensure a derivative of zero at the throat.

It was determined that for ease of use, the nozzle should be redesigned to match the 14 inch length of the current Mach 3 nozzle. This simplified the problem greatly and led to an algorithm to solve for the amplitude and frequency necessary to create a sinusoid to bridge the gap between the fixed length divergent portion of the nozzle and the fixed height of the upstream portion of the SVDB. This led to a unique curve that was adjoined to the divergent data set and outputted to a text file. The program used to generate these text files is shown in Appendix A.

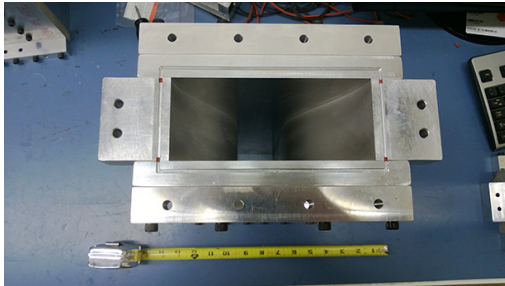
Solidworks was used to create a curve through the XY points defined in the text file for each Mach number. This was then used to generate a 2.5 inch wide block that described the main nozzle block for each Mach number. Side walls and attachment flanges were created as separate parts to ease construction. After all parts were designed, an assembly was created in order to place holes for the screws securing the side walls and flanges to the nozzle and the completed nozzle block to the wind tunnel. O-ring grooves were cut on both sides of the nozzle sections and both the upstream and downstream faces in order to ensure airtight connections. The final nozzles were constructed of solid aluminum. Figure 3.3 shows the Mach 1.5 nozzle, Figure 3.4 shows the Mach 1.9 nozzle, and Figure 3.5 shows the Mach 2.3 nozzle. More detailed drawings can be found in Appendix G.



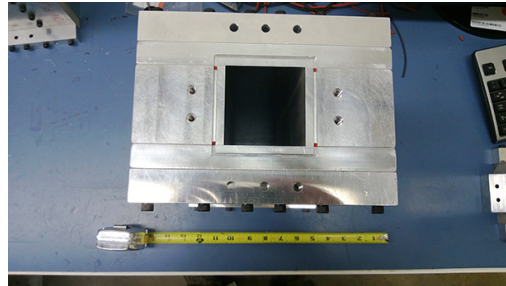
(a) Side



(b) Top

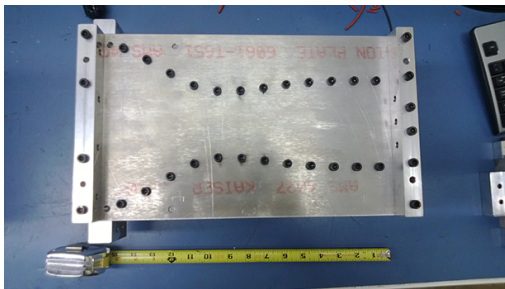


(c) Upstream (from stagnation tank)

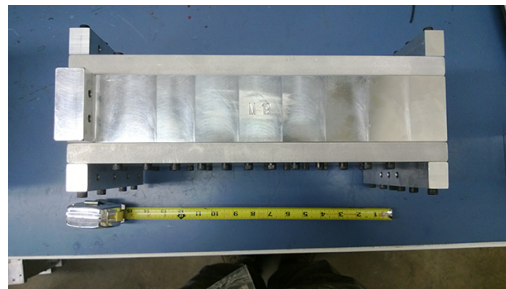


(d) Downstream (from test section)

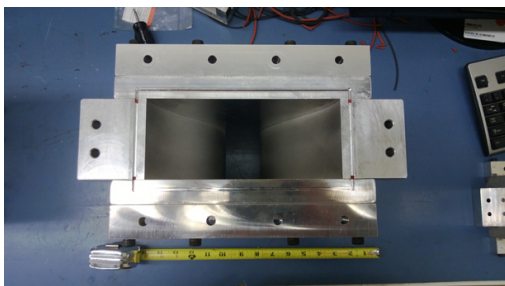
Figure 3.3: Multiple views of the assembled Mach 1.5 nozzle block



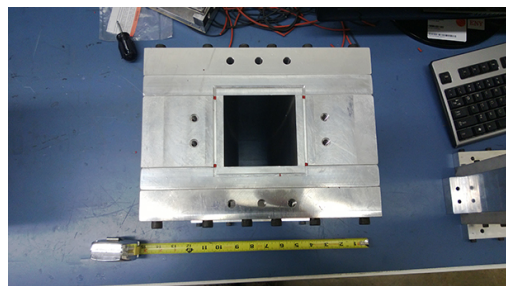
(a) Side



(b) Top

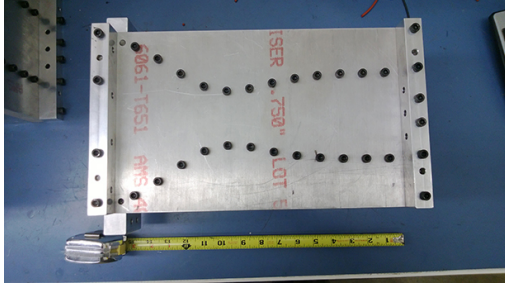


(c) Upstream



(d) Downstream

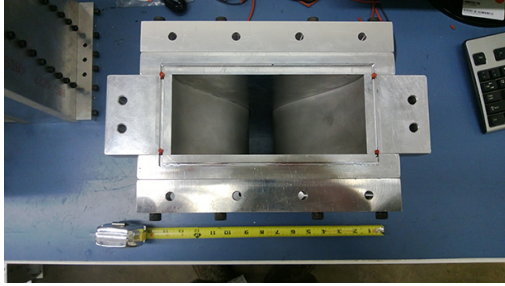
Figure 3.4: Multiple views of the assembled Mach 1.9 nozzle block



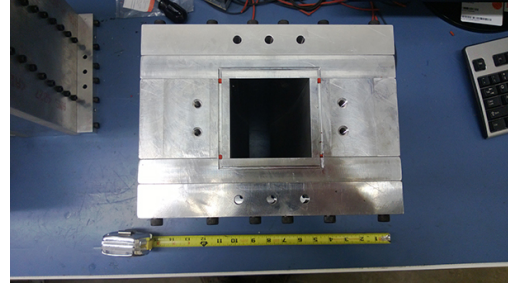
(a) Side



(b) Top



(c) Upstream



(d) Downstream

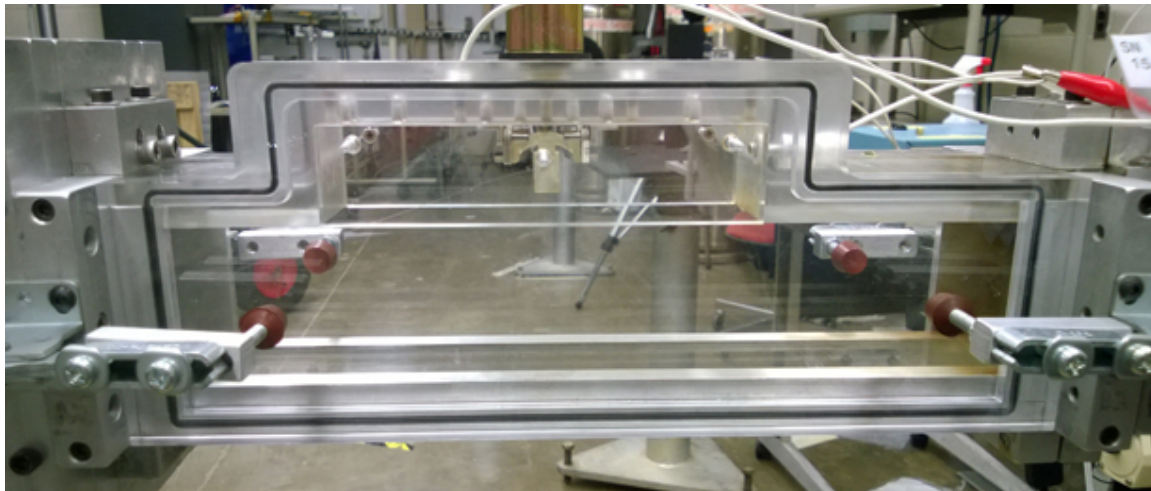
Figure 3.5: Multiple views of the assembled Mach 2.3 nozzle block

### 3.1.5 Test Section and Cavity.

The test section is constructed of acrylic and aluminum, with removable acrylic side walls allowing optical access to the cavity and test sections for Schlieren photography. Figure 3.6 shows the test section installed in the tunnel with side walls attached. The test section is 2.5 inches by 2.5 inches and is approximately 16 inches long. The cavity is a 3:8 scaled version of the Weapons Internal Carriage and Separation (WICS) bay that is built into the top of the test section with dimensions of  $D = 1.5in.$ ,  $W = 1.75in.$ , and  $L = 6.75in.$ , yielding an  $L/D$  of 4.5. The cavity is configured for up to six dynamic pressure transducers, five in the roof of the cavity and one in the back wall. Figure 3.7 shows this configuration.

In order to adapt the test section for characterization of the new nozzles, a fill block is used. Figure 3.8 shows the fill block, which is designed to match the dimensions of the cavity and is constructed of rapid prototyping (RP) material using an Objet® 3D printer. The four posts are positioned to line up with the first two and last two transducer mounts





(a) Side view



(b) Off axis view

Figure 3.6: Two views of the test section

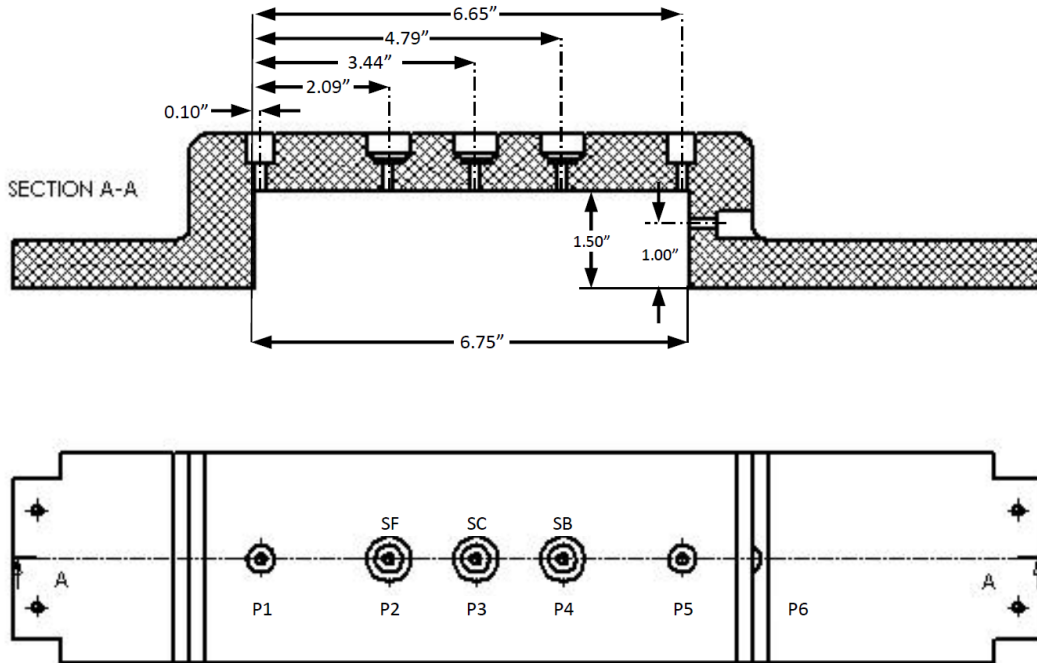
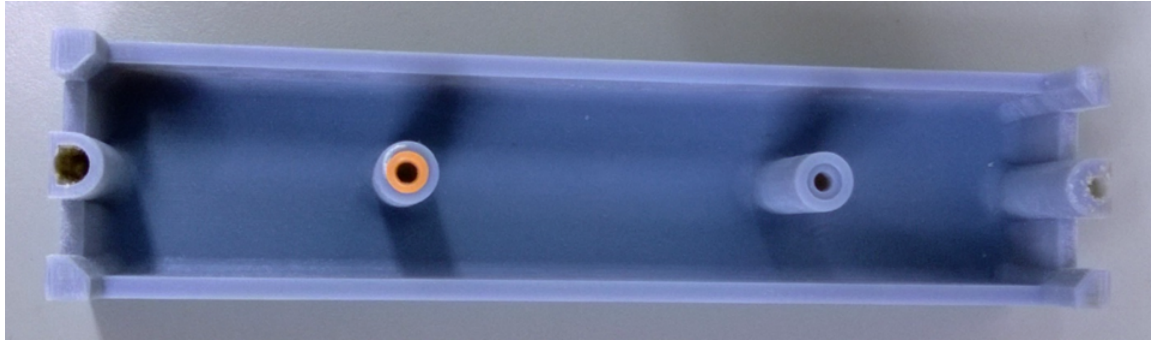


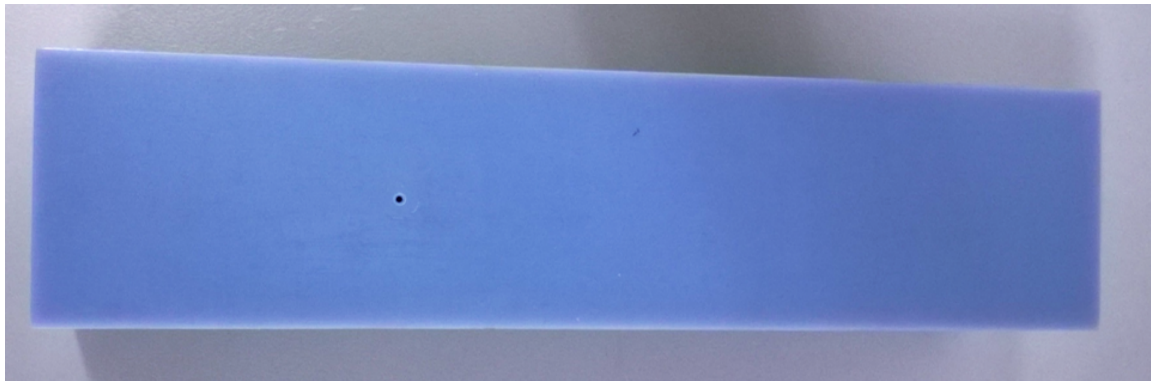
Figure 3.7: Location of Transducer Mounts in Cavity [1]

in the roof of the cavity. This allows the first and last post to be used to secure the fill block to the cavity. The second post is fitted with an O-ring and a small diameter hole is drilled through the bottom of the fill block. This serves as a static pressure port, allowing quantitative verification of the freestream Mach number. Data is obtained in this manner in order to facilitate rapid tunnel reconfiguration from the nozzle characterization setup to the cavity characterization or drop test configuration. Figure 3.9 shows the fill block installed in the test section. The fill block is designed to be interoperable with all other tunnel configurations.

For drop testing, the fill block is removed and the center transducer mount is fitted with a release mechanism. The release mechanism is a solenoid-driven carriage fixed to the roof of the cavity. When a voltage is applied to the solenoid, the clamp arms of the carriage release the store with nominally zero ejector force. Figure 3.10 shows the mechanism in the opened and closed position. The clamp arms are manufactured using an Objet® 3D



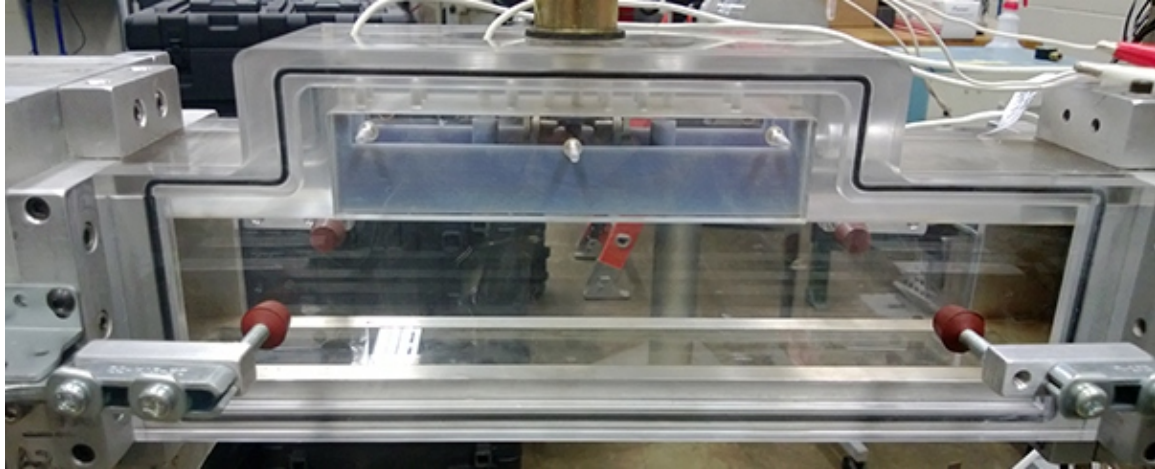
(a) Top view



(b) Bottom view

Figure 3.8: Two views of the fill block outside the tunnel (flow from left)



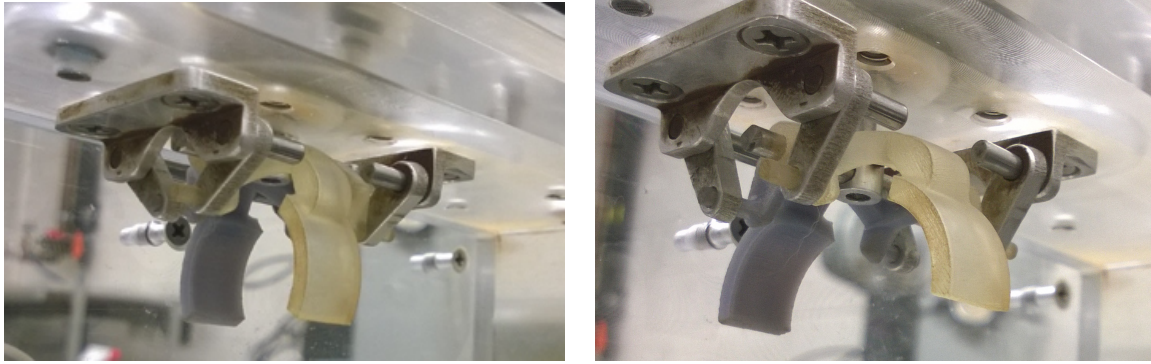


(a) Side view w/ sidewall



(b) Off axis view w/o sidewall

Figure 3.9: Two views of the fill block installed in the test section



(a) Closed

(b) Open

Figure 3.10: Release mechanism in the open and closed positions

printer. This allows quick production of replacement parts and it was observed that using RP material as opposed to longer lasting metal arms has the advantage of reducing the melting of the ice models after installation in the mechanism and before being dropped.

### ***3.1.6 Data Acquisition.***

Data acquisition is conducted using two primary systems. Schlieren photography is captured using a Photron FASTCAM-X<sup>®</sup> digital camera and postprocessed using Photron software. Multiple frame rates are utilized to best capture the various features of the flow. Additionally, slight changes in the refraction setup of the system allows for the resolution of different portions of the test section, including the boundary layer upon exit from the nozzle block.

Pressure data is collected using multiple types of Endevco<sup>®</sup> 8530C piezoresistive pressure transducers. In the stagnation chamber, high pressure Regulating Valve setup, and the vacuum valve, 8530C-50 transistors are used with a range of 0-50 psia. In the test section, specifically at the 2nd and 6th locations shown in Figure 3.7, and in the low pressure Regulating Valve setup, 8350C-15 transistors are used with a range of 0-15 psia and greater sensitivity than the 8530C-50 transistors. The pressure transducers were calibrated using a Martel<sup>®</sup> BetaGauge 330 hand-held pressure calibrator and the

calibrations were uploaded into the tunnel control virtual interface. Details of the calibrations are provided in Appendix B. Temperature data is collected using an Omega K-Type thermocouple.

The output of these sensors is transferred to two Endevco® 136 DC differential voltage amplifiers where a flat gain of 50 is applied to them. The signals are then transmitted to a National Instruments® data acquisition card for transfer to the data acquisition system.

All data is then transmitted to a National Instruments® NI PXI-1042 computer running the National Instruments® LabView software. A virtual interface run by LabView® automates the tunnel control and the data collection processes. In parallel with this computer, pressure data from the back wall of the cavity, the 6th position, is transmitted to an Agilent® 35670A spectral analyzer. This analyzer is connected to the NI computer using a GPIB to USB adapter cable. This facilitates the control of the spectral analyzer in a LabView® virtual interface. The spectral analyzer is set to observe data between 0 and 6400 Hz and compute twenty flat-top averages at 800 lines of resolution. This results in each average taking 125 ms, with full data being collected in 2.5 sec and then saved to the NI computer in a file separate from the other data. The spectral analyzer is currently triggered by hand, but could be incorporated into the existing virtual interface to function seamlessly with the tunnel.

## **3.2 Experimental Methodology**

### ***3.2.1 Procedures.***

Testing begins with the start-up of the vacuum pump. The two-stage nature of the pump requires a warm-up time of approximately two minutes between stage one and stage two to maintain optimum performance and reliability. Next, the supply valve to the tunnel must be opened followed by the configuration of the tunnel and, finally, data collection.

Initially, verification testing of tunnel performance was conducted on the existing Mach 3.0 nozzle, which was already installed in the tunnel. Upon completion of this

testing, the nozzle was removed, to be replaced by the Mach 2.3 nozzle. Upon removal, several important mechanical differences were noted between the Mach 3 nozzle and the new set of nozzles. First, the Mach 3 nozzle included a pair of bolted on hemispherical blocks, allowing it to fit snugly into the faceplate. The asymmetric and non-flush mounting of these blocks and the non-flush connection of the nozzle and the mesh housing to the faceplate spawned the creation of the new faceplate, discussed in 3.1.2, to solve this problem. Second, the Mach 3 nozzle was designed as an asymmetric nozzle, placing its downstream opening higher than the new nozzles, all of which were designed as symmetric nozzles. Unfortunately, the construction of the stagnation chamber does not allow the one inch height change necessary to mount the new nozzles to the test section. To address this difference a rail system was designed to elevate the stagnation chamber the required one inch and allow the stagnation chamber to slide upstream while keeping it square to the test section. This greatly decreases the assembly time and ensures the nozzle and test section have a flush, level, and airtight connection.

With these initial problems solved, configuring the tunnel becomes much more simple. The desired nozzle block ( $M=2.3$ , 1.9, or 1.5) is connected to the faceplate and the test section. Next, the Regulating valve pressure is set. This loosely correlates to the stagnation pressure and allows a quantitative measure of the likely stagnation pressure prior to tunnel activation. Finally, the test section is configured as desired. If nozzle characterization testing is to be conducted, the fill block must be installed and the Schlieren adjusted to better image the forward portion of the test section. Figure 3.9 shows the tunnel configured for nozzle characterization. During cavity characterization, the fill block is removed and the Schlieren must be adjusted to image the entire cavity and any unused transducer mounts must be filled. Figure 3.6 shows the tunnel configured for cavity characterization. During drop testing, the test section is configured in an identical manner to cavity characterization. The ice models must first be checked and mounted within the release mechanism.

The ice-store fabrication process takes approximately one hour. The molds are filled and then placed in the freezer. Once solidified, the models are weighed and visually inspected to ensure that there are no large defects and that the model weight is consistent with averages. Multiple molds are used to increase the rate of testing.

Finally, data acquisition must be configured for the current test objectives. If nozzle characteristics are being observed, the option to activate the release mechanism must be disabled. For measuring cavity characteristics, the release mechanism should be disabled, the spectral analyzer must be powered on, and its virtual interface prepared. Drop testing requires the release mechanism to be active as well as the spectral analyzer.

Immediately before initiating a run, the Regulating valve pressure is recorded, along with the test name. The tunnel is initiated with the virtual interface. Then, 3.5 seconds after the run is initiated, the FASTCAM begins collecting data. At this time, the spectral analyzer is also started. After sufficient data is collected, typical runs range from five to eight seconds, the tunnel is shut down manually via the virtual interface. Adjustments are made to the Regulating valve pressure, FASTCAM data is saved, and any other configuration changes are made. Typically within fifteen minutes or less, depending on mass flow, the vacuum pump has reduced the pressure significantly enough for another run to take place.

### ***3.2.2 Data Reduction.***

All quantitative data is saved in tab-delimited text files. This allows for easy input and manipulation using MATLAB®. After the data is loaded into MATLAB®, the startup transients are removed by the program. This is done by only considering the data after the tunnel has been running for 3.4 seconds. This limit was determined empirically. At this point, the data reduction is determined by the type of run being analyzed. For the nozzle characterization process, the Mach number is an unknown to be determined by Equation 3.2. In a cavity characterization run, the Mach number is assumed and the Rossiter modes are calculated assuming this Mach number. This Mach number is set

to be average of the freestream Mach numbers from all of the nozzle characterization runs. Additionally, the freestream test conditions, including viscosity, Reynolds number, temperature, density, pressure, and velocity are determined. This is done using the Flow\_Con.m MATLAB® function shown in Appendix C.

$$M = \sqrt{\frac{2}{\gamma - 1} \left( \left( \frac{p_T}{p} \right)^{\frac{\gamma - 1}{\gamma}} - 1 \right)} \quad (3.2)$$

Flow\_Con.m is a MATLAB® function with logic to determine the type of data reduction needed based on the input arguments. The required inputs are the filepath of the .lvm file to be analyzed, the structure containing the loaded data, and a start time for data reduction. The output is the data structure appended with the flow conditions as new fields. Based on the filename, the function will either analyze Mach number or assume Mach number, as discussed above. The other flow conditions are then calculated using Equation 3.3. All arguments are formatted in English Engineering units using pounds as the unit of force, feet as the unit of length, slugs as the unit of mass, and degrees Rankine as the unit of temperature.

$$p_{\infty} = \frac{p_t}{\frac{p_t}{p}} \quad (3.3a)$$

$$T_{\infty} = \frac{T_t}{1 + (\gamma - 1) M_{\infty}^2} \quad (3.3b)$$

$$\rho_{\infty} = \left( \frac{p_{\infty}}{R_{air} T_{\infty}} \right) \quad (3.3c)$$

$$\mu_{\infty} = \frac{1.458 \times 10^{-6} \left( \frac{5}{9} T_{\infty} \right)^{1.5}}{\frac{5}{9} T_{\infty} + 110.4} \quad (3.3d)$$

$$a_{\infty} = \sqrt{\gamma R_{air} T_{\infty}} \quad (3.3e)$$

$$V_{\infty} = M_{\infty} a_{\infty} \quad (3.3f)$$

$$Re_{\infty} = \frac{\rho_{\infty} V_{\infty}}{\mu_{\infty}} \quad (3.3g)$$

To further characterize the flow exiting the nozzle, turbulent boundary layer theory is used to approximate the boundary layer at the exit of the nozzle by utilizing the methods put forth in McCabe [26] and Rogers and Davis [2]. To approximate the radius of curvature, Equation 3.4 is used. Figure 3.11 shows the graph, taken from Rogers and Davis [2] used to estimate the boundary layer thickness parameter. The process of estimating the boundary layer thickness is automated using BL\_Thickness.m, shown in Appendix E. This estimate is compared to qualitative data obtained using Schlieren photography at 16,000 frames per second and a resolution of  $320 \times 32$ . This corresponds to 50.8 pixels per inch, allowing an estimate of the boundary layer thickness.

$$\rho = \frac{|1 + f'^2|^{3/2}}{|f''|} \quad (3.4)$$

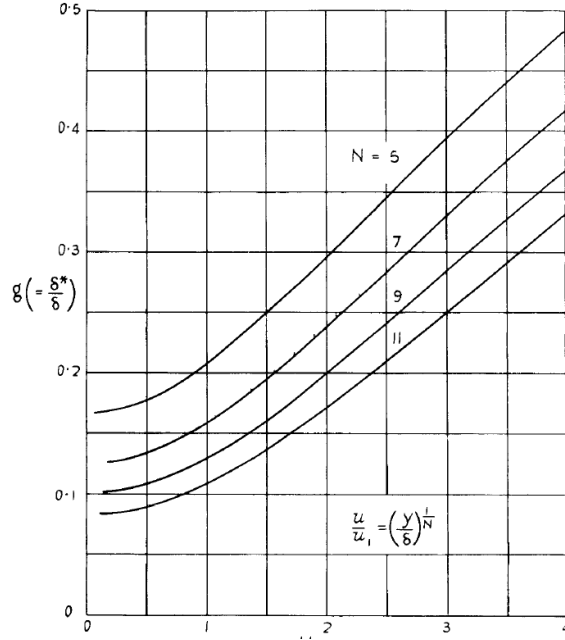


Figure 3.11: Boundary Layer Thickness Parameter vs. Mach number, reprinted from Rogers and Davis [2]

To characterize the cavity and determine whether it matches the expected Rossiter modes, another MATLAB<sup>®</sup> function was created, `Rossiter.m`, shown in Appendix D. `Rossiter.m` requires the structure containing the data from `Flow_Con.m`, the desired modes, and the cavity length as input values. It appends the data structure with an array of the Rossiter modes as an output. The function includes logic to display an error message if the required fields are not present in the data structure, specifically the freestream Mach and freestream Velocity. These functions are called in a driver program, `Cavity_analysis.m`, which also processes the data produced by the spectral analyzer. The spectral data is recorded in the form of RMS voltages, so it is first converted to RMS pressures using the information from Figure B. Then this pressure data is converted to SPL using Equation 3.5. The reference pressure used is  $2.9 \times 10^{-9}$  psi, which is a commonly used reference, as it represents the threshold of human hearing. `Cavity_analysis.m` is shown in Appendix J.



$$SPL = 10 \log \frac{p_{RMS}^2}{p_{ref}^2} \quad (3.5)$$

The drop testing data reduction is the most involved experimental data reduction. Flow conditions are determined via the Flow\_Con.m function. Trajectory data is created when Schlieren video data taken during testing is parsed into images spaced 0.0075 seconds apart. These images are then loaded into digitizing software by Engauge®. The axis points are set by the corners of the cavity and the center of mass of the sphere is set as a data point. This data is then output to a comma separated value (CSV) file. This is done by hand for each image parsed from the video file. Automated methods of accomplishing this task were investigated, however, the diffraction caused by the varying thicknesses of plexiglass as the light from the Schlieren lamp passed through the test section was of sufficient severity to impede accuracy from frame to frame. Once the CSV files were generated, trajectories were plotted using the MATLAB® program Mult\_traj\_plot.m, shown in Appendix H.

Heavy Mach scaling data was achieved through the use of the Flow\_Con.m function in conjunction with 3 other functions. These functions are mass.m, which is a look-up table of store mass based on test number, ATMOS.m, which generates standard atmosphere data when given an altitude, and HMS.m, which creates a structure of scaled quantities based on the test conditions provided by Flow\_Con.m, the mass properties provided by mass.m, and the standard-day properties provided by ATMOS.m. The sequencing of these functions is contained in the driver program Drop\_analysis.m. Mass.m, ATMOS.m, HMS.m, and Drop\_analysis.m can be found in Appendix I.

### 3.3 Computational Methodology

#### 3.3.1 Grid Generation.

Previous computational efforts resulted in a functional multiblock grid based on a grid used by Nichols to describe the WICS bay [16]. This grid consists of two blocks, *Plate* and *Bay*. These blocks were augmented by adding two grids to describe a sphere

Table 3.2: Computational Domain Information

Block	Name	Cells	Dimensions	Wall Spacing (in)
1	Plate	5600000	$351 \times 201 \times 81$	$2.8125 \times 10^{-3}$
2	Bay	1920000	$201 \times 81 \times 121$	$2.8125 \times 10^{-2}$
3	Yin	140000	$41 \times 71 \times 51$	$1.875 \times 10^{-3}$
4	Yang	140000	$41 \times 71 \times 51$	$1.875 \times 10^{-3}$

of the same proportions as the experimental setup. These grids, *Yin* and *Yang*, are two overlapping C-type grids based on the approach by Kageyama and Sato [1, 28]. In the grid files, the cavity extends from 15.0 inches to 33.0 inches in the x-direction, 0.0 to -4.0 in the z-direction, and from -2.0 to 2.0 in the y-direction. The experimental cavity is a 3:8 scale version of these dimensions, so trajectory data and wall spacing was scaled to this size. The *Plate* grid has a wall spacing upstream of the cavity of 0.0028 inches. The Bay grid has a wall spacing of 0.028 inches. The spacing could be reduced within the cavity because of lower wall shear stress [16]. The *Yin* and *Yang* grids have a wall normal grid spacing of 0.0019 inches and extend 0.19 inches from the surface of the sphere with a cell growth rate of 1.2 [1]. Figure 3.12 shows the computational domain, with the axes oriented with  $x$  in the streamwise direction and  $z$  aligned with the gravity vector. Table 3.2 summarizes the grid information.

### 3.3.2 Boundary Conditions.

Boundary conditions in OVERFLOW are broken into groupings for each grid. The *Plate* grid contains eleven boundary conditions. Figure 3.13 shows the locations of the boundary conditions. Table 3.3 shows these boundary conditions and their corresponding numbers from Figure 3.13. The number 3 boundary condition, the inviscid adiabatic wall, exists to prevent any outflow across the inflow boundary and to create a uniform flow field.

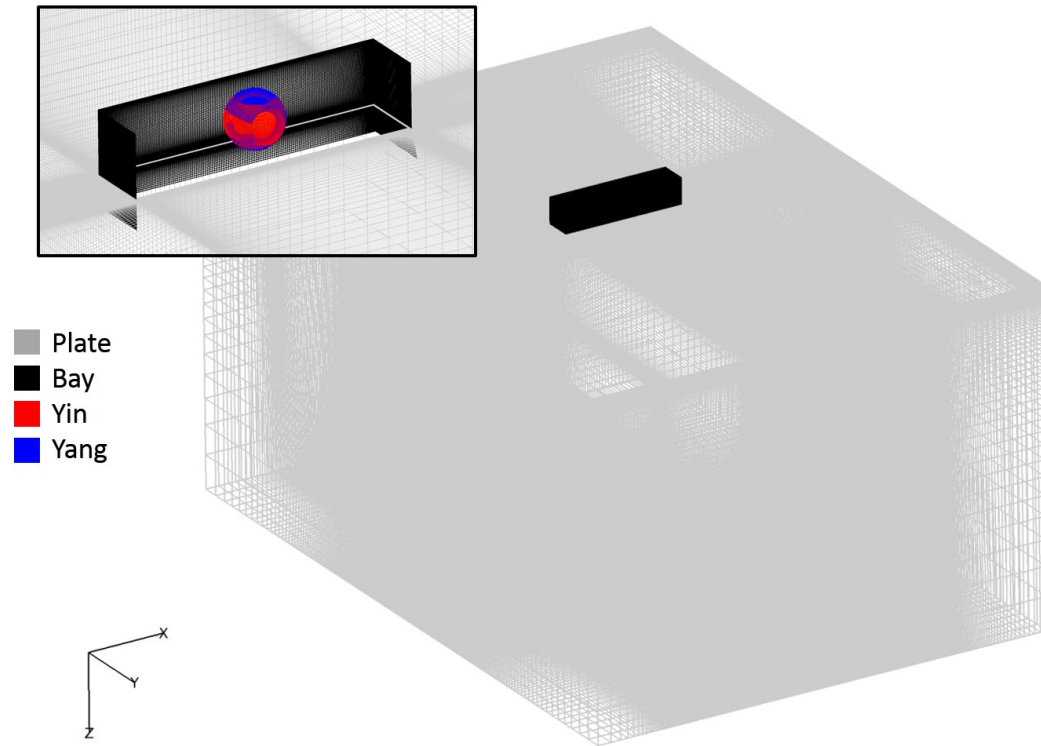


Figure 3.12: Computational Domain with detail showing *Bay*, *Yin*, and *Yang* grids

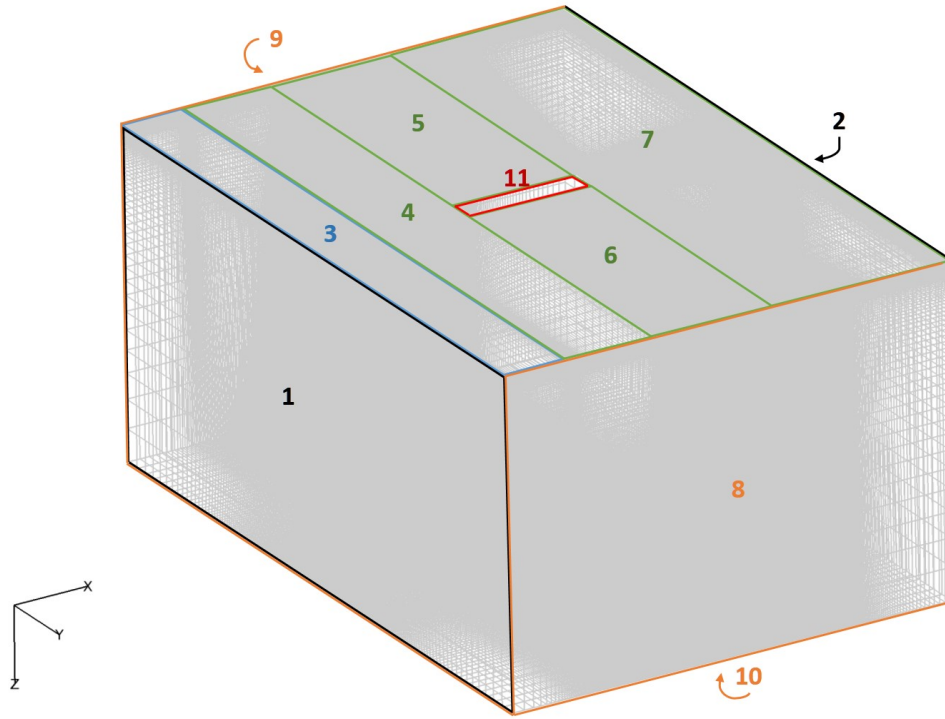


Figure 3.13: Boundary Condition Locations of *Plate* Grid

The *Bay* grid has much more simple boundary conditions, with all physical boundaries implementing a viscous adiabatic wall condition. Three artificial boundary conditions are also defined in the *Bay* grid that can be used to extract pressure data from the centerline of the cavity. These conditions, labeled as 201 in OVERFLOW, output the vector of conserved variables at each time step for the locations specified. The three conditions specify a line down the centerline of the cavity and running up the front face of the cavity, along the ceiling, and down the back face of the cavity. Figure 3.14 shows this line. The *Yin* and *Yang* grids each consist of a viscous adiabatic wall boundary condition describing the surface of the sphere.

Table 3.3: *Plate* grid Boundary Conditions

Region	Type
1	Inflow (impose freestream)
2	Outflow (pure extrapolation)
3	Inviscid adiabatic wall (pressure extrapolation)
4	Viscous adiabatic wall (pressure extrapolation)
5	Viscous adiabatic wall (pressure extrapolation)
6	Viscous adiabatic wall (pressure extrapolation)
7	Viscous adiabatic wall (pressure extrapolation)
8	Farfield (Characteristic outflow w/ freestream on incoming characteristics)
9	Farfield (Characteristic outflow w/ freestream on incoming characteristics)
10	Farfield (Characteristic outflow w/ freestream on incoming characteristics)
11	Blank out region (Overlap between <i>Plate</i> and <i>Bay</i> )

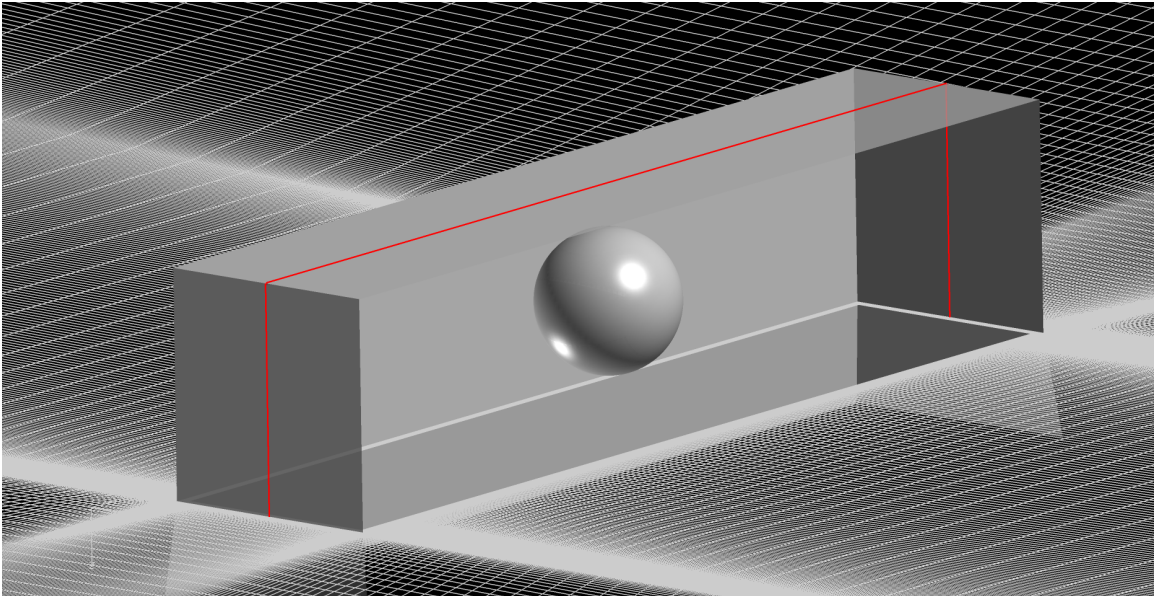


Figure 3.14: Line of interest for BC201 boundary condition

### 3.3.3 Initial Conditions.

Access to restarts and input files from the work of Flora [1] allowed swift progress to be made in setting up simulations. Since Flora used simulations at Mach 3.0, the restarts had to gradually be stepped down in speed to Mach 2.22, the experimentally determined Mach number for the Mach 2.3 nozzle. This was done through a series of input files with different Mach numbers and the `overrunmpi` script built into OVERFLOW, which allows multiple input files to be run in succession without user manipulation. Each case was run for 500 iterations, which was determined prior to beginning the ramp down to be a sufficient number of iterations to allow for grid sequencing and the stabilization of residuals. The residual history for the ramp down is shown in Figure 3.15. The flow solver settings used for this ramp down and for all subsequent tests are shown in Table 3.4. Once the proper freestream Mach number was attained, the non-dimensional Reynolds number, freestream temperature, and non-dimensional time step were altered to meet the flow conditions equivalent to experimental stagnation pressures of 4.0 psia, 3.0 psia, 2.0 psia, and 1.0 psia. Equation 3.6 shows the non-dimensional relations used and Table 3.5 shows these flow conditions. Additionally, for dynamic runs, the `Scenario.xml` and `Config.xml` files were altered to reflect the proper non-dimensionalized acceleration due to gravity, mass, and moment of inertia. Equation 2.19 shows the relationships used to generate these quantities while Table 3.6 shows the values corresponding to each stagnation pressure.

$$a_{\infty} = \sqrt{\gamma R_{air} T_{\infty}} \quad (3.6a)$$

$$V_{ref} = M_{\infty} a_{\infty} \quad (3.6b)$$

$$\Delta t^* = \Delta t \frac{V_{ref}}{L_{ref}} \quad (3.6c)$$

$$Re^* = Re L_{ref} \quad (3.6d)$$

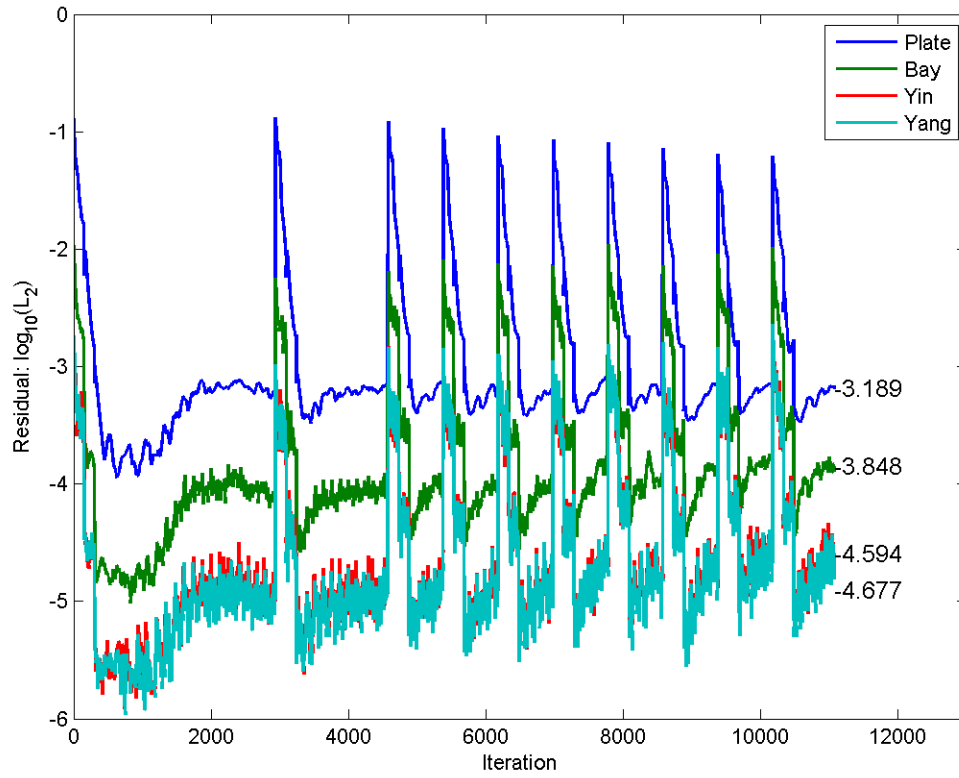


Figure 3.15: Residuals during ramp down from Mach 3.0 to Mach 2.22

Table 3.4: OVERFLOW Solver Settings

Parameter	Setting
IRHS (Numerical Method)	3rd-order HLLC Upwind Scheme
ILIMIT (Limiter)	van Albada Limiter
ILHS (Numerical Method)	SSOR (with subiterations)
NITWT (# of Newton subiterations)	5
FSONWT (Accuracy for subiterations)	2nd Order
NQT (Turbulence Model)	SST 2-equation model
IDES (DES)	DDES
FSOT (Order of turbulent convection terms)	2nd Order
VISC (Viscous terms)	All viscous terms (including cross terms)

Table 3.5: Initial Flow Parameters

Parameter	$P_t = 4.0$ psia	$P_t = 3.0$ psia	$P_t = 2.0$ psia	$P_t = 1.0$ psia
$\Delta t$ (sec)	$5.00 \times 10^{-6}$	$5.00 \times 10^{-6}$	$5.00 \times 10^{-6}$	$5.00 \times 10^{-6}$
$\Delta t^*$ (sec)	0.2923	0.2923	0.2923	0.2923
$L_{ref}$ (ft/grid unit)	0.03125	0.03125	0.03125	0.03125
$Re^*$ (grid unit $^{-1}$ )	$2.76 \times 10^4$	$2.07 \times 10^4$	$1.38 \times 10^4$	$6.89 \times 10^3$
$T_\infty$ °R	281.19	281.19	281.19	281.19

Table 3.6: Non-dimensional Mass Properties

Parameter	$P_t = 4.0$ psia	$P_t = 3.0$ psia	$P_t = 2.0$ psia	$P_t = 1.0$ psia
$g^*$	$3.01 \times 10^{-7}$	$3.01 \times 10^{-7}$	$3.01 \times 10^{-7}$	$3.01 \times 10^{-7}$
$m^*$	$1.44 \times 10^5$	$1.92 \times 10^5$	$2.88 \times 10^5$	$5.77 \times 10^5$
$I_{zz}^*$	$9.01 \times 10^4$	$1.20 \times 10^5$	$1.80 \times 10^5$	$3.60 \times 10^5$



## IV. Results

### 4.1 Nozzle Characterization

For all nozzles, multiple tests were conducted at stagnation pressures ranging from 6 psia to 20 psia. The lowest setting of 6 psia corresponds to the lowest stagnation pressure previously documented. Nozzles are referred to interchangeably by their nominal Mach number or their experimentally determined Mach number.

#### 4.1.1 *Mach 3.0.*

As an initial verification of correct tunnel operation, the pre-existing Mach 3 nozzle was tested. Previous testing by many others found the nozzle to yield flow of Mach 2.9 and 2.94 [1, 29].

In the current study, the nominal Mach 3 nozzle is found to have an average Mach number of 2.96 with a standard deviation of 0.06, leading to a 95% confidence interval of [2.84, 3.08]. This was determined over four tests. Table 4.1 shows the test conditions for each of these tests and indicates a possible minor influence on the Mach number due to Reynolds number. Figure 4.1 shows the normalized probability density function (PDF) of each test as well as the combined data. All of the data is weighted equally, however, some tests result in more data due to a longer tunnel run time. This accounts for the unequal PDF results. While each test has a normal distribution with a small standard deviation, the result as a whole has a distinctly non-normal distribution. Possible causes of this bi- or tri-modal distribution are a non-significant number of tests (four), a dependence on stagnation pressure, or an outlier data point, possibly caused by a leak or other hardware problem. Comparison of stagnation pressures with average Mach numbers for other nozzles shows no correlation between stagnation pressure and Mach number, possibly due to reduced sensitivity to Reynolds number.

In addition, Schlieren photography can be used to qualitatively determine the Mach number. Images were opened in Adobe® Photoshop CS5®, where the flat plate prior to the cavity was used as a rule line to straighten the picture. Then, the shock angle was determined using Photoshop’s Ruler Tool and verified using trigonometry. Figure 4.2 shows a sample Schlieren image with the lines used for verification and the angle marked. The angle of 19.6 degrees corresponds to a freestream Mach of 2.98, consistent with the quantitative data.

Several tests were conducted with various restrictions on the pressure-side valve, shown in Figure 3.1. This resulted in a decrease of stagnation pressure due to insufficient high pressure air. These tests were conducted to test whether supersonic flow could be sustained in the tunnel at stagnation pressures lower than 6 psia. The choked flow remained supersonic but could not sustain a constant stagnation pressure. For these reasons, these tests were not included in the analysis of the Mach number.

Table 4.1: Flow properties for Mach 3 Nozzle Experiments

Test	$M_\infty (\bar{x} \pm 2\sigma)$	$P_t$ (psia)	$Re_\infty$ (ft <sup>-1</sup> )	$U_\infty$ (ft/s)
1-3	Preliminary Test Runs			
4	$2.87 \pm 0.03$	15.72	$2.49 \times 10^6$	2043
5	$2.94 \pm 0.03$	8.45	$1.31 \times 10^6$	2054
6	$3.01 \pm 0.04$	6.16	$9.17 \times 10^5$	2072
7	$2.99 \pm 0.04$	6.57	$9.94 \times 10^5$	2064

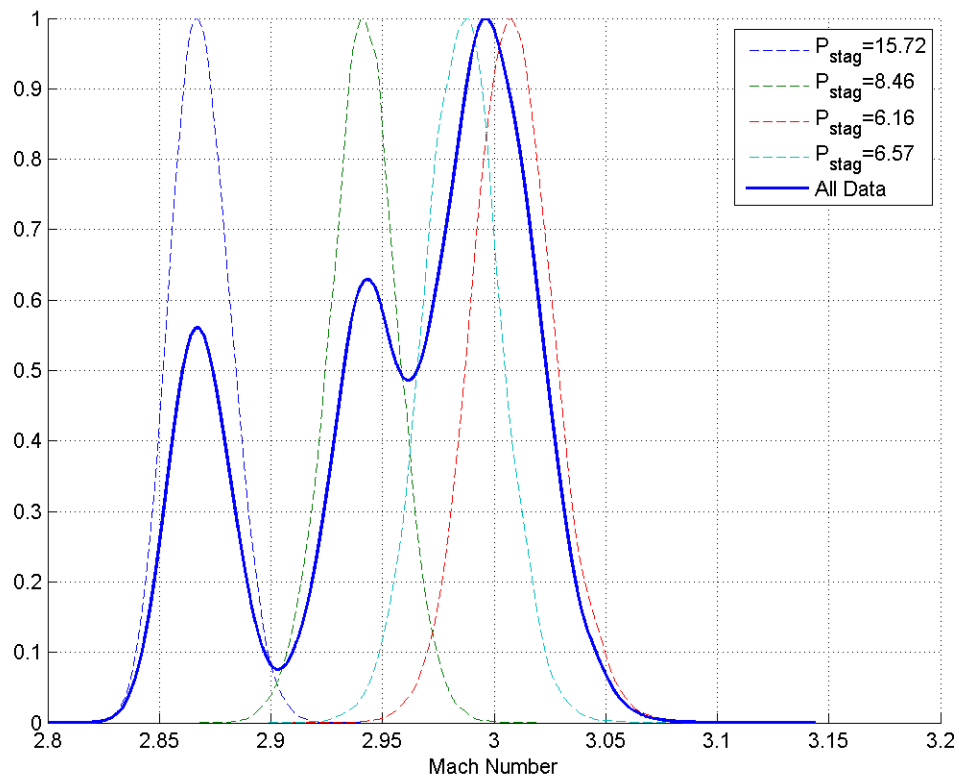


Figure 4.1: Normalized PDF of Mach 3 Nozzle Tests

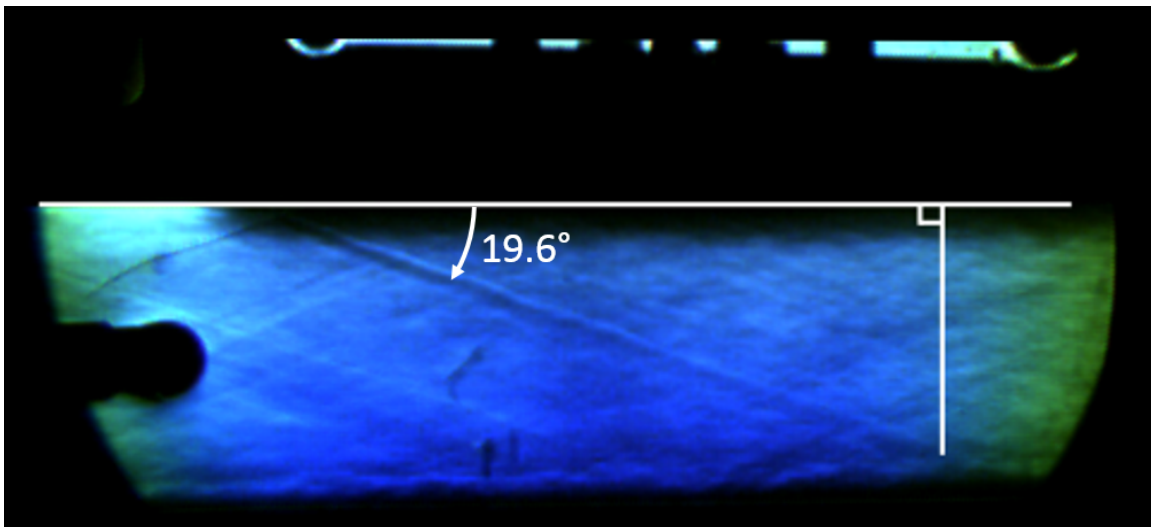


Figure 4.2: Qualitative determination of Mach number for Mach 3 nozzle using Schlieren photography

#### **4.1.2 Mach 2.3.**

The Mach 2.3 nozzle is found to have an average Mach number of 2.22 with a standard deviation of 0.02, resulting in a 95% confidence interval of [2.18, 2.26]. Since this nozzle had never been tested before, a greater number of tests were conducted, with eight tests contributing to the average. The PDF of these tests, as well as the combined PDF, is shown in Figure 4.3 while the test conditions are shown in Table 4.2. The data for this nozzle is much more tightly grouped despite a larger range of stagnation pressures. This is indicative of repeatability, especially since the tests took place over a range of days and times. Qualitative analysis of Schlieren imagery yielded a Mach angle of 26.2 degrees, which corresponds with a freestream Mach number of 2.27, verifying the quantitative data. Figure 4.4 shows a sample Schlieren image. Differences in brightness and contrast in Schlieren images is likely due to minor movements of the knife edge in order to better resolve the leading edge shock. In one test run, large anomalies were observed. During this run, the transducer leads appeared to contact the diffuser walls. After ensuring that the wiring contacts for the transducers were free of interference, repeat tests did not show anomalies. Therefore, the outlying results were omitted from the analysis.

The flow exiting the nozzle appears to have a relatively small boundary layer. Analytical predictions place the boundary layer thickness between 0.088 inches and 0.111 inches, averaging 0.096 inches for the eight tests used. Schlieren data supports this estimate. Figure 4.5 shows images from tests 7 and 8, each predicting a boundary layer thickness of approximately 0.1 inches.

Table 4.2: Flow properties for Mach 2.3 Nozzle Experiments

Test	$M_\infty (\bar{x} \pm 2\sigma)$	$P_t$ (psia)	$Re_\infty$ (ft <sup>-1</sup> )	$U_\infty$ (ft/s)
1	$2.23 \pm 0.02$	16.37	$3.60 \times 10^6$	1829
2	$2.22 \pm 0.02$	16.87	$3.69 \times 10^6$	1832
3	$2.23 \pm 0.02$	18.15	$3.97 \times 10^6$	1833
4	$2.22 \pm 0.03$	5.59	$1.25 \times 10^6$	1818
5	$2.24 \pm 0.03$	19.07	$4.15 \times 10^6$	1837
6	$2.23 \pm 0.02$	14.05	$3.09 \times 10^6$	1829
7	DAQ error due to wiring			
8	$2.22 \pm 0.02$	11.84	$2.63 \times 10^6$	1822
9	$2.21 \pm 0.03$	6.22	$1.40 \times 10^6$	1813

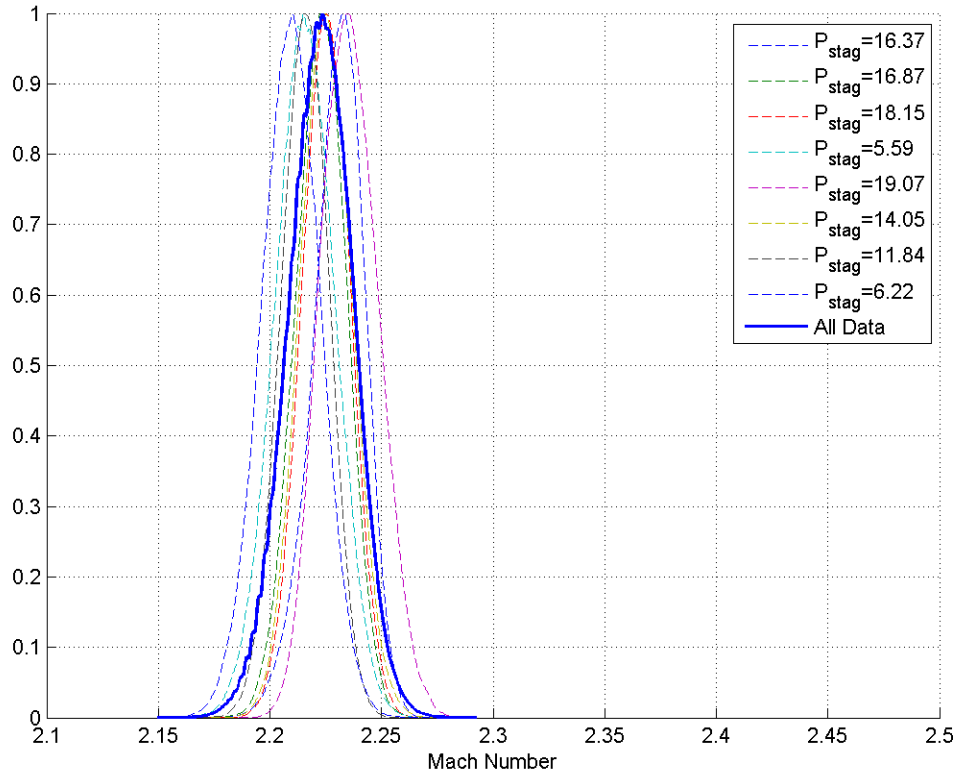


Figure 4.3: Normalized PDF of Mach 2.3 Nozzle Tests

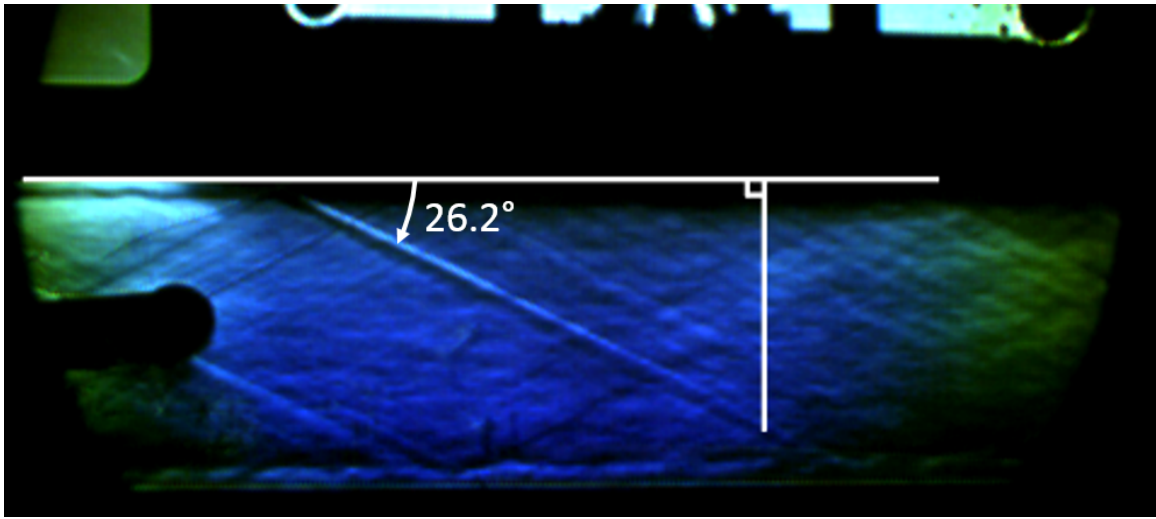
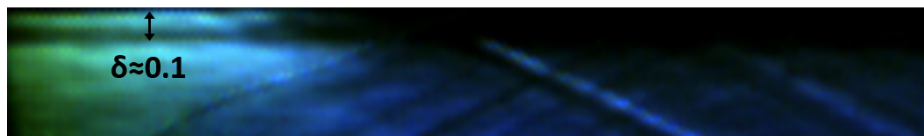
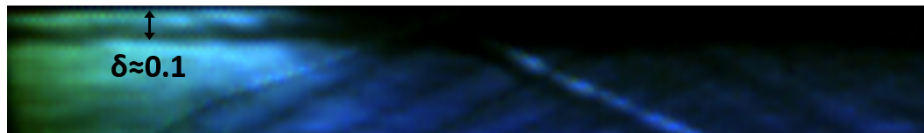


Figure 4.4: Qualitative determination of Mach number for Mach 2.3 nozzle using Schlieren photography



(a) Test: 2



(b) Test: 3

Figure 4.5: Qualitative Boundary Layer Estimation for Mach 2.22

#### 4.1.3 Mach 1.9.

The Mach 1.9 nozzle resulted in a tightly grouped series of PDF's for each test, similar to that of the Mach 2.3 nozzle. The average Mach number is 1.84 with a standard deviation of 0.01, resulting in a 95% confidence interval of [1.82, 1.86]. Table 4.3 shows the flow conditions of the individual runs and Figure 4.6 shows the PDF of each test as well as the data as a whole. Five tests contributed to the average Mach. No data was collected near a stagnation pressure of 20 psi because insufficient run times would be produced. Qualitative analysis of Schlieren imagery provided a shock angle of 32.4 degrees, corresponding to a freestream Mach number of 1.87, verifying the quantitative data. Figure 4.7 shows a sample Schlieren image. Several of the tests were initially attempted with a compressor pressure of 120 psi, but acquired data suggested that the tunnel unstated early in those experiments. When the compressor pressure was increased to 180 psi, the problem was prevented for stagnation pressures up to at least 13.6 psia, and those results are presented.

Table 4.3: Flow properties for Mach 1.9 Nozzle Experiments

Test	$M_\infty (\bar{x} \pm 2\sigma)$	$P_t$ (psia)	$Re_\infty$ (ft <sup>-1</sup> )	$U_\infty$ (ft/s)
1	$1.83 \pm 0.02$	13.63	$3.52 \times 10^6$	1652
2	Variable stagnation pressure			
3-4	DAQ error due to wiring			
5	$1.84 \pm 0.02$	10.62	$2.76 \times 10^6$	1648
6	$1.83 \pm 0.03$	5.86	$1.55 \times 10^6$	1635
7	$1.84 \pm 0.02$	10.33	$2.68 \times 10^6$	1650
8	$1.84 \pm 0.02$	10.25	$2.67 \times 10^6$	1648

The flow exiting the nozzle appears to have a relatively small boundary layer. Analytical predictions place the boundary layer thickness between 0.090 inches and

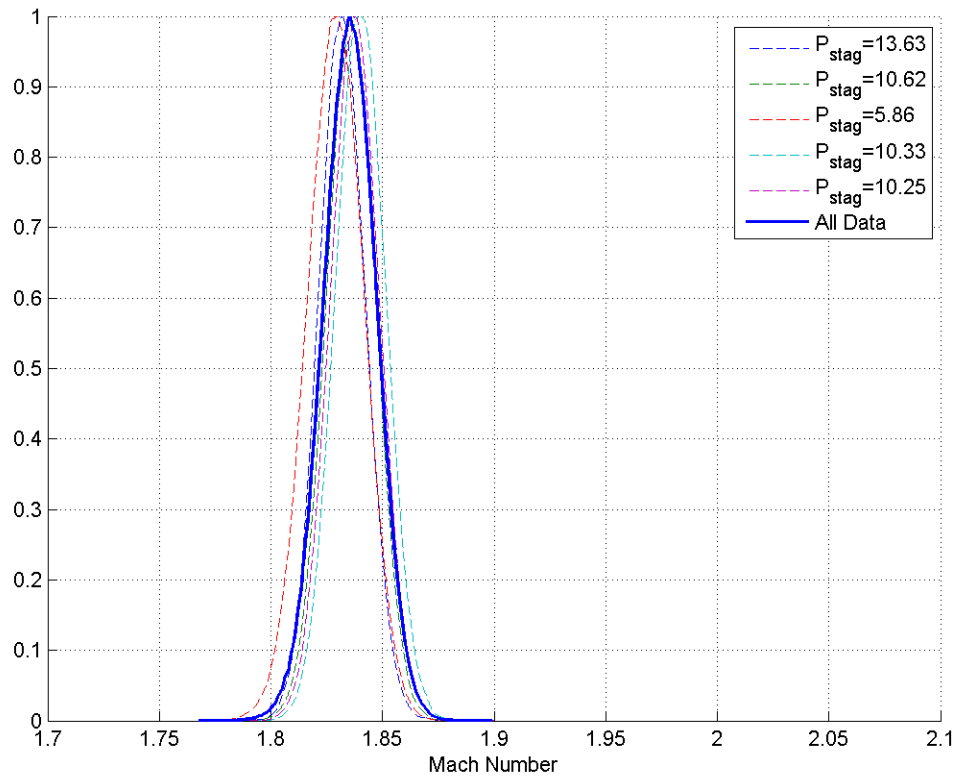


Figure 4.6: Normalized PDF of Mach 1.9 Nozzle Tests

0.106 inches, averaging 0.096 inches for the five tests used. Schlieren data supports this estimate. Figure 4.8 shows images from tests 7 and 8, each predicting a boundary layer thickness of approximately 0.1 inches.



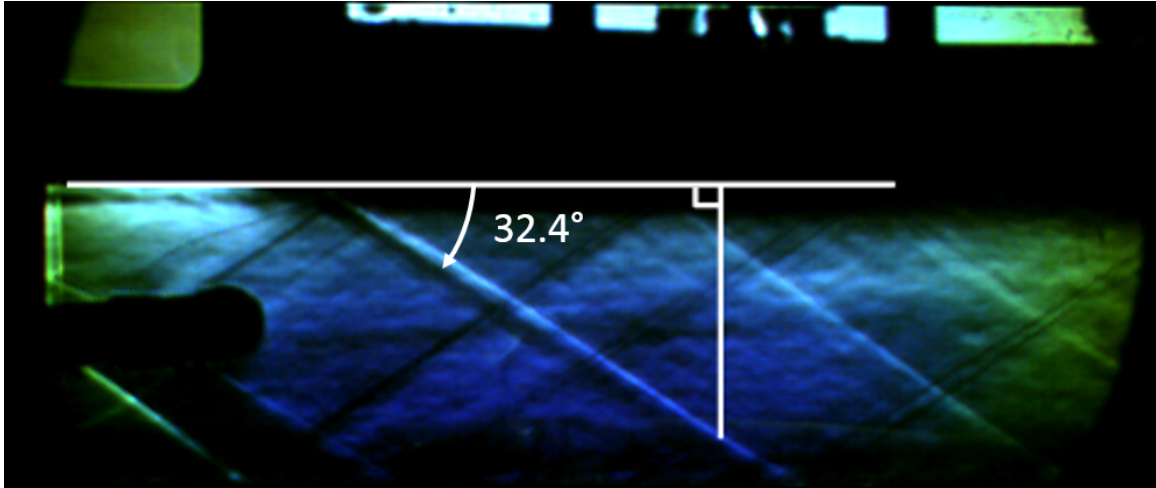
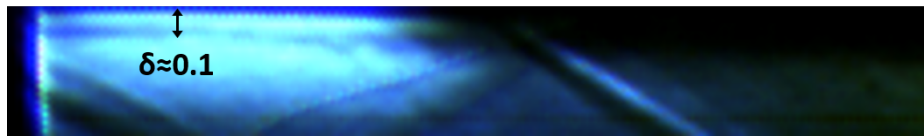
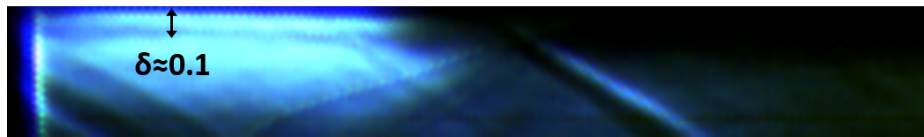


Figure 4.7: Qualitative determination of Mach number for Mach 1.9 nozzle using Schlieren photography



(a) Test: 7



(b) Test: 8

Figure 4.8: Qualitative Boundary Layer Estimation for Mach 1.84

#### 4.1.4 Mach 1.5.

The nominal Mach 1.5 nozzle produced data similar in character to that of the Mach 1.9 and Mach 2.3 nozzles, but with slightly more variation. Six tests produced an average Mach number of 1.43 with a standard deviation of 0.03 for a 95% confidence interval of [1.37, 1.49]. Table 4.4 shows the flow conditions for the tests used in producing the average Mach and Figure 4.9 shows the PDF of each test as well as the combined PDF.

No data was collected for 20 psi stagnation pressure due to insufficient run times, even at the increased compressor air pressure of 180 psi. Furthermore, the data from a stagnation pressure of 6 psi was disregarded because tunnel conditions resulted in a normal shock that oscillated across the static port resulting in widely varying Mach numbers clustered around 1.1. Figure 4.10 shows the time history of the Mach number for the 6 psi case, illustrating the effect of the oscillating normal shock on the Mach number while Figure 4.11 shows Schlieren photography of this phenomenon.

Table 4.4: Flow properties for Mach 1.5 Nozzle Experiments

Test	$M_\infty (\bar{x} \pm 2\sigma)$	$P_t$ (psia)	$Re_\infty$ (ft <sup>-1</sup> )	$U_\infty$ (ft/s)
1	$1.41 \pm 0.03$	14.44	$3.92 \times 10^6$	1429
2	$1.43 \pm 0.03$	15.21	$4.11 \times 10^6$	1440
3	$1.41 \pm 0.03$	10.43	$2.92 \times 10^6$	1415
4	Oscillating normal shock			
5	$1.44 \pm 0.04$	10.91	$3.03 \times 10^6$	1432
6	$1.42 \pm 0.03$	11.83	$3.28 \times 10^6$	1425
7	$1.47 \pm 0.06$	14.64	$3.94 \times 10^6$	1470

The flow exiting the nozzle appears to have a relatively small boundary layer. Analytical predictions place the boundary layer thickness between 0.091 inches and 0.098 inches, averaging 0.094 inches for the six tests used. Schlieren data supports this estimate. Figure 4.12 shows images from tests 7 and 8, each predicting a boundary layer thickness of approximately 0.1 inches.

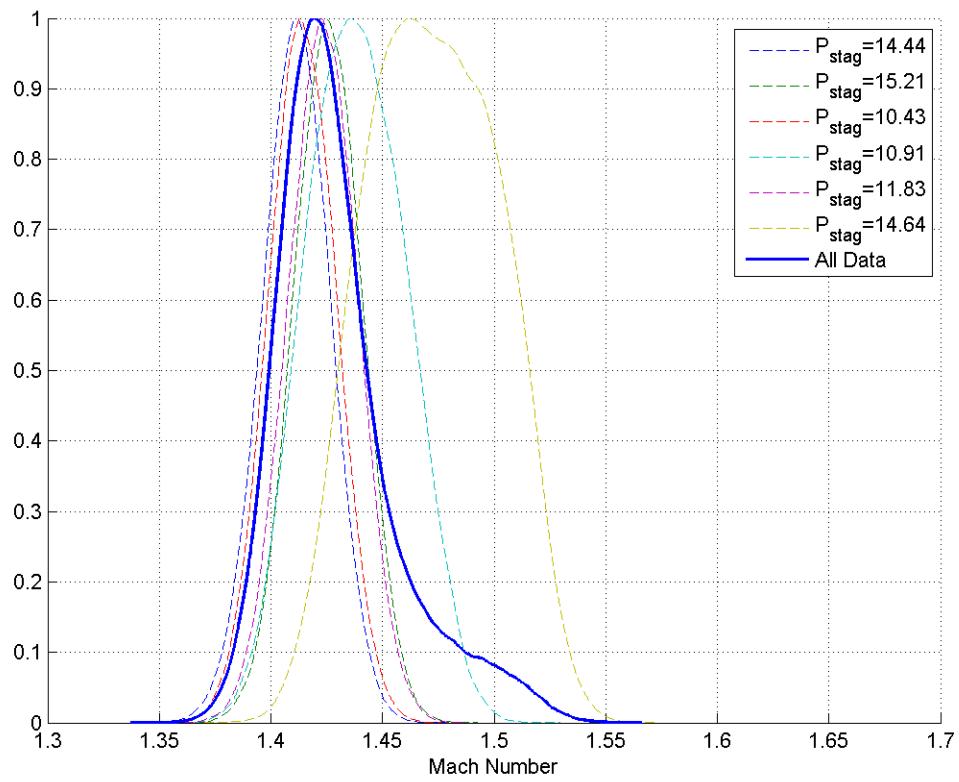


Figure 4.9: Normalized PDF of Mach 1.5 Nozzle Tests

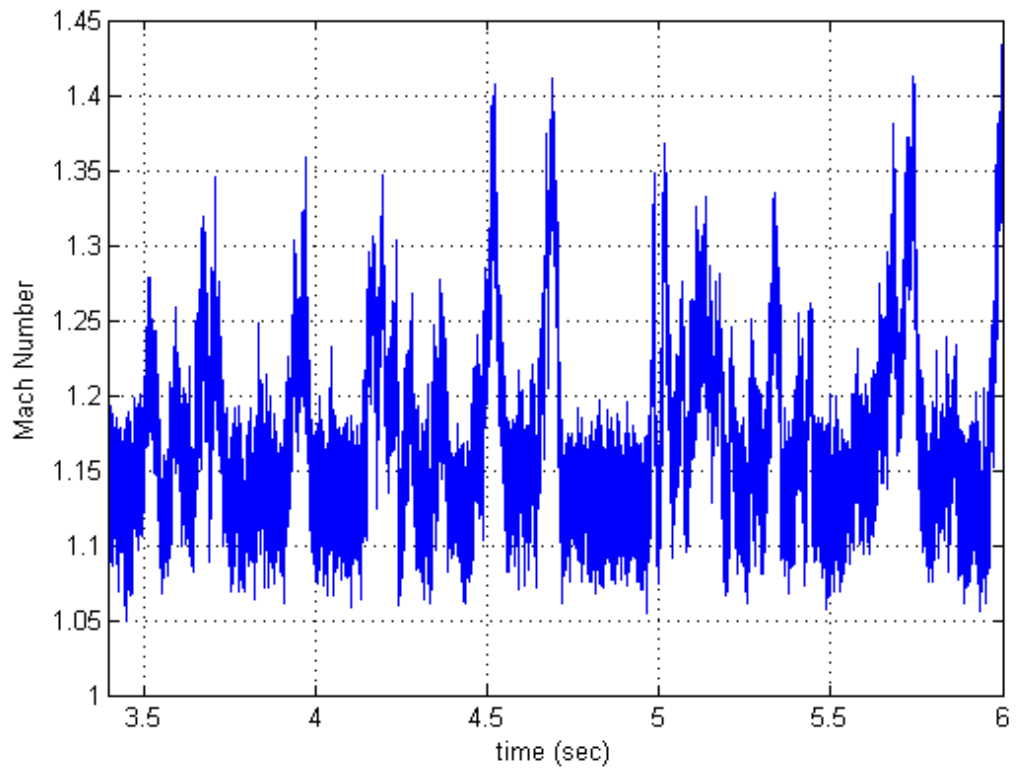


Figure 4.10: Time History of Mach number for  $P_0 = 6psi$

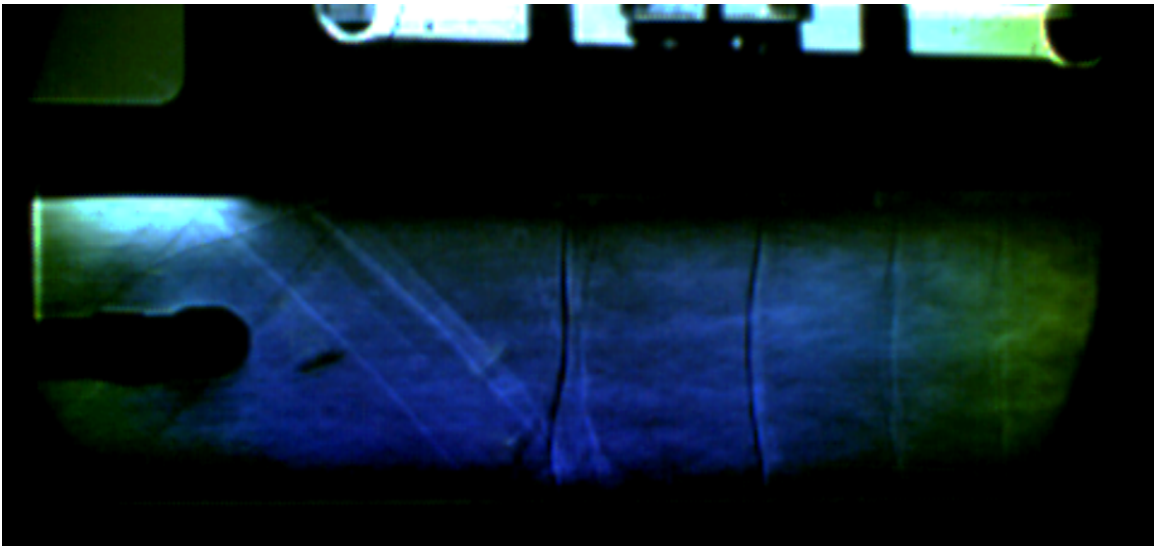
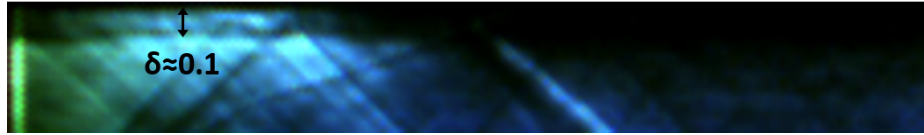
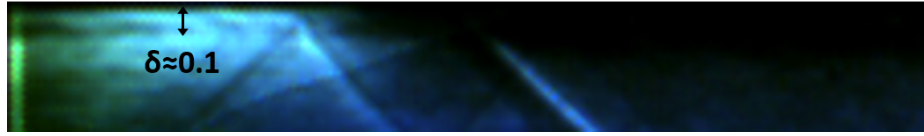


Figure 4.11: Normal Shock across static port for Mach 1.5 nozzle at  $P_0 = 6psi$



(a) Test: 1



(b) Test: 2

Figure 4.12: Qualitative Boundary Layer Estimation for Mach 1.43

## 4.2 Cavity Environment

The cavity environment is characterized through the comparison of peak frequencies of experimental pressure spectrum data with analytically predicted Rossiter modes. Relative noise levels and the effects of Reynolds number on peak noise levels is also examined. Additionally, flow variables are calculated using an assumed Mach number equal to the average Mach number determined in Section 4.1 for each nozzle. Nozzles are referred to interchangeably by their nominal Mach number and experimentally determined Mach number.

### 4.2.1 *Mach 3.0.*

Characterization of the cavity in Mach 3 flow has already been conducted by Bjorge et al [29] and Flora [1]. Therefore, matching the Rossiter modes seen in these previous works will serve as verification of correct methods. Initially, peak amplitudes and broadband noise levels of the cavity spectra were seen to be significantly different from those presented in Flora [1]. After thorough scrutiny of both methods of data reduction, an error in the amplitude of the sound pressure level (SPL) was discovered in Flora's calculations. Since most of Flora's discussion and analysis deals with the frequency content of the signal, which was not directly affected by the error, the data presented in Flora [1] is still significant. After correcting this error, the amplitude of the spectra were much more closely matched. Figure 4.13 shows the results of all cavity tests. This indicates a dependency between noise levels and stagnation pressure that is much more visible than at other Mach numbers. This is likely due to the higher dynamic pressures at Mach 2.96. Figure 4.14 shows each test and the calculated Rossiter modes for each test. Table 4.5 shows the flow conditions for each of the tests.

At Mach 2.96, only the second through fifth Rossiter modes are clearly displayed. The first mode shows only slight indications of its existence while the sixth mode does not present at all. The third and fourth modes are presented very distinctly and correspond

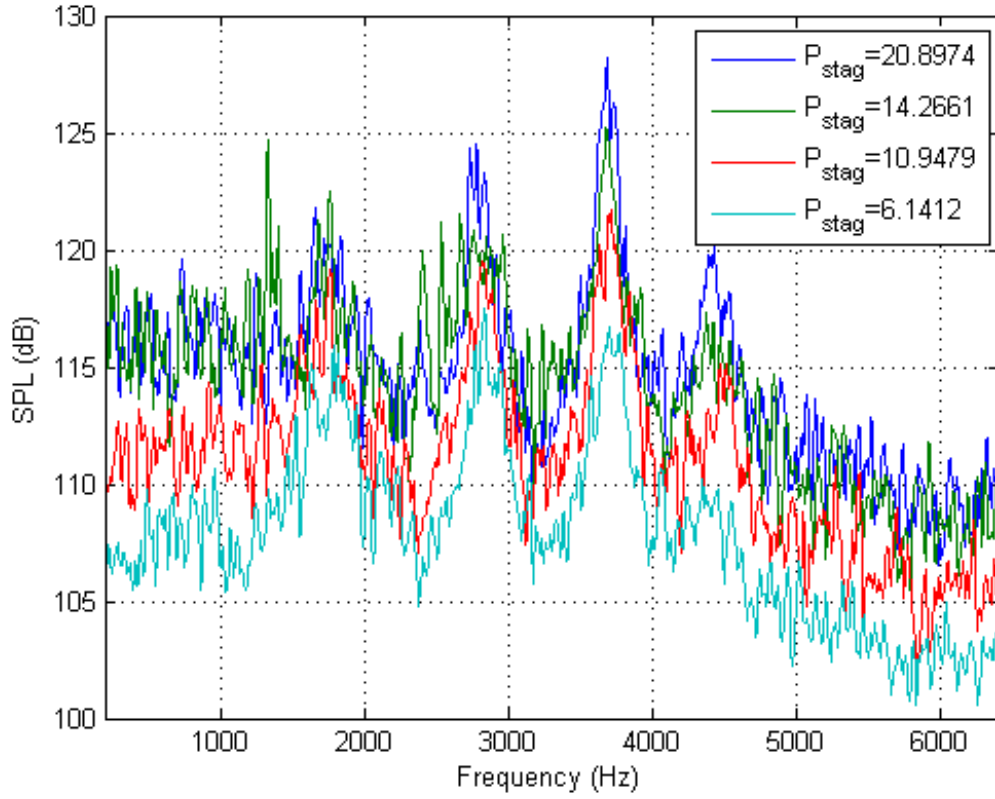
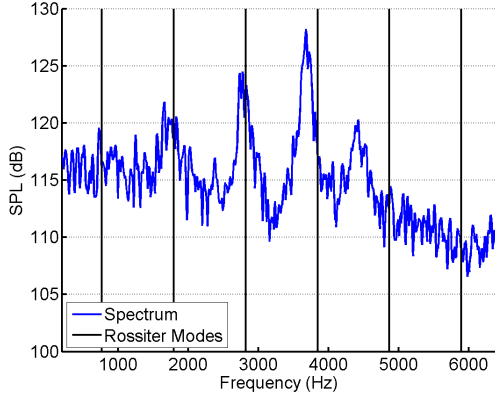


Figure 4.13: Cavity Spectra for all Mach 2.96 Tests

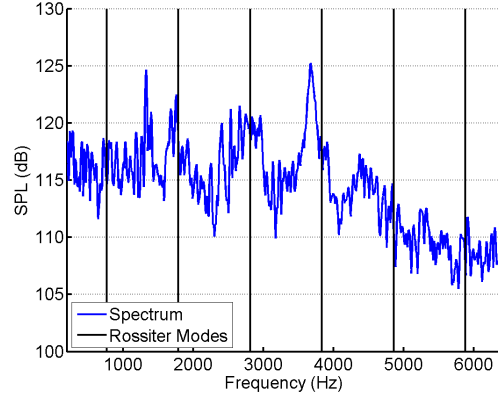
Table 4.5: Flow Conditions for Mach 2.96 Cavity Tests

Test	$P_t$ (psia)	$U_\infty$ (ft/s)	$Re_\infty$ (ft <sup>-1</sup> )
1	20.90	2042	$3.28 \times 10^6$
2	14.27	2037	$2.25 \times 10^6$
3	10.95	2035	$1.74 \times 10^6$
4	6.14	2027	$9.85 \times 10^5$

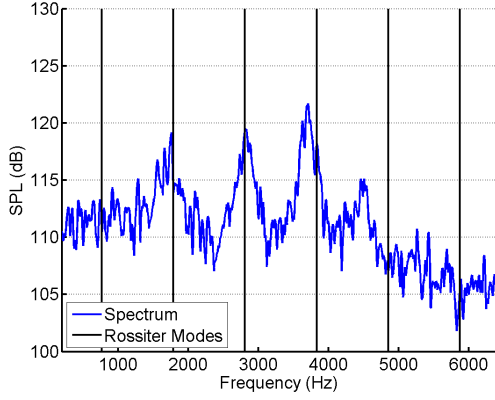
closely to the modes predicted by Equation 2.2. The second mode is somewhat obscured by the broadband noise and seems slightly diffused. The fifth mode presents a clear peak but consistently shows a significant amount of deviation from the predicted Rossiter



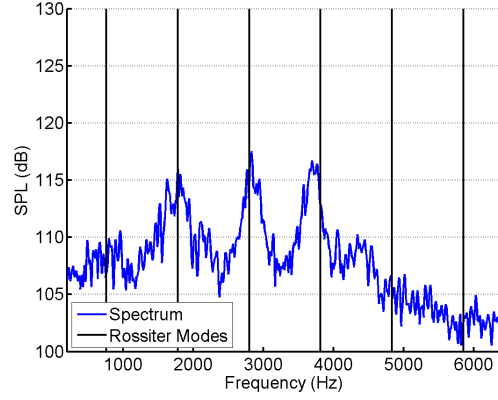
(a)  $P_0 = 20.90$



(b)  $P_0 = 14.27$



(c)  $P_0 = 10.95$



(d)  $P_0 = 6.14$

Figure 4.14: Rossiter modes for individual Mach 2.96 Tests

modes. The average difference between the predicted Rossiter mode and the corresponding observed mode for the second through fifth modes is 176.48 Hz. Table 4.6 shows the average difference between each predicted and observed mode for all tests. More detailed tables concerning the predicted and observed Rossiter modes can be found in Appendix F.



Table 4.6: Average Difference per Rossiter Mode for Mach 2.96

Mode	Average Difference (Hz)	Average % Difference
2	155.53	8.69
3	40.12	1.43
4	144.71	3.77
5	347.31	7.15

#### 4.2.2 *Mach 2.3.*

The Mach 2.3 nozzle configured for cavity characterization presents the Rossiter modes extremely well, with 6 modes presenting fully in the range from 0 to 6.4 kHz and the 7th presenting at the very boundary of this range. Figure 4.15 shows the results of all cavity tests. There is a small trend of decreasing SPL with decreasing stagnation pressure, which is attributable to the lower dynamic pressure. Additionally, the 18 psia stagnation pressure test does not follow the trend. Figure 4.16 shows each test and the Rossiter modes calculated for each test. Due to small changes in temperature between tests, the Rossiter modes are not constant for all tests, but the variation is quite small. Table 4.7 shows the flow conditions for each of the tests. Mach number is assumed to be 2.22, as determined by the nozzle characterization tests discussed in Section 4.1.

The difference between each predicted Rossiter mode and the corresponding observed mode averages -17.03 Hz. Table 4.8 shows the average difference between each predicted mode and the observed mode for all tests. More detailed tables concerning the predicted and observed Rossiter modes can be found in Appendix F.

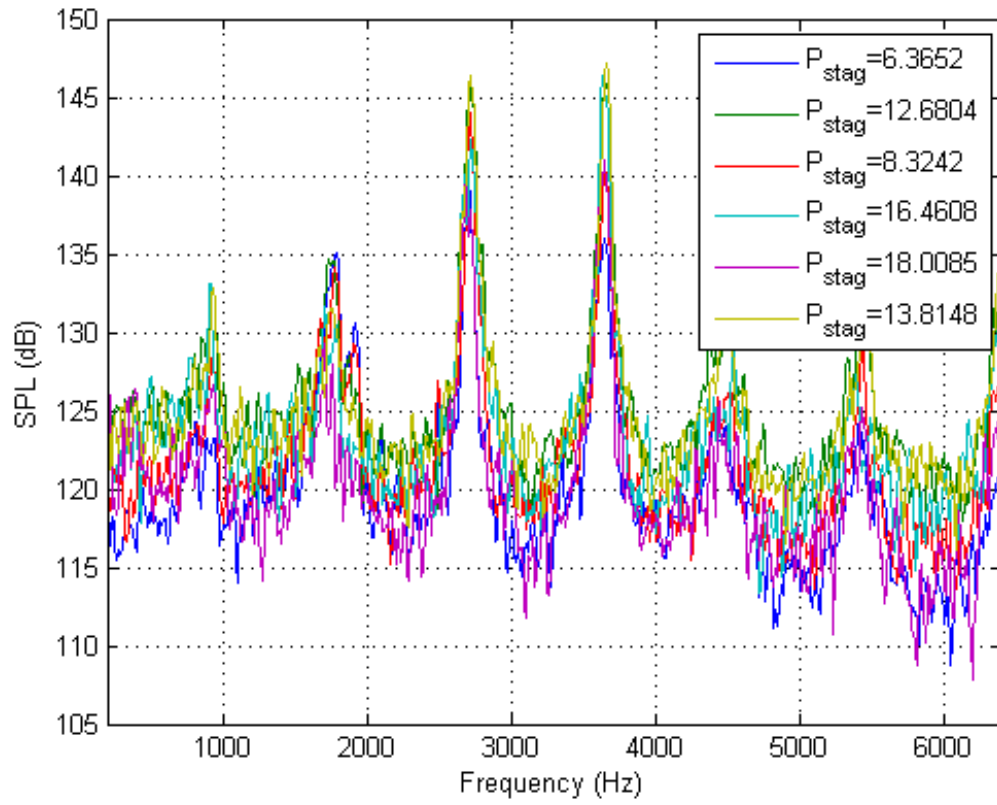
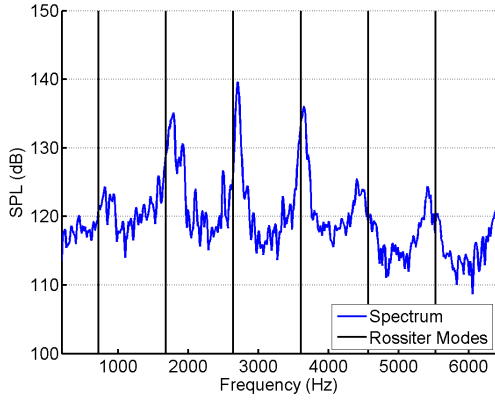


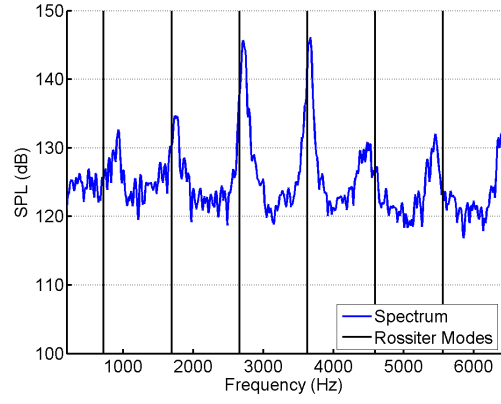
Figure 4.15: Cavity Spectra for all Mach 2.22 Tests

Table 4.7: Flow Conditions for Mach 2.22 Cavity Tests

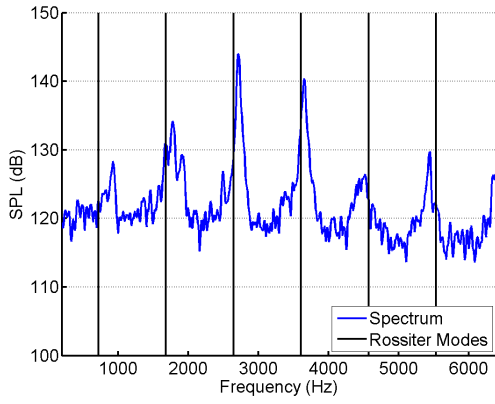
Test	$P_t$ (psia)	$U_\infty$ (ft/s)	$Re_\infty$ ( $\text{ft}^{-1}$ )
1	Tunnel Configuration Error		
2	6.37	1802	$1.46 \times 10^6$
3	12.68	1813	$2.86 \times 10^6$
4	8.32	1805	$1.90 \times 10^6$
5	16.46	1817	$3.69 \times 10^6$
6	18.01	1821	$4.01 \times 10^6$
7	13.81	1814	$3.11 \times 10^6$



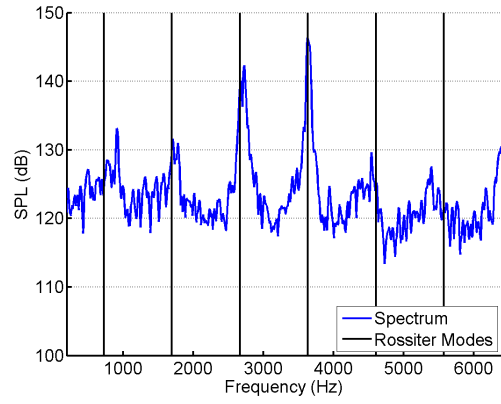
(a)  $P_t = 6.37$



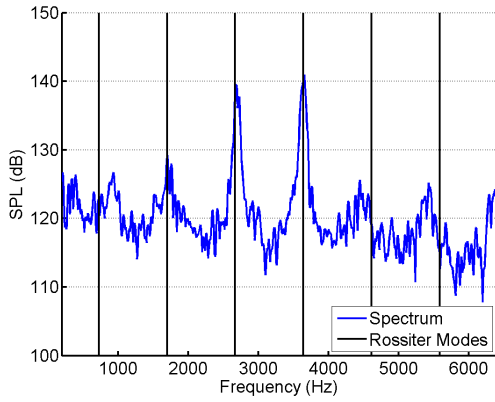
(b)  $P_t = 12.68$



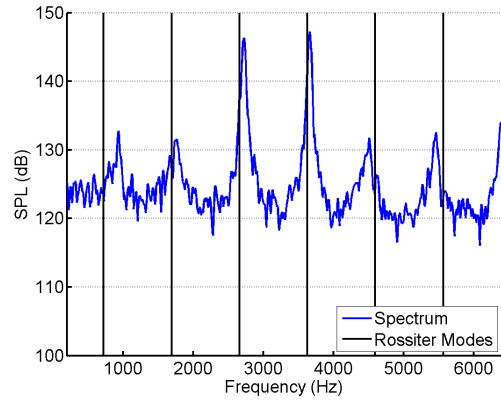
(c)  $P_t = 8.32$



(d)  $P_t = 16.46$



(e)  $P_t = 18.01$



(f)  $P_t = 13.81$

Figure 4.16: Rossiter modes for individual Mach 2.22 Tests

Table 4.8: Average Difference per Rossiter Mode for Mach 2.22

Mode	Average Difference (Hz)	Average % Difference
1	-185.26	-25.5
2	-55.39	-3.3
3	-52.18	-2.0
4	-28.98	-0.8
5	92.89	2.0
6	126.77	2.3

### 4.2.3 Mach 1.9.

The Mach 1.9 nozzle configured for cavity characterization presents 6 modes in a similar fashion to the Mach 2.3 nozzle, with the 7th visible at the boundary of the range of frequencies analyzed. Figure 4.17 shows the spectra for all cavity tests at Mach 1.84. One test, the 5 psia test, shows a noticeable decrease in SPL, however, the other tests are tightly clustered despite variation in stagnation pressure. The lack of data at higher stagnation pressures may be masking the true effect of decreasing stagnation pressure for this nozzle, as 12 psia was the highest stagnation pressure tested. Figure 4.18 shows the spectra and Rossiter modes for each test. Table 4.9 shows the flow conditions for each of these tests. Mach number is assumed to be 1.84.

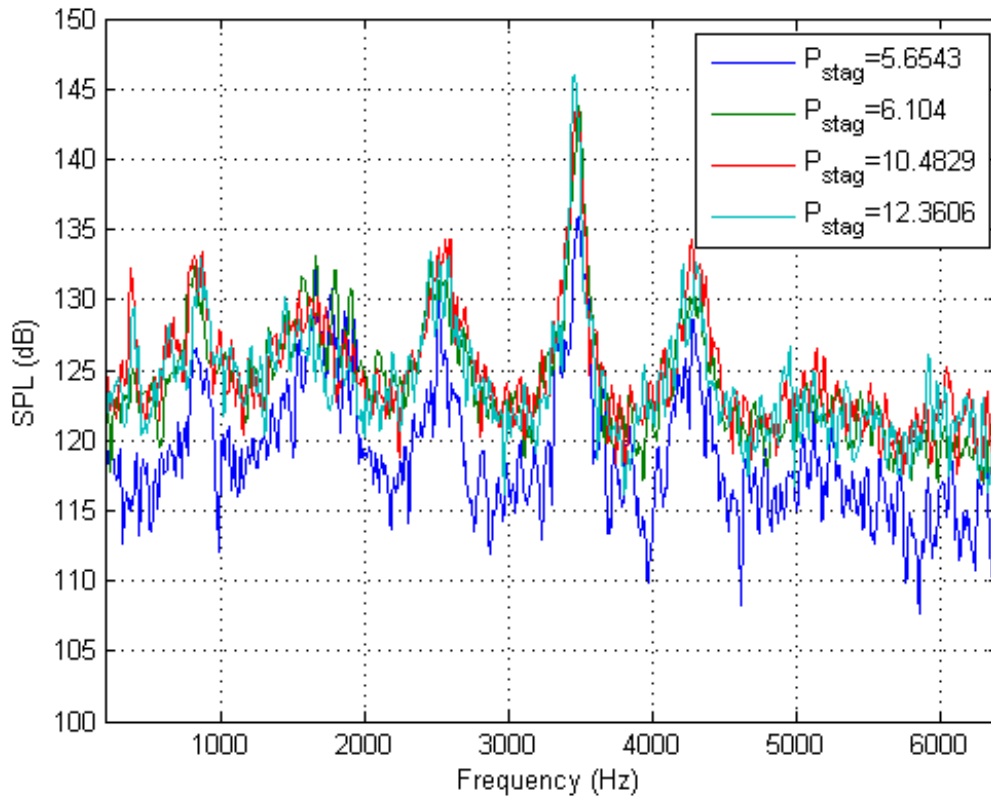
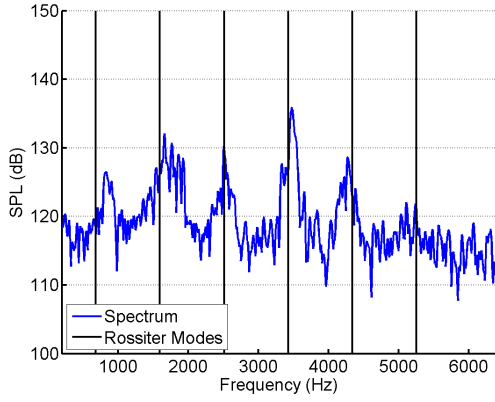
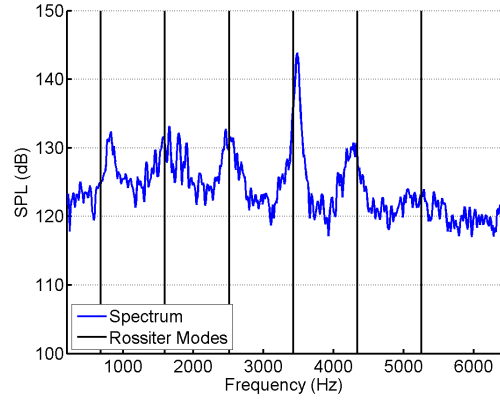


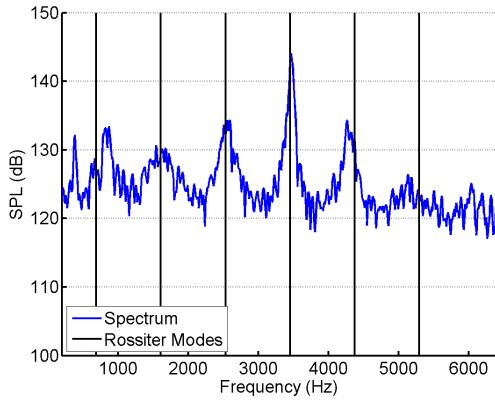
Figure 4.17: Cavity Spectra for all Mach 1.84 Tests



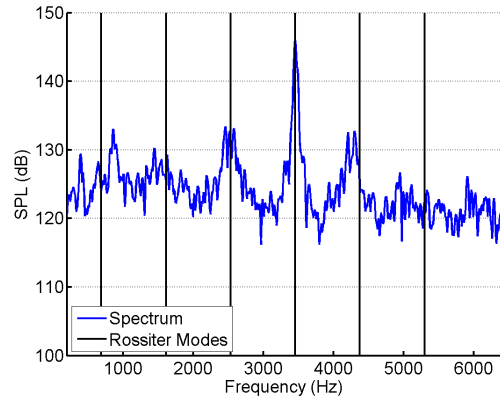
(a)  $P_t = 5.65$



(b)  $P_t = 6.10$



(c)  $P_t = 10.48$



(d)  $P_t = 12.36$

Figure 4.18: Rossiter modes for individual Mach 1.84 Tests

The difference between each predicted Rossiter mode and the observed mode averaged 5.44 Hz. Table 4.10 shows the difference for each mode, averaged over the four tests used. More detailed tables concerning the predicted and observed Rossiter modes can be found in Appendix F.

Table 4.9: Flow Conditions for Mach 1.84 Cavity Tests

Test	$P_t$ (psia)	$U_\infty$ (ft/s)	$Re_\infty$ (ft <sup>-1</sup> )
1	No frequency data collected		
2	5.65	1631	$1.51 \times 10^6$
3	6.10	1632	$1.63 \times 10^6$
4	10.48	1644	$2.74 \times 10^6$
5	12.36	1646	$3.23 \times 10^6$

Table 4.10: Average Difference per Rossiter Mode for Mach 1.84

Mode	Average Difference (Hz)	Average % Difference
1	-157.59	-22.9
2	-53.71	-3.3
3	24.17	1.0
4	-27.95	-0.8
5	75.93	1.7
6	171.81	3.3

#### 4.2.4 Mach 1.5.

The pressure measurements in the cavity for the Mach 1.5 nozzle show considerably more broadband noise than a typical spectrum. The presence of a rebounded shock from the tunnel floor and/or a normal shock disrupts the periodic oscillations, causing higher SPL's at lower frequencies. It also results in higher broadband noise. While most of the frequency content is disrupted, local peaks in the SPL occur at the first two modes, with smaller local peaks visible for some higher modes. Figure 4.19 shows all the spectra of cavity tests at Mach 1.43. Only two stagnation pressures were tested, as discussed in Section 4.1.

Figure 4.20 shows the spectrum of each test and the predicted Rossiter modes. Table 4.11 shows the flow conditions for each test.

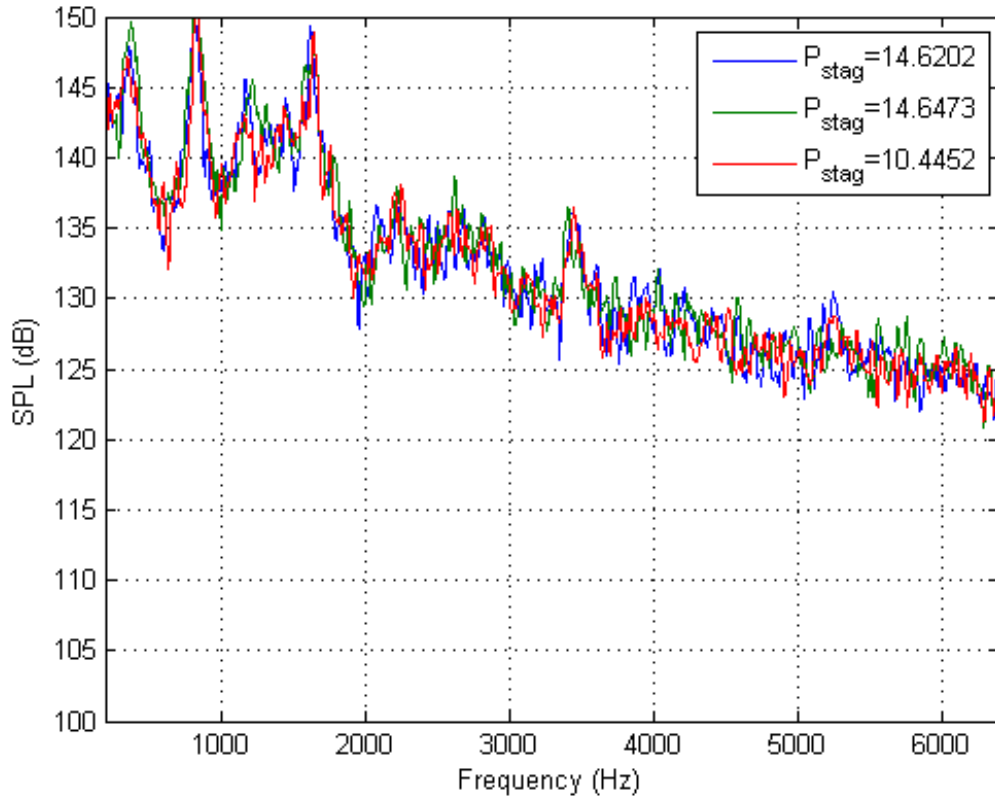
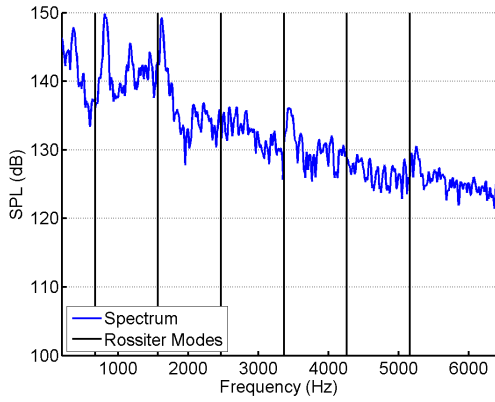


Figure 4.19: Cavity Spectra for all Mach 1.43 Tests

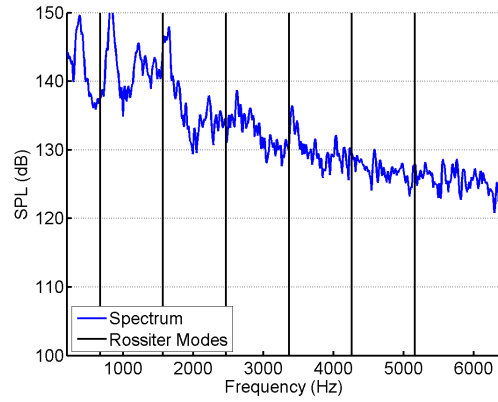
Table 4.11: Flow Conditions for Mach 1.43 Cavity Tests

Test	$P_t$ (psia)	$U_\infty$ (ft/s)	$Re_\infty$ ( $\text{ft}^{-1}$ )
1	14.62	1494	$3.61 \times 10^6$
2	14.65	1494	$3.61 \times 10^6$
3	10.45	1460	$2.74 \times 10^6$

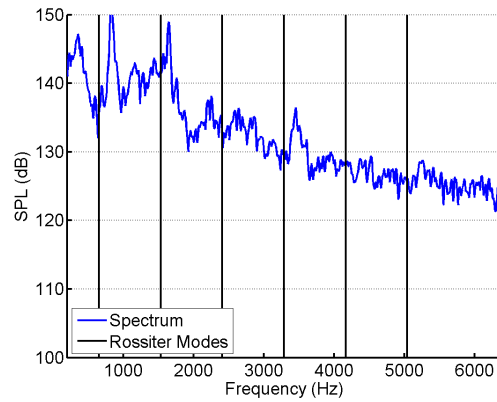




(a)  $P_t = 14.62$



(b)  $P_t = 14.65$



(c)  $P_t = 10.45$

Figure 4.20: Rossiter modes for individual Mach 1.43 Tests

The first four modes are distinguishable from the noise, with an average difference between observed and predicted modes of -176.81 Hz. The 3rd and 4th modes are significantly attenuated, with the visibility of the third mode being questionable. Table 4.12 shows the average difference between the observed and predicted modes for each mode, averaged across all three tests. More detailed tables concerning the predicted and observed Rossiter modes can be found in Appendix F.

Table 4.12: Average Difference per Rossiter Mode for Mach 1.43

Mode	Average Difference (Hz)	Average % Difference
1	-155.67	-23.3
2	-83.24	-5.3
3	-200.13	-8.17
4	-159.26	-3.26

### 4.3 Drop Testing

Drop testing was conducted in both an experimental and a computational setting. A freestream Mach number of 2.22, in accordance with the experimentally determined Mach number of the Mach 2.3 nozzle, was used for both cases. Stagnation pressures as low as 1.0 psia were utilized in an attempt to produce a successful release of the store from the bay. All trajectory traces track the center of mass of the sphere. Heavy Mach Scaling was used to determine comparable real world conditions.

#### 4.3.1 *Experimental.*

Stagnation pressures of approximately 7.5 psia, 3.5 psia, and 1.0 psia were utilized in experiments. Table 4.13 shows the flow conditions for each test. The lower stagnation pressure of 3.5 psia was likely achieved from a better seal between the nozzle and the other tunnel components, allowing a more complete vacuum to be drawn by the vacuum pump. The stagnation pressure of 1.0 psia was achieved through the use of a vacuum pump connected to the Regulating valve as discussed in 3.1.3.

Due to imperfections in the stores and the fragile nature of ice, some tests did not produce viable video data for processing into trajectories. Those that did were tests 5, 6, 13, 15, 18, 19, 22, 23, 24, and 25. Figure 4.21 through Figure 4.30 show the X-Z plane trajectories reduced from the Schlieren video data. Time labels are given in seconds for each case. The trajectory calculations were terminated upon the fragmentation of the store.

Table 4.13: Flow Conditions for Sphere Drop Tests

Test	$P_t$ (psia)	$U_\infty$ (ft/s)	$Re_\infty$ (ft <sup>-1</sup> )	Trajectory Data	Pressure Data
1-2	Tunnel start blew store downstream				
3	3.53	1799	$8.13 \times 10^5$		X
4	DAQ Error				
5	3.73	1799	$8.59 \times 10^5$	X	X
6	3.68	1799	$8.48 \times 10^5$	X	X
7	7.94	1804	$1.81 \times 10^6$		X
8	Insufficient air supply				
9	6.83	1804	$1.56 \times 10^6$		X
10	Captive sphere to test low $p_t$ setup				X
11	2.83	1823	$6.28 \times 10^5$		X
12	Valve pressure too low for flow				
13	1.45	1808	$3.29 \times 10^5$	X	X
14	Timing error				X
15	1.12	1809	$2.53 \times 10^5$	X	X
16	1.17	1806	$2.67 \times 10^5$		X
17	0.97	1806	$2.21 \times 10^5$		X
18	1.05	1803	$2.41 \times 10^5$	X	X
19	0.93	1802	$2.13 \times 10^5$	X	X
20	1.30	1808	$2.95 \times 10^5$		X
21	0.90	1804	$2.06 \times 10^5$		X
22	1.00	1806	$2.29 \times 10^5$	X	X
23	0.75	1798	$1.72 \times 10^5$	X	X
24	1.22	1809	$2.77 \times 10^5$	X	X
25	1.21	1809	$2.75 \times 10^5$	X	X

Usually this coincided with a collision between the trailing edge of the cavity and the store, though one, test 15 does not. The fragmentation observed in this test may be due to high aerodynamic loading on an imperfection in the store or due to a collision with the side wall of the cavity.

All of the trajectories demonstrate an initial forward,  $-X$ , tendency upon the release of the store. This phenomenon is especially present in test 5 and test 6, Figure 4.21 and Figure 4.22. Here, the store experiences a significant  $-X$  trajectory before convecting towards the back wall of the cavity ( $+X$ ). This phenomenon was also documented in the experimental test results of Flora [1]. These cases also exhibit a periodic vertical component of the trajectory consistent with the store “skipping” across the shear layer as it convects longitudinally. Due to the large forward translation and, in test 6, some interference from the store release mechanism while convecting towards the back wall, tests 5 and 6 take considerably longer before colliding with the back wall of the cavity when compared to the 1 psia stagnation pressure tests.

Each of the 1 psia stagnation pressure tests displays some initial  $-X$  trajectory component, with tests 15 and 23, Figure 4.24 and Figure 4.28, displaying the smallest forward component. Test 13 and test 25, Figure 4.23 and Figure 4.30, display the largest  $-X$  component. All of the 1 psia tests initially fall into and, on some occasions through, the shear layer ( $+Z$ ) before the vertical velocity reverses and results in a  $-Z$  translation, similar to that discussed in Section 2.3. This effect varies from an extreme climb back into the cavity as shown in test 25 (Figure 4.30) to a nearly imperceptible rise that has no real impact on the trajectory, as shown in test 24 (Figure 4.29). As the pitch of a sphere does not affect its lift or drag characteristics, it is likely that this rise is caused by compression lift acting on the lower surface of the sphere in the wake of the shock wave that forms as it exits the shear layer into supersonic flow. Figure 4.31 shows this bow shock forming on the lower half of the sphere as it protrudes into the freestream while the upper half is still contained in the shear layer, experiencing a lower pressure.

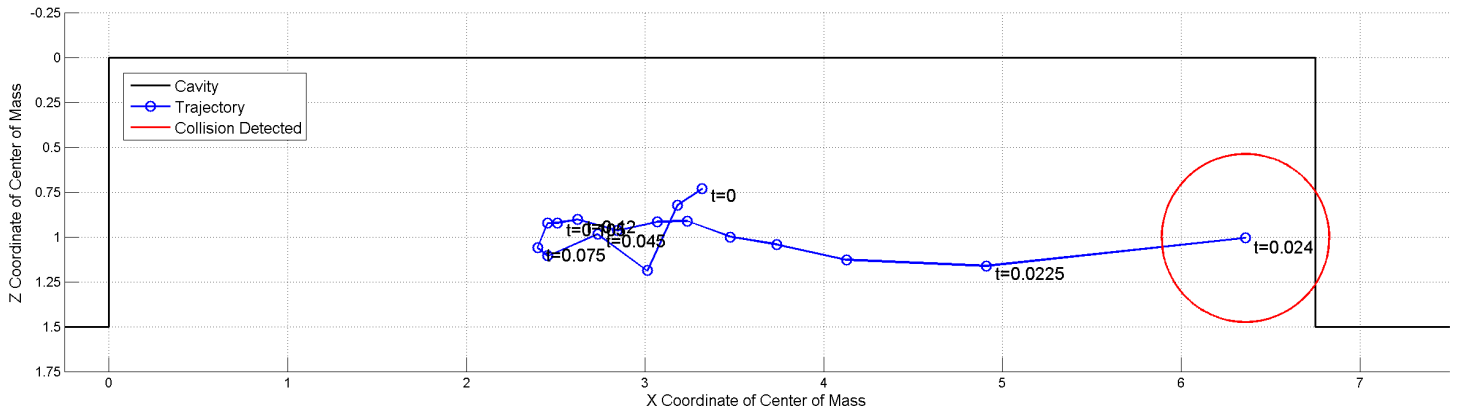


Figure 4.21: X-Z Plane Trajectory for Test 5 ( $P_t = 3.73$ )

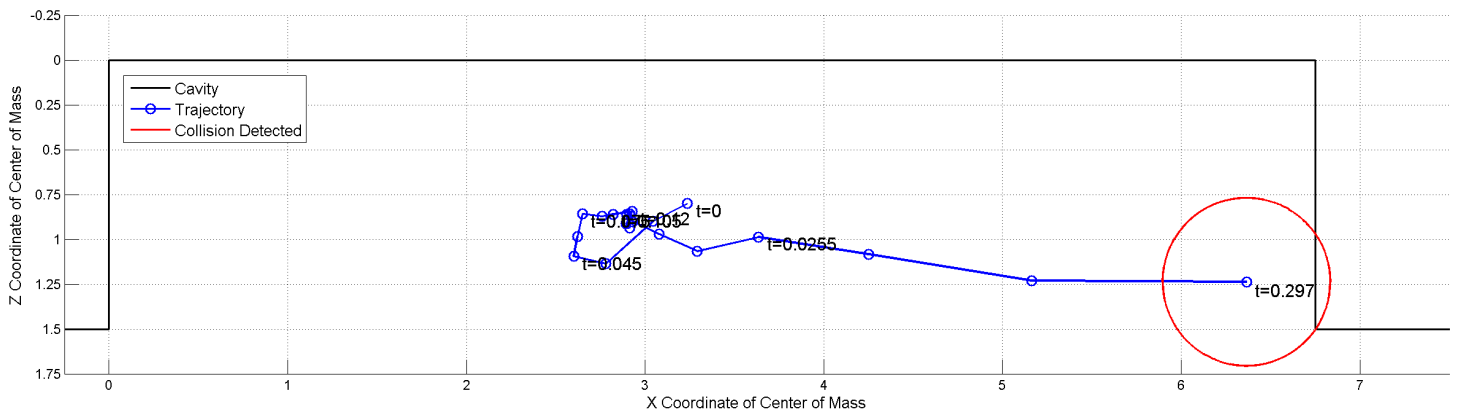


Figure 4.22: X-Z Plane Trajectory for Test 6 ( $P_t = 3.68$ )

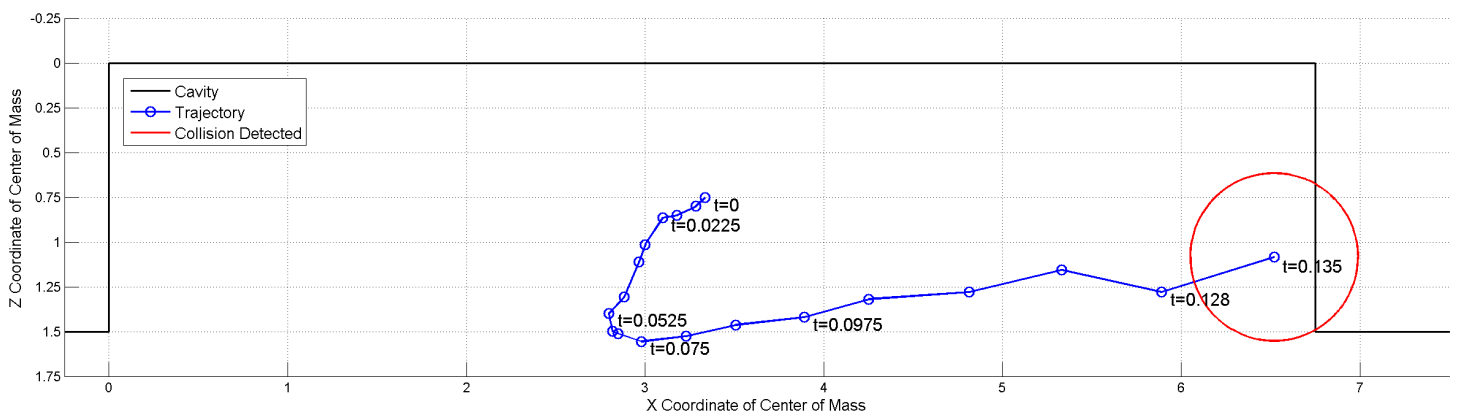


Figure 4.23: X-Z Plane Trajectory for Test 13 ( $P_t = 1.45$ )

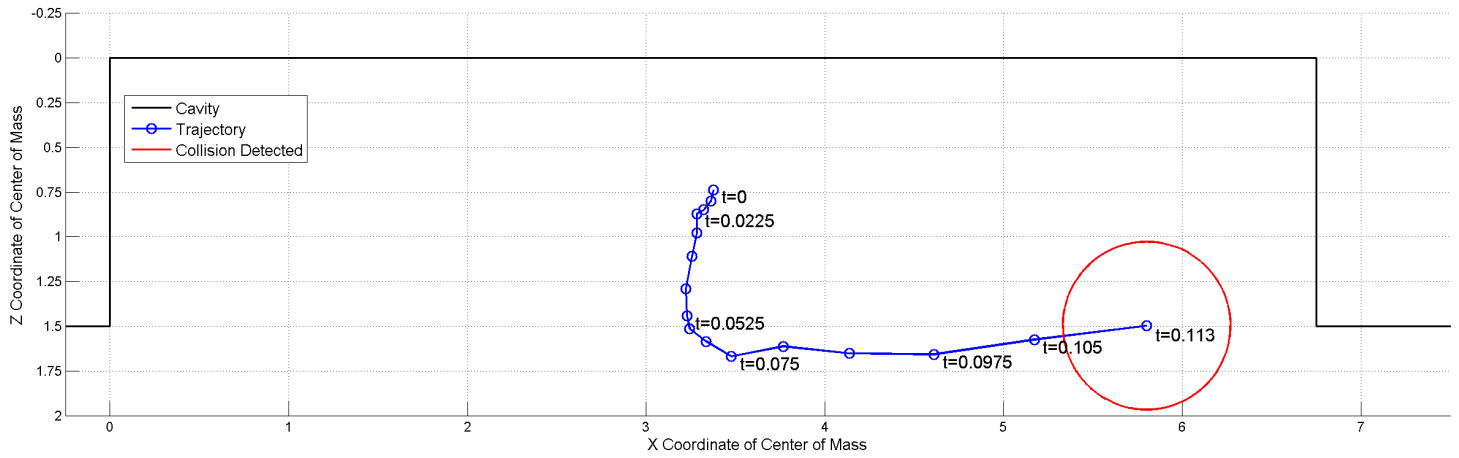


Figure 4.24: X-Z Plane Trajectory for Test 15 ( $P_t = 1.12$ )

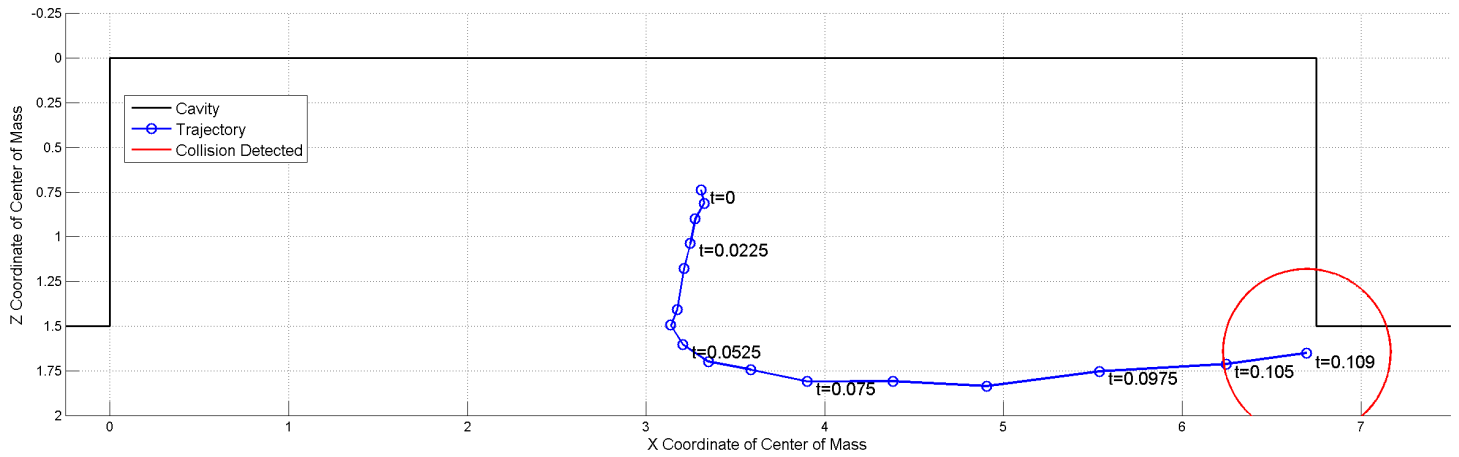


Figure 4.25: X-Z Plane Trajectory for Test 18 ( $P_t = 1.05$ )

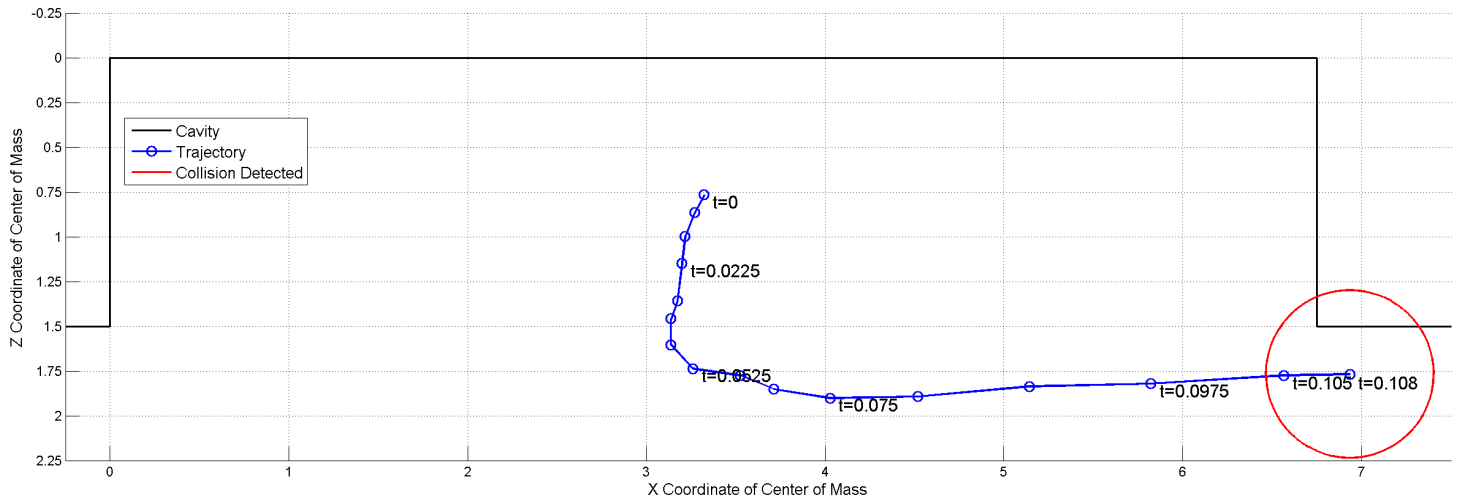


Figure 4.26: X-Z Plane Trajectory for Test 19 ( $P_t = 0.93$ )

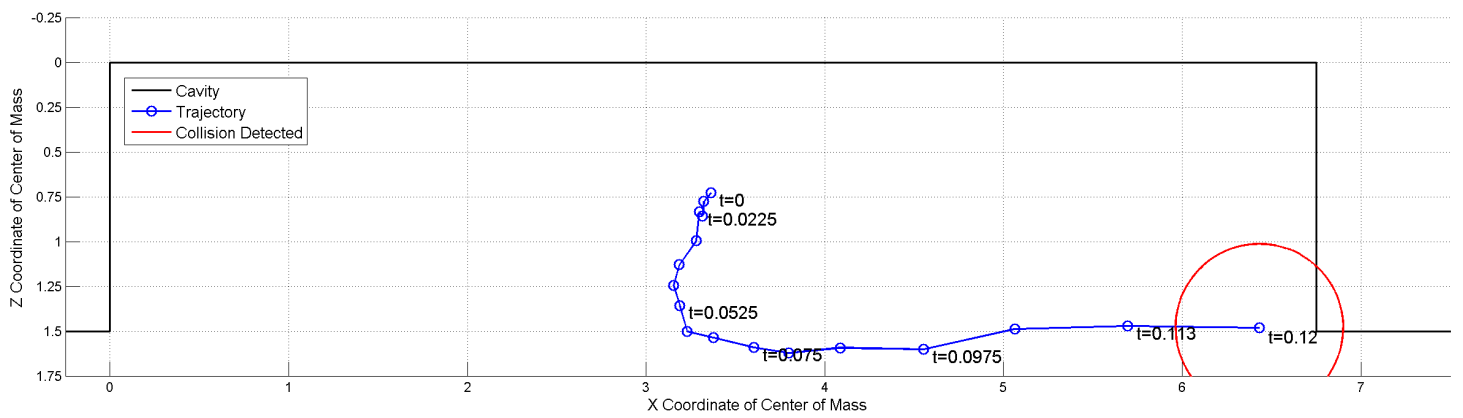


Figure 4.27: X-Z Plane Trajectory for Test 22 ( $P_t = 1.00$ )

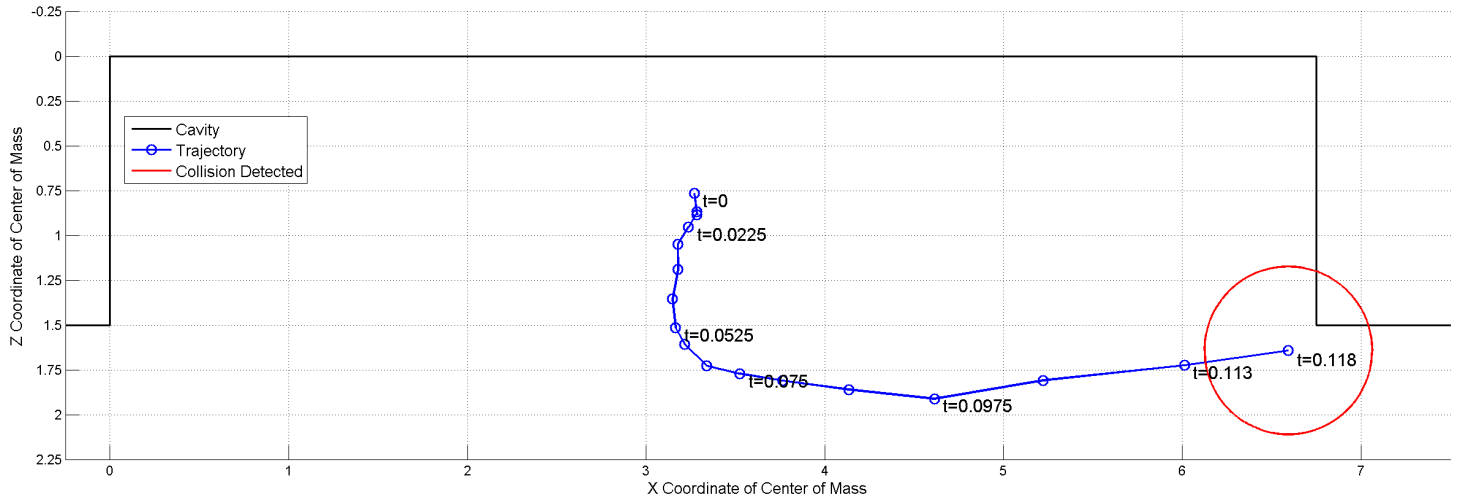


Figure 4.28: X-Z Plane Trajectory for Test 23 ( $P_t = 0.75$ )

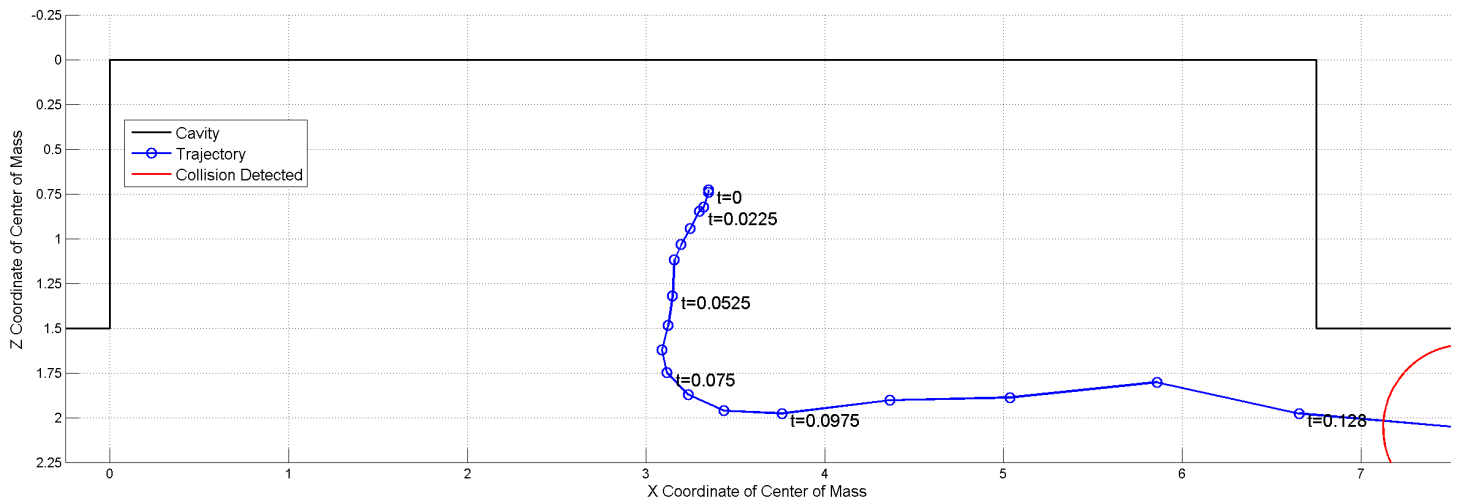


Figure 4.29: X-Z Plane Trajectory for Test 24 ( $P_t = 1.22$ )



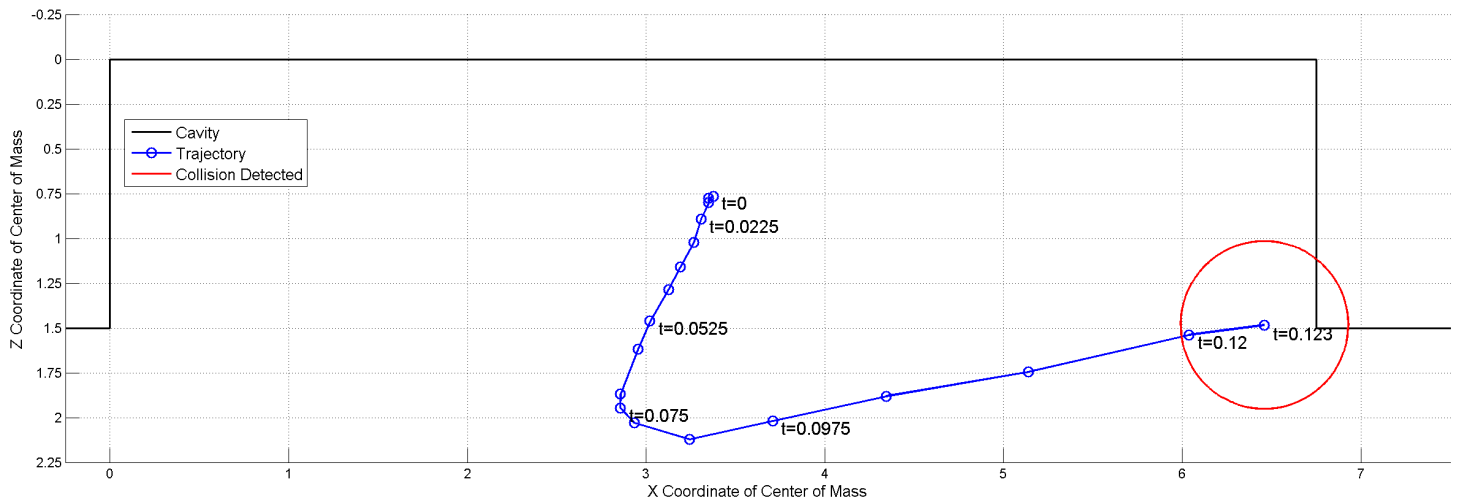


Figure 4.30: X-Z Plane Trajectory for Test 25 ( $P_t = 1.21$ )

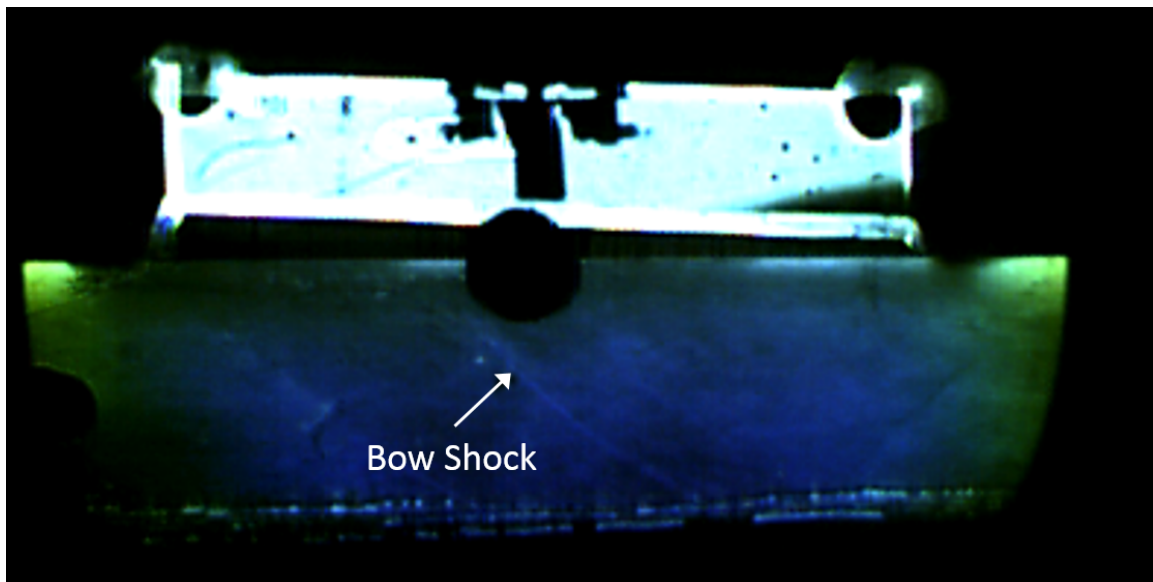


Figure 4.31: Bow shock on the lower half of a sphere

### 4.3.2 Computational.

Computational results were obtained for conditions corresponding to 3.5, 2.0, and 1.0 psia stagnation pressures at Mach 2.22. The trajectories are shown in Figure 4.32 through Figure 4.34, with time labels given in seconds. Figure 4.32, the 3.5 psia case clearly displays the  $-X$  initial trajectory seen in the experimental results, though to a much lesser extent. Figure 4.33, corresponding to 2.0 psia stagnation pressure also displays this trait, though its magnitude is nearly negligible. Figure 4.34, the 1.0 psia case, does not display an initial trajectory in the  $-X$  direction. While all 3 trajectories contact the back wall of the cavity, there is a clear downward trend in the location of contact as the pressure decreases. Figure 4.35 shows the time histories of the z-component of the trajectory for all three computational runs, with the traces representing the center of mass of the sphere. Figure 4.35 also shows that the 1.0 psia case is the only trajectory whose center of mass exited the cavity. All three computational trajectories also display the  $-Z$  translation that the experimental runs displayed, with higher pressure corresponding to a larger translation.

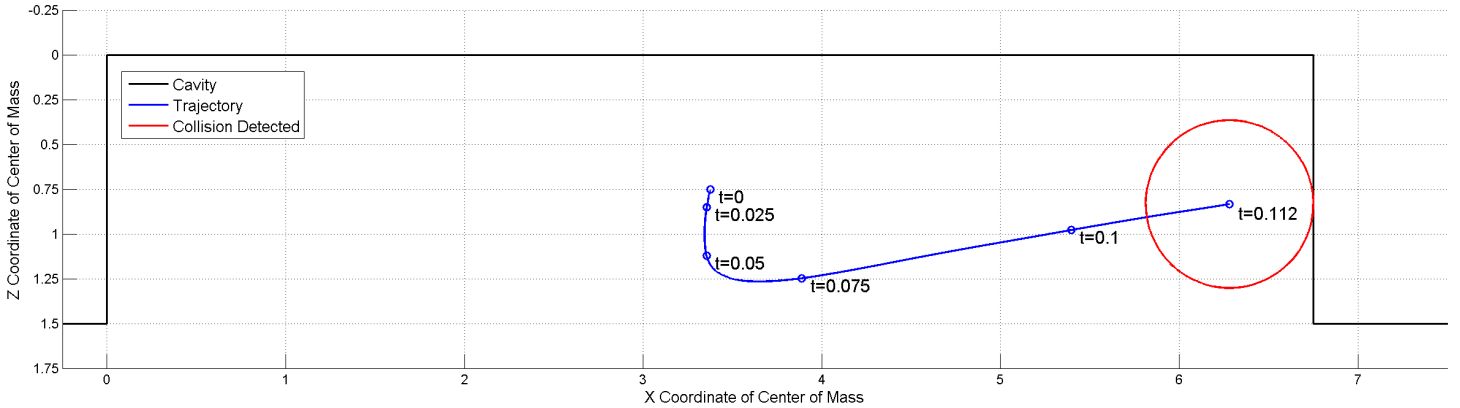


Figure 4.32: Computational X-Z Plane Trajectory at  $P_t = 3.5$

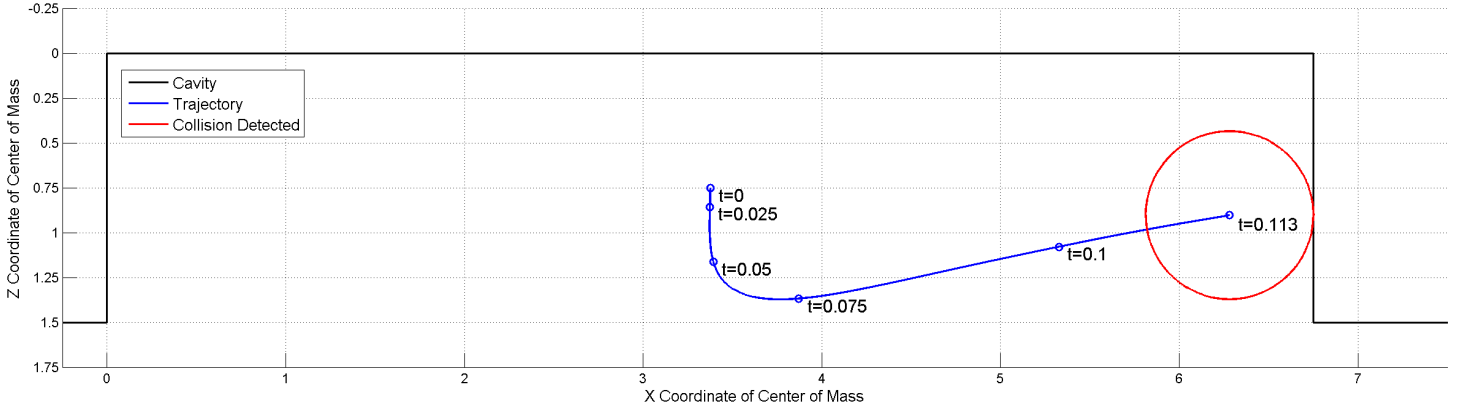


Figure 4.33: Computational X-Z Plane Trajectory at  $P_t = 2.0$

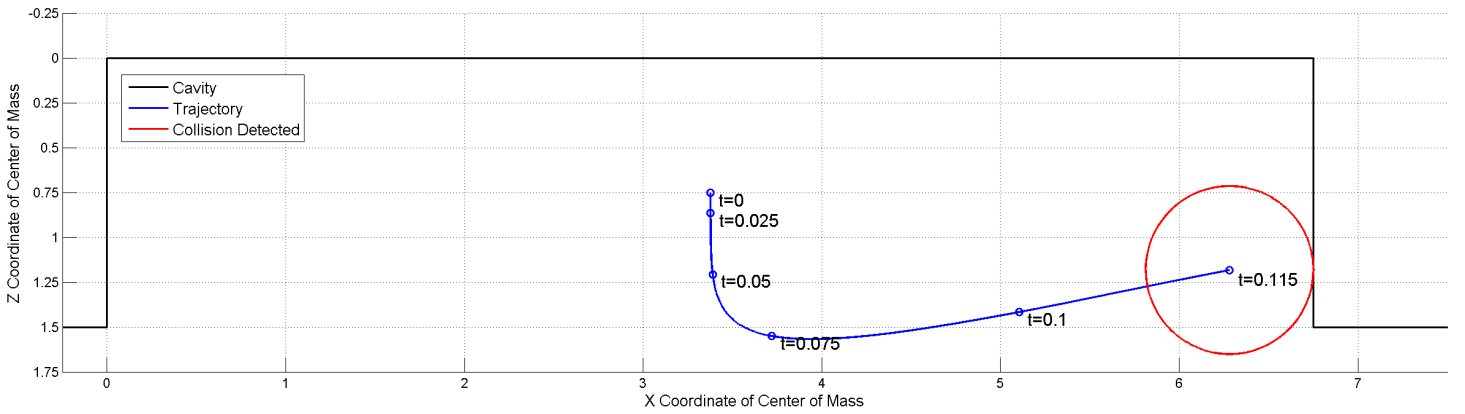


Figure 4.34: Computational X-Z Plane Trajectory at  $P_t = 1.0$

Figure 4.36 through Figure 4.38 show the residual traces for each of the grids. For each test, the *Plate* and *Bay* grid residuals quickly stabilize in the  $10^{-3}$  and  $10^{-4}$  range respectively. This is consistent with the residual traces of Flora [1]. The *Yin* and *Yang* grids initially stabilize in the  $10^{-4.5}$  to  $10^{-5}$  range, but as the simulation progresses and the sphere interacts with the cavity shear layer, around the 10,000 iteration mark, or 0.05 seconds, the residuals rise into the  $10^{-4}$  to  $10^{-4.5}$  range. This phenomenon was also seen in the work of Flora [1]. However, unlike Flora, the rise persists for the remainder of the

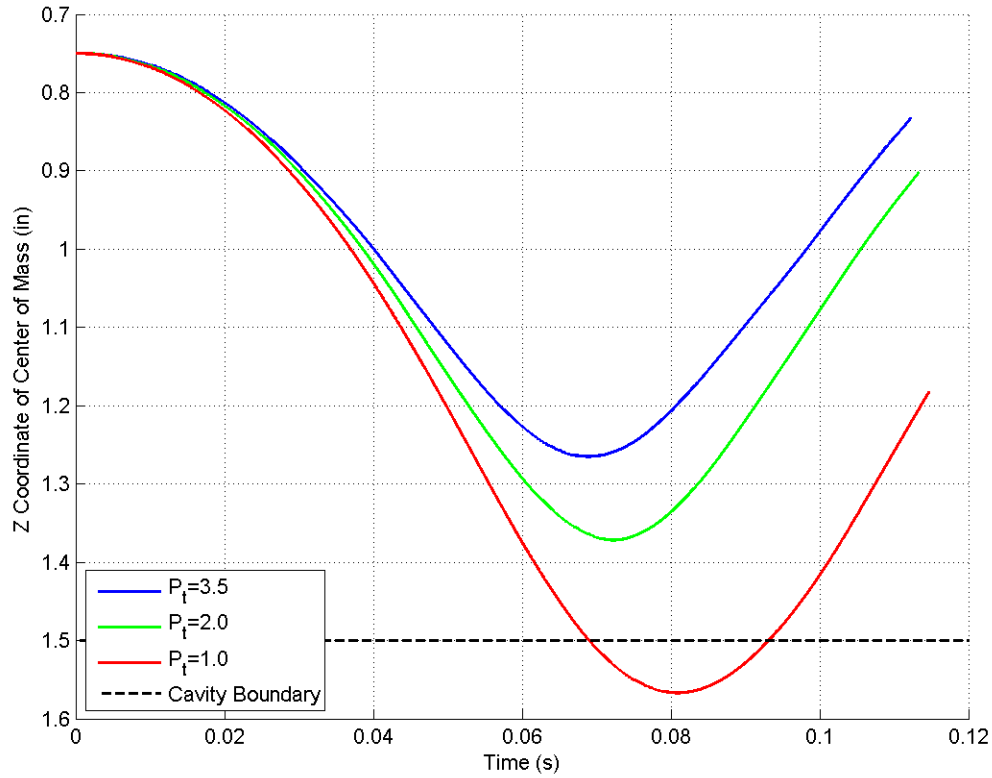


Figure 4.35: Computational Z-Trajectory vs. time

simulation. This is likely due to the lower speed resulting in a wider shear layer within the cavity, leading to a longer interaction between the sphere grids and the shear layer. In Figure 4.36 and especially in Figure 4.38 a sharp drop in the residuals for the *Yin* and *Yang* grids after approximately 25,000 iterations. This drop corresponds with these grids exiting the influence of the *Plate* and *Bay* grids through the back wall of the cavity. While OVERFLOW does have a collision modeling system, it was not enabled for these simulations, as the period of interest is from the initial “release” of the sphere until its first contact with another body.

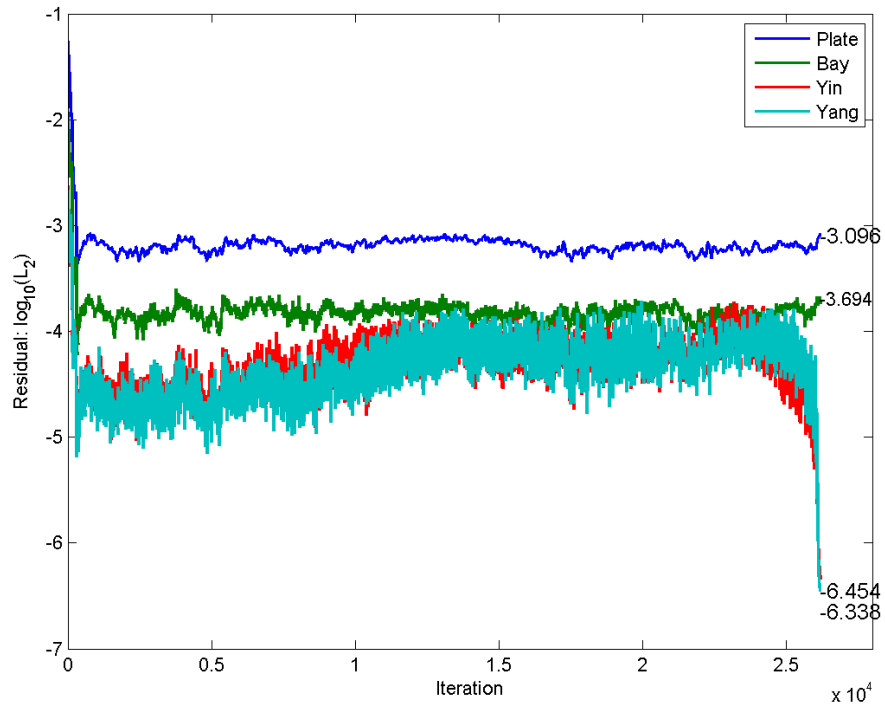


Figure 4.36: Residuals of  $P_t = 3.5$  Computational Run

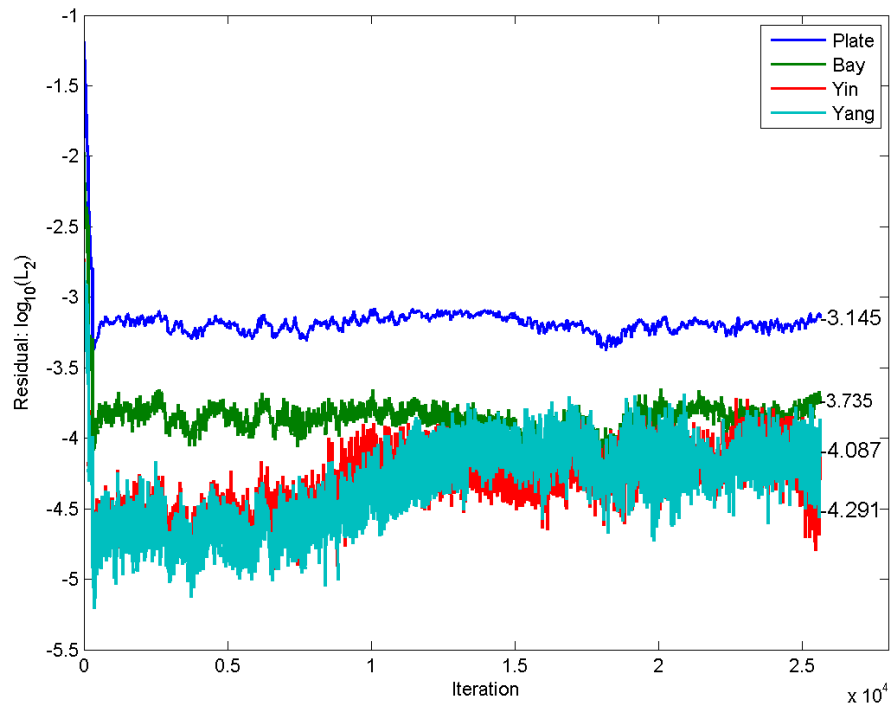


Figure 4.37: Residuals of  $P_t = 2.0$  Computational Run

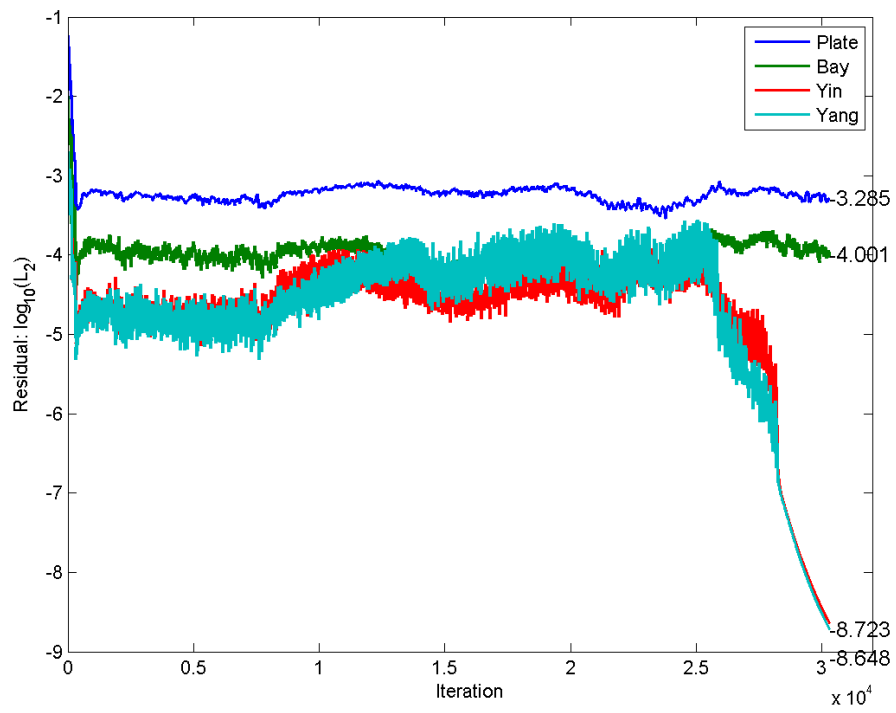


Figure 4.38: Residuals of  $P_t = 1.0$  Computational Run

### 4.3.3 Trajectory Comparison.

Figure 4.39 shows the comparison of the experimental and computational trajectories for 3.5 psia stagnation pressure. While the amount of initial +Z translation for the computational trajectory matches the experimental results, the magnitude of initial  $-X$  translation does not match and the  $-Z$  translation in the second half of the trajectory is larger than that seen in either experimental run. The computational trajectory also does not display any of the “skipping” phenomenon seen in the experimental results.

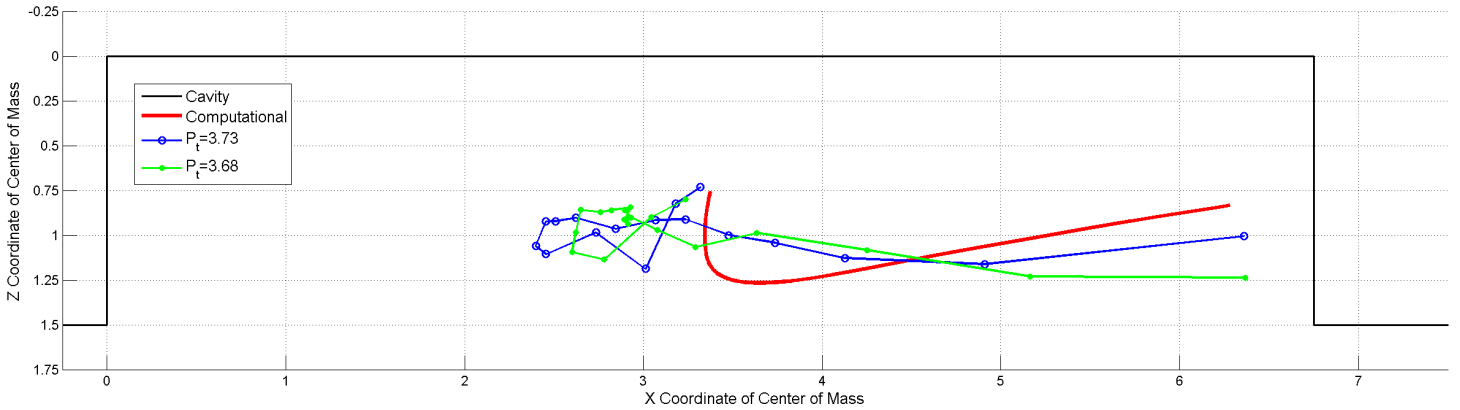


Figure 4.39: Comparison of Computational and Experimental Trajectories for  $P_t = 3.5$

Figure 4.40 compares the experimental and computational trajectories for 1.0 psia stagnation pressure. The overall agreement between computational and experimental results for this case is similar to that of the 3.5 psia case. While the computational trajectory does not display an initial  $-X$  motion like all of the experimental data, it does display a similar amount of  $-Z$  motion in the second half of the trajectory. The maximum +Z motion predicted computationally is lower than nearly all of the experimental results, yet still of a comparable magnitude to multiple tests, specifically tests 13, 15, and 22. It is interesting to note that all but one of the experimental trajectories end farther towards the freestream

than the computational case. By  $X = 6$ ,  $Z$ -values corresponding to the experiments vary from  $Z = 1.25$  to  $Z = 1.75$ , while the computational trajectory yields  $Z = 1.25$ .

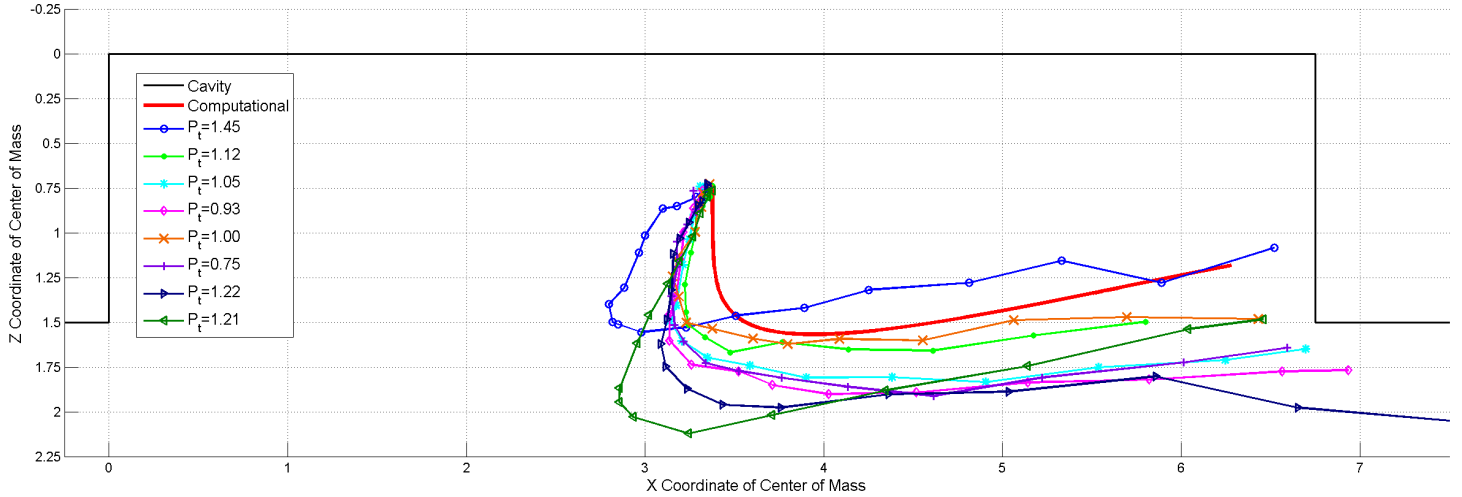


Figure 4.40: Comparison of Computational and Experimental Trajectories for  $P_t = 1.0$

#### 4.3.4 Heavy Mach Scaling.

Heavy Mach Scaling is achieved through the equations described in Section 2.2. The experimental results are scaled to standard day conditions at ten, twenty, and thirty thousand feet using a model scale factor of 0.05. Since the model density is fixed at the density of ice, approximately  $62 \text{ lb/ft}^3$ , the SVDB capabilities of scaling tunnel stagnation pressure, and hence dynamic pressure, are used to achieve the proper scaling. Table 4.14 shows the scaled quantities of each test and simulation to 10,000 ft standard day conditions. The resulting average quantities for the 3.5 psia stagnation pressure are a store weight of 171.6 lb, a dynamic pressure ratio of 0.033, and an average model density of  $85.9 \text{ lb/ft}^3$ . The average quantities for the 1.0 psia case are a store weight of 629.0 lb, a dynamic pressure ratio of 0.010, and a store density of  $314.9 \text{ lb/ft}^3$ .



Table 4.14: Sphere Heavy Mach Scaling.  $M=2.22$ ,  $h=10,000$  ft,  $1/20$  scale

Test	$P_t$	$q'_\infty/q_\infty$	Weight (lb)	Density ( $lb/ft^3$ )
5	3.73	0.034	169.3	84.8
6	3.68	0.033	174.0	87.1
$P_t = 3.5$	3.50	0.031	195.1	97.7
$P_t = 2.0$	2.00	0.018	341.5	171.0
13	1.45	0.013	448.6	224.6
15	1.12	0.010	607.2	304.0
18	1.05	0.009	631.7	316.3
19	0.93	0.008	722.1	361.5
22	1.00	0.009	656.9	328.9
23	0.75	0.007	889.2	445.2
24	1.22	0.011	538.6	269.7
25	1.21	0.011	537.7	269.2
$P_t = 1.0$	1.00	0.009	682.9	341.9

Table 4.15 shows the scaled quantities of each test scaled to 20,000 ft standard day conditions. The 3.5 psia tests result in an average store weight of 114.7 lb, a 0.050 average ratio of dynamic pressures, and an average store density of 57.4 lb/ft<sup>3</sup>. Testing at 1.0 psia results in averages of 420.3 lb for store weight, dynamic pressure ratio equal to 0.015, and a store density of 210.4 lb/ft<sup>3</sup>.

Scaled quantities at 30,000 ft standard day conditions are shown in Table 4.16. Tests at a stagnation pressure of 3.5 psia result in an average store weight of 74.1 lb, an average dynamic pressure ratio of 0.077, and an average store density of 37.1 lb/ft<sup>3</sup>. The average quantities resulting from a stagnation pressure of 1.0 psia are a store weight of 271.6 lb, a dynamic pressure ratio of 0.023, and a store density of 136.0 lb/ft<sup>3</sup>.

Table 4.15: Sphere Heavy Mach Scaling.  $M=2.22$ ,  $h=20,000$  ft,  $1/20$  scale

Test	$P_t$	$q'_\infty/q_\infty$	Weight (lb)	Density ( $lb/ft^3$ )
5	3.73	0.050	113.13	56.6
6	3.68	0.050	116.3	58.2
$P_t = 3.5$	3.50	0.047	130.4	65.3
$P_t = 2.0$	2.00	0.027	228.2	114.2
13	1.45	0.019	299.8	150.1
15	1.12	0.015	405.7	203.1
18	1.05	0.014	422.2	211.4
19	0.93	0.012	482.5	241.6
22	1.00	0.013	438.9	219.8
23	0.75	0.010	594.2	297.5
24	1.22	0.016	359.9	180.2
25	1.21	0.016	359.3	179.9
$P_t = 1.0$	1.00	0.013	456.3	228.5

As the scaled altitude increases, the scaled air density decreases, more closely approximating the wind tunnel conditions. This causes the scaling to have less effect on the store weight and density, as seen by comparing the store weight and densities across Table 4.14 through Table 4.16. However, at 10,000 ft, by utilizing the vacuum system to lower the stagnation pressure to 1.0 psia, the SVDB is capable of mimicking real world store separation conditions. This approach of aggressively scaling dynamic pressure and achieving a heavy Mach-scaled environment at a small scale ( $1/20$ ) is atypical. More commonly, model densities are increased through the addition of heavy materials such as lead shot and are performed at larger scales.

Table 4.16: Sphere Heavy Mach Scaling.  $M=2.22$ ,  $h=30,000$  ft,  $1/20$  scale

Test	$P_t$	$q'_\infty/q_\infty$	Weight (lb)	Density ( $lb/ft^3$ )
5	3.73	0.078	73.1	36.6
6	3.68	0.077	75.1	37.6
$P_t = 3.5$	3.50	0.072	84.3	42.2
$P_t = 2.0$	2.00	0.041	147.5	73.8
13	1.45	0.030	193.7	97.0
15	1.12	0.023	262.2	131.3
18	1.05	0.022	272.8	136.6
19	0.93	0.019	311.8	156.1
22	1.00	0.021	283.7	142.0
23	0.75	0.015	384.0	192.3
24	1.22	0.025	232.6	116.5
25	1.21	0.025	232.2	116.3
$P_t = 1.0$	1.00	0.021	294.9	147.6

## **V. Conclusions**

### **5.1 Nozzle and Cavity Characterization**

Understanding and controlling the conditions under which a test is performed is a crucial first step in building a body of research. The fabrication of three nozzles at nominal Mach numbers of 2.3, 1.9, and 1.5 presents numerous future opportunities to conduct high speed wind tunnel testing at AFIT. While well documented contours from AFRL's TGF were used in building these nozzles, the small scale environment and new upstream contour used in order to adapt the nozzles to the AFIT SVDB tunnel introduced several unknown variables. With the replacement of the SVDB tunnel faceplate and flow straighteners, these variables were compounded. Through quantitative and qualitative techniques, these new nozzles were verified to conform to analytical predictions, with average Mach numbers of 2.22, 1.84, and 1.43 being determined through the use of static pressure ratios and verified through the use of Schlieren photography. Additionally, qualitative data was obtained from Schlieren photography indicating the boundary layer height at the nozzle exit to be approximately 0.1 inches for all nozzles. This analysis aligns with the values predicted through the use of turbulent boundary layer theory.

As verification of testing techniques and procedures, the existing Mach 3.0 nozzle was tested in a similar fashion. This nozzle was found to have a freestream Mach of 2.96. Previous research yielded a similar result. This grants further confidence to the results obtained for the Mach 2.3, 1.9, and 1.5 nozzles.

The Mach 1.5 nozzle was determined to be of questionable use at low stagnation pressures without modifications to the SVDB diffuser section due to a normal shock forming in the test section. This shock is delayed through the use of higher stagnation pressures. However, the increased mass flow associated with these higher pressures reduces the amount of time the tunnel can be used before back pressure in the system causes the

tunnel to unstart. Stagnation pressures up to 15.2 psia all display this normal shock at various locations in the test section, but at 10 psia or higher, the shock is far enough downstream in the test section to allow for pressure data to be collected.

After verifying and characterizing the flow through the test section with these new nozzles, the acoustic cavity environment was characterized and compared to the predicted Rossiter modes. As with the nozzle characterization, the Mach 3.0 nozzle was initially used to verify the data collection techniques. Results obtained for this nozzle matched data from previous research and correlated well with predicted resonant frequencies.

Subsequently, the three new nozzles were used in collecting data about the acoustic cavity environment. The Mach 2.3 and Mach 1.9 nozzles produced spectra that correlated extremely well with the analytically predicted Rossiter modes, showing clear resonant peaks for the first seven modes. With the exception of the first mode, less than 10% difference between the observed and predicted modes was recorded. The first mode showed a clear peak, but slightly more error.

The cavity flow for the Mach 1.5 nozzle was compromised by the size of the cavity, even at stagnation pressures up to 15 psia. The angle of the oblique shock off the leading edge of the cavity is sufficiently steep that the shock is reflected off the lower wall of the test section and impinges on the back wall of the cavity. Even with this large increase in noise, several resonant peaks were detected, and the frequencies of these peaks matched the predicted Rossiter modes.

With the completion of the nozzle characterization and the strong correlation between the predicted and observed spectra of the cavity environment, the first goal of this research is successfully completed. The SVDB tunnel now has the capability to conduct tests at a range of Mach numbers with confidence in the quality of the flow and its ability to reproduce complex aeroacoustic problems consistently.

## 5.2 Store Separation

The capability to successfully release a store from a cavity, such as an internal weapons bay, at supersonic speeds has clear tactical and operational advantages. However, the unsteady and highly forceful nature of shallow cavity flows makes this problem especially difficult and dangerous. To mitigate this danger, CFD simulations and experimental freedrop testing are extensively used. While CFD simulations can be scaled to many sizes relatively easily, they are computationally intensive because of the necessity of a time-accurate simulation and a 6DOF motion solver. Furthermore, the turbulence modeling may introduce some inaccuracies. Experimental freedrop testing can provide useful information about full-scale stores, but the scaling methods needed to balance the inertial and aerodynamic forces incorporate unavoidable compromises. Typical heavy Mach scaling overcomes the imbalance of aerodynamic and inertial forces by increasing the model density with lead shot or similarly heavy and destructive materials. This increases the cost and risk associated with a freedrop test in a wind tunnel environment.

The tests performed in this research were performed with the Mach 2.3 nozzle and sought to create a heavy Mach scaling environment not by increasing model density, but by decreasing freestream dynamic pressure. This was accomplished by reducing the stagnation pressure of the SVDB tunnel. Through the use of a vacuum pump, the stagnation pressure of the tunnel can be reduced to approximately 1.0 psia while maintaining supersonic flow of the intended Mach number. These flow conditions were only previously attainable in a computational setting. Drop testing of an inertially simple store, a sphere made of ice, yielded Schlieren video data that was used to create a two-dimensional trajectory of the store as it was dropped from the cavity. Stagnation pressures of approximately 3.5 psia and 1.0 psia were tested with multiple freedrops. The trajectories produced by these drops was compared to computational trajectories produced using the

OVERFLOW solver. The computational flow parameters were altered to mimic those seen in the experimental testing.

At 3.5 psia stagnation pressure, the experimental and computational trajectories differed noticeably. Experimentally, a large translation towards the front wall after initial release was observed, as well as a periodic vertical translation believed to indicate the “skipping” of the store off the shear layer separating the cavity from the freestream. The forward translation predicted in the computational trajectory was significantly smaller, and no “skipping” phenomenon was predicted. Despite these differences, the relative magnitude of total vertical translation was similar between the computational and experimental trajectories.

At 1.0 psia stagnation pressure, the experimental and computational trajectories matched fairly closely. While the computational trajectory did not display an initial forward motion as seen in the experimental trajectories, the initial downward translation and subsequent upward translation correlated closely with the experimental trajectories.

The differences seen in the correlation between experimental and computational data for the different stagnation pressures seem to suggest that when inertial forces play a more prominent role, as in the 1.0 psia case, the computational and experimental data correlate more closely. Another factor leading to differences between the experimental and computational results may also be the unsteadiness inherent to cavity flow and the timing of the release.

Heavy Mach scaling was applied to the experimental and computational results, scaling the data to standard day conditions at multiple altitudes. By reducing the stagnation pressure to such low levels, scaled store weights typical of modern-day weapons were achieved. This will allow future research to utilize the low stagnation pressure setup to obtain operationally relevant results.

With these results, this research has satisfied both its secondary goal of directly comparing low pressure experimental and computational results and its tertiary goal of generating two-dimensional trajectory plots of the experimental data for further direct comparison of trajectory data between the experimental and computational results.

### 5.3 Future Opportunities

The numerous hardware upgrades performed on the AFIT SVDB tunnel provide a launching point for a significant amount of store separation research. The following discussion provides a few areas where research could be conducted.

- **Nozzle Characterization:** While the freestream turbulence level and boundary layer thickness were predicted analytically in this research, and the boundary layer thickness qualitatively verified, a thorough characterization using PIV or hot-wire techniques would improve the experimental control of future projects
- **Flow Control:** The cavity used in this research implemented no flow control devices in an attempt to reduce peak or broadband cavity noise levels. Significant research has already been conducted on flow control, but the AFIT SVDB tunnel now has the capability to test more advanced flow control methods at multiple Mach numbers and in a well understood cavity environment.
- **Computational Tuning:** The grids used in this research were obtained from previous research. A full time-step study, grid-refinement study, and turbulence model optimization with the goal of matching the spectra produced by the experimental cavity would increase AFIT's store separation capabilities.
- **Store Separation:** While heavy Mach scaling dampens pitch response, it would still be beneficial to research the trajectories produced by a more complicated store geometry than a sphere. Some research has been done utilizing a Mk. 82 geometry,



but not at the low experimental pressures that can now be obtained using the SVDB tunnel. Additionally, the release mechanism could be altered to provide an ejection force similar to that seen in operational store separations.

## Appendix A: Nozzle Design Code

```
1 % Nozzle design code, uses contours adapted from TGF
   contours
2
3 %% Constants
4 close all; clear all; clc
5 load X15_data.txt
6 load X19_data.txt
7 load X23_data.txt
8
9 ymax=1.2;
10 display=1; %0 for write, 1 for graphs, otherwise nothing
11 height=2.5;
12 curve=0; %1 for fit
13
14 %% Compute
15 for i=1:3
16     switch i
17         case 1
18             A=X15_data;
19         case 2
20             A=X19_data;
21         case 3
22             A=X23_data;
23         otherwise
24
25     end
26
27     ymin=min(A(:,2));
28     yint=(ymax+ymin)/2;
29     amp=(ymax-ymin)/2;
30
31     ind=find(A(:,2)==min(A(:,2)),1,'first');
32
33     per=2*(14/height-A(ind,1));
34
35     omega=per/2/pi;
36
37     f=amp*cos(omega*A(:,1))+yint;
38
39     ind2=find(f==min(f),1,'first');
40
41     fcon=cat(1,f(1:ind2),A(ind:end,2));
42
```

```

43     error1=abs(f(ind2-1)-A(ind-1,2));
44     error2=abs(f(ind2-2)-A(ind-2,2));
45
46     endind=find(fcon>0,1,'last');
47     ind3(i)=endind;
48
49     switch i
50     case 1
51         M15.amp=amp;
52         M15.y=yint;
53         M15.w=omega;
54         M15.e1=error1;
55         M15.e2=error2;
56         M15.fcon=fcon;
57     case 2
58         M19.amp=amp;
59         M19.y=yint;
60         M19.w=omega;
61         M19.e1=error1;
62         M19.e2=error2;
63         M19.fcon=fcon;
64     case 3
65         M23.amp=amp;
66         M23.y=yint;
67         M23.w=omega;
68         M23.e1=error1;
69         M23.e2=error2;
70         M23.fcon=fcon;
71     otherwise
72
73     end
74 end
75
76 for i=1:3
77     switch i
78     case 1
79         fcon=M15.fcon;
80     case 2
81         fcon=M19.fcon;
82     case 3
83         fcon=M23.fcon;
84     otherwise
85
86     end
87

```

```

88         fcon=cat(1,fcon(1:end),fcon(end)*ones(max(ind3)-
           length(fcon),1));
89
90     switch i
91     case 1
92         M15.fcon=fcon;
93     case 2
94         M19.fcon=fcon;
95     case 3
96         M23.fcon=fcon;
97     otherwise
98
99     end
100 end
101
102 dx=X15_data(2,1)-X15_data(1,1);
103 x=0:dx:dx*(max(ind3)-1);
104
105 %% Display
106 for i=1:3
107     switch i
108     case 1
109         A=M15;
110         filename='M15_contour.txt';
111         str='Mach=1.5 Nozzle Contour';
112     case 2
113         A=M19;
114         filename='M19_contour.txt';
115         str='Mach=1.9 Nozzle Contour';
116     case 3
117         A=M23;
118         filename='M23_contour.txt';
119         str='Mach=2.3 Nozzle Contour';
120     otherwise
121
122     end
123     if display==1
124         figure
125         plot(height*x,height*A.fcon)
126         grid on
127         xlabel('Length (in)')
128         ylabel('Dimension from Centerline (in)')
129         title(str);
130         axis([0 height*x(end) 0 height*ymax+0.1]);
131
132

```

```

133     elseif display==0
134         fileID=fopen(filename,'w');
135         for j=1:length(A.fcon)
136             fprintf(fileID,'%4.8f %4.8f %4.8f\n',height*x(j)
137                 ,height*A.fcon(j),0);
138         end
139     end
140
141 %% Curve fit
142 x=height*x;
143 for i=1:3
144     switch i
145     case 1
146         A=M15;
147     case 2
148         A=M19;
149     case 3
150         A=M23;
151     end
152     A.fcon=A.fcon*height;
153     if curve==1
154         A.p6=polyfit(x',A.fcon,6);
155         A.p8=polyfit(x',A.fcon,8);
156         A.p10=polyfit(x',A.fcon,10);
157         A.p12=polyfit(x',A.fcon,12);
158         A.p14=polyfit(x',A.fcon,14);
159         A.p16=polyfit(x',A.fcon,16);
160
161         A.fit6=polyval(A.p6,x);
162         A.fit8=polyval(A.p8,x);
163         A.fit10=polyval(A.p10,x);
164         A.fit12=polyval(A.p12,x);
165         A.fit14=polyval(A.p14,x);
166         A.fit16=polyval(A.p16,x);
167
168         A.perr6=max((A.fcon'-A.fit6)./A.fcon');
169         A.perr8=max((A.fcon'-A.fit8)./A.fcon');
170         A.perr10=max((A.fcon'-A.fit10)./A.fcon');
171         A.perr12=max((A.fcon'-A.fit12)./A.fcon');
172         A.perr14=max((A.fcon'-A.fit14)./A.fcon');
173         A.perr16=max((A.fcon'-A.fit16)./A.fcon');
174     end
175     switch i
176     case 1
177         M15=A;

```

```
178         case 2
179             M19=A;
180         case 3
181             M23=A;
182     end
183 end
184
185 M15con=M15.fcon;
186 M19con=M19.fcon;
187 M23con=M23.fcon;
```

## Appendix B: Transducer Calibrations

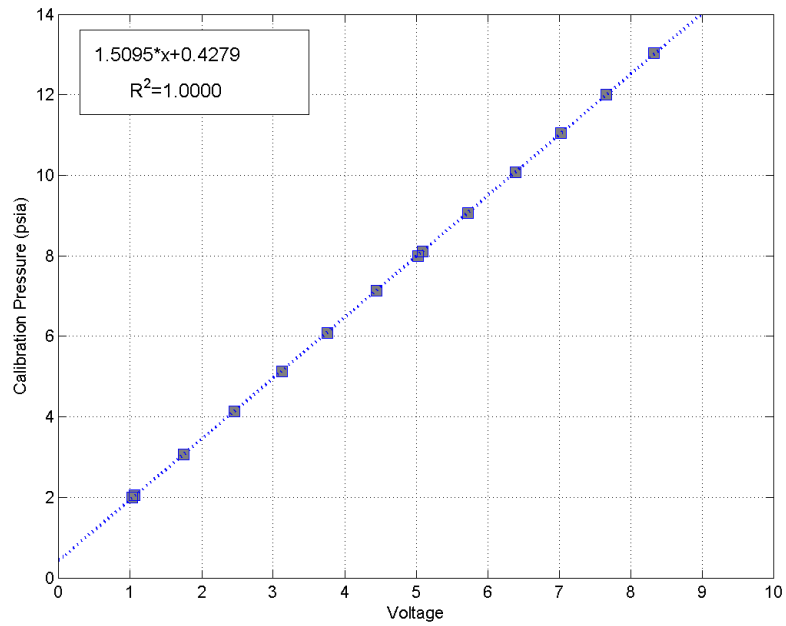


Figure B.1: 1-1: Cavity Front

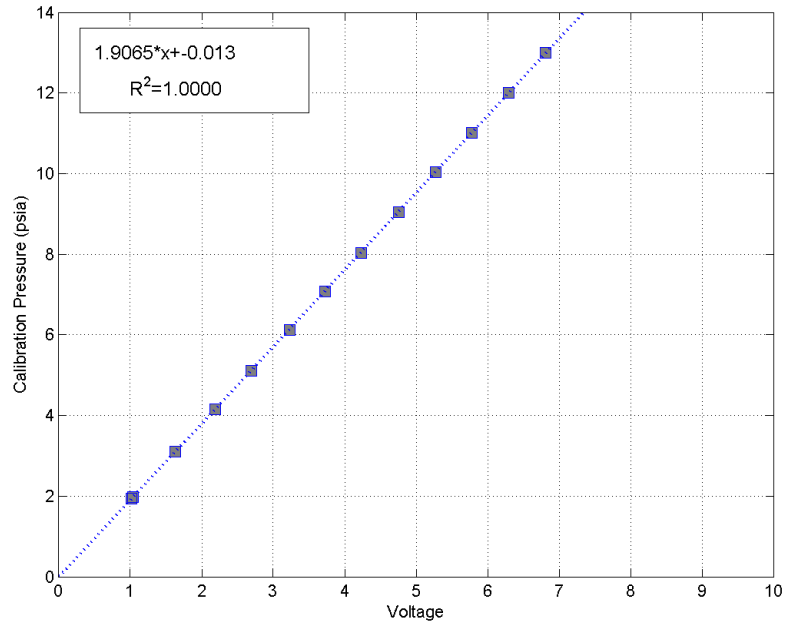


Figure B.2: 1-2: Low Pressure Diaphragm Setup

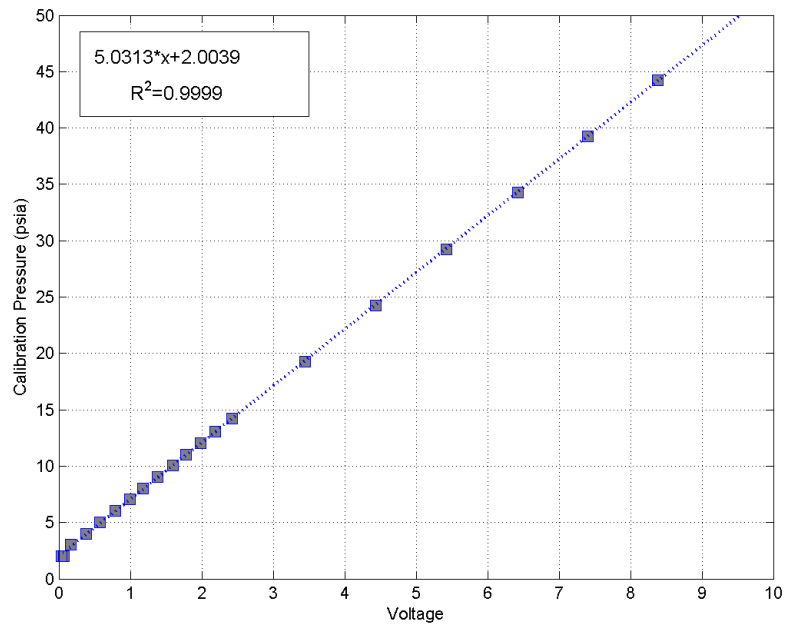


Figure B.3: 1-3: Stagnation Chamber

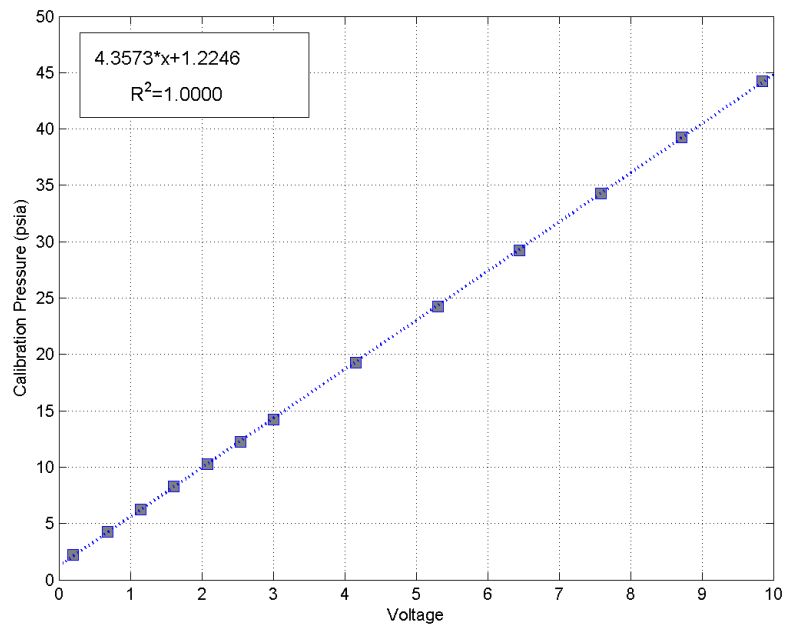


Figure B.4: 2-1: Vacuum Valve



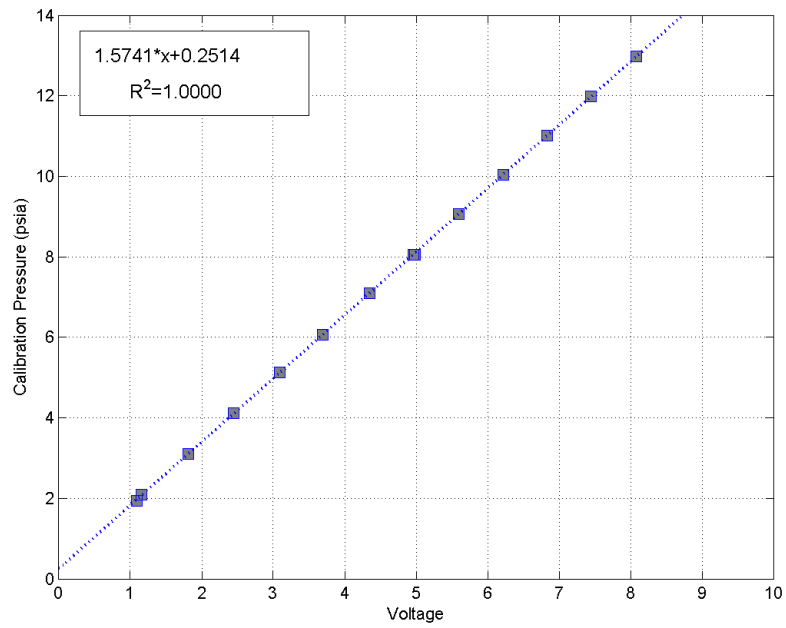


Figure B.5: 2-2: Cavity Back Wall

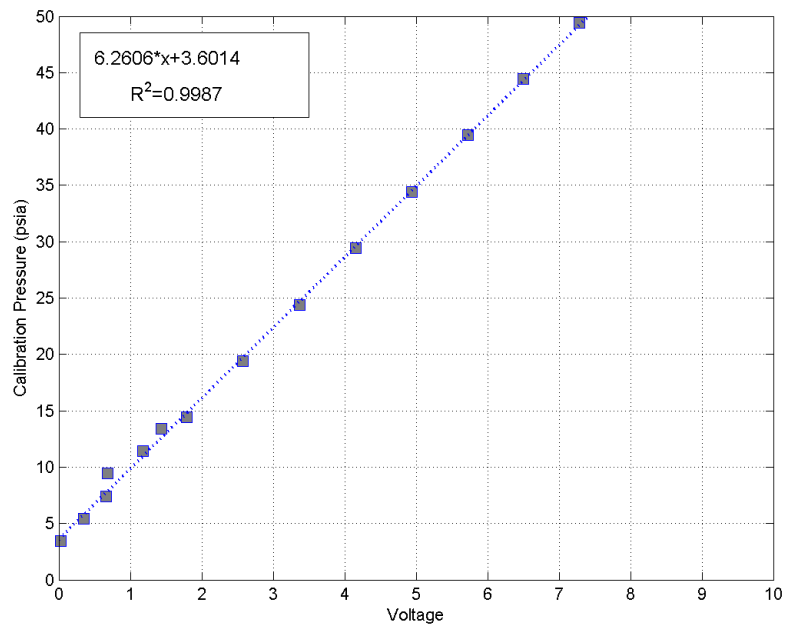


Figure B.6: 2-3: High Pressure Diaphragm Setup

## Appendix C: Flow Conditions Code

```
1 % Function that calculates flow parameters based on file
   name structure ,
2 % uses EE units of psi , lb/ft^3 , ft/s , deg R
3
4 function [A]=Flow_Con( filepath ,A, tstart )
5
6 %% Constants
7 gamma=1.4;
8 R_air=1716;
9 C1=1.458e-6;
10 C2=110.4;
11
12 tmp=roundn(A.data(:,1),-1);
13 ind=find(tmp==tstart,1,'first');
14 A.data=A.data(ind:end,:);
15 %% Mach number and pressure ratio
16 tmp=strfind(filepath,'\');
17 filename=filepath(tmp(end)+1:end);
18
19 % logic that determines whether Mach number is assumed or
   calculated.
20 % Hinges on filename format using word 'straight' (e.g.
21 % Mach23_straight_4.lvm). Accepts 'M' or 'Mach' as first
   expression.
22
23 if isempty(strfind(filename,'straight'))==1 % if 'straight'
   not in filename
24     actual_Mach=[2.9579,2.2226,1.8352,1.4294];
25     design_Mach=[3,23,19,15];
26     if filename(1:4)=='Mach'
27         tmp=sscanf(filename,'%*4s%f_%*s_%*f.lvm');
28         ind=find(design_Mach==tmp,1,'first');
29     else
30         tmp=sscanf(filename,'%*1s%f_%*s_%*f.lvm');
31         ind=find(design_Mach==tmp,1,'first');
32     end
33     A.Mach_inf=actual_Mach(ind);
34     prat=(1+(gamma-1)*.5*A.Mach_inf^2)^(gamma/(gamma-1));
35     % calculate pressure ratio off of assumed Mach number
36
37 else %calculate Mach number using pressure ratio
38     for j=1:length(A.data)
39         V=(A.data(j,7)+0.0549)/1.9118;
```

```

40         p=1.9065*V-0.013;
41         A.prat(j)=A.data(j,3)./p;
42         A.Mach(j)=sqrt(2/(gamma-1)*(A.prat(j)^((gamma-1)/
            gamma)-1));
43     end
44     A.Mach_inf=mean(A.Mach);
45     A.Mach_std=std(A.Mach);
46     prat=mean(A.prat);
47 end
48
49 A.filename=filename;
50
51 %% Other Calcs
52 A.pt=mean(A.data(:,3));
53 A.pt_std=std(A.data(:,3));
54 A.p_inf=A.pt/prat;
55
56 Tt1=(mean(A.data(:,2))+273.15).*(9/5);
57 Trat=1+(gamma-1)*.5*A.Mach_inf^2;
58 A.T_inf=Tt1/Trat;
59
60 A.rhot=A.pt*144/(R_air*Tt1);
61 A.rho_inf = A.p_inf*144/(R_air*A.T_inf);
62
63 mut_SI=C1*(Tt1*5/9)^1.5/(Tt1*5/9+C2);
64 A.mut=mut_SI*.02088543; %convert to EE
65
66 mu_SI=C1*(A.T_inf*5/9)^1.5/(A.T_inf*5/9+C2);
67 A.mu_inf=mu_SI*.02088543; %convert to EE
68
69 A.at=sqrt(gamma*R_air*Tt1);
70 A.a_inf=sqrt(gamma*R_air*A.T_inf);
71 A.V_inf=A.Mach_inf*A.a_inf;
72
73 A.Re_inf=(A.rho_inf*A.V_inf)/A.mu_inf;
74
75 A.q_inf=0.5*A.rho_inf*A.V_inf^2;
76
77 end

```

## Appendix D: Rossiter Modes Code

```
1 % Function that calculates Rossiter modes using modified
  Rossiter equation
2 % from Heller and Bliss (allows improved accuracy at
  supersonic speeds).
3 % Includes logic to output error messages if required
  structure fields do
4 % not exist.
5 function [A]=Rossiter(A,modes,L)
6
7 %% Check to ensure required field exist
8 check_mach=isfield(A,'Mach_inf');
9 check_V=isfield(A,'V_inf');
10
11 %% Calculate Rossiter modes
12 if check_mach==1 && check_V==1
13     beta=.25;
14     kc=.57;
15     gamma=1.4;
16
17     for i=1:length(modes)
18         A.Str(i)=(modes(i)-beta)/(A.Mach_inf/sqrt(1+.5*(
19             gamma-1)*A.Mach_inf^2)+1/kc);
20         A.Rfreq(i)=A.Str(i)*A.V_inf/L;
21     end
22 elseif check_mach==0 && check_V==1
23     display('Mach_inf does not exist in input 1')
24 elseif check_mach==1 && check_V==0
25     display('V_inf does not exist in input 1')
26 else
27     display('Mach_inf and V_inf do not exist in input 1')
28 end
29 end
```

## Appendix E: Boundary Layer Code

```
1 % Calculates Nozzle BL thickness based on turbulent boundary
   layer theory
2
3 %% Input and Mach specific calculations
4 close all; clear all; clc
5 M_nom=input('Nominal Mach Number (no decimals i.e.
   15,19,23,3): ');
6 switch M_nom
7     case 15
8         tests=[1 2 3 5 6 7];
9         load M15.mat %from nozzle design code
10        h=min(M15.fcon);
11        ind=find(M15.fcon==h,1,'first');
12        xrange=linspace(0,14,length(M15.fcon));
13        x=xrange(ind);
14        fp=-2.5*M15.amp*M15.w*sin(M15.w*x); %first deriv
15        fpp=-2.5*M15.amp*M15.w^2*cos(M15.w*x); %second deriv
16        rho=abs(1+fp^2)^1.5/abs(fpp); %radius of curvature
17        R=rho/h;
18        g=0.195213; %from figure from Rogers and Davis
19     case 19
20         tests=[1 5 6 7 8];
21         load M19.mat
22         h=min(M19.fcon);
23         ind=find(M19.fcon==h,1,'first');
24         xrange=linspace(0,14,length(M19.fcon));
25         x=xrange(ind);
26         fp=-2.5*M19.amp*M19.w*sin(M19.w*x);
27         fpp=-2.5*M19.amp*M19.w^2*cos(M19.w*x);
28         rho=abs(1+fp^2)^1.5/abs(fpp);
29         R=rho/h;
30         g=0.228697;
31     case 23
32         tests=[1 2 3 4 5 6 8 9];
33         load M23.mat
34         h=min(M23.fcon);
35         ind=find(M23.fcon==h,1,'first');
36         xrange=linspace(0,14,length(M23.fcon));
37         x=xrange(ind);
38         fp=-2.5*M23.amp*M23.w*sin(M23.w*x);
39         fpp=-2.5*M23.amp*M23.w^2*cos(M23.w*x);
40         rho=abs(1+fp^2)^1.5/abs(fpp);
41         R=rho/h;
```

```

42         g=0.265212;
43     case {3,30} % no rho calc because contour not known
44         M_nom=3;
45         tests=[4 5 6 7];
46         g=0.3319;
47 end
48
49 basename=strcat('C:\Users\Justin\Documents\Thesis\Results\
    Straight Test Section\Mach',...
50     num2str(M_nom),'_straight_');
51 tstart=3.4; %determined through observation of pressure
    traces
52
53 for i=1:length(tests)
54     filepath=strcat(basename,num2str(tests(i)),'.lvm');
55     A=importdata(filepath,'\t',23);
56
57     A=Flow_Con(filepath,A,tstart);
58     % Method from Rogers and Davis / McCabe
59     Re_h=A.rhot*A.at*h/A.mut;
60
61     ds_th=0.026*h*(R^2/Re_h)^0.2;
62     d_th=ds_th/g;
63
64     dx=xrange(end)-x;
65     Re_x=A.rho_inf*A.V_inf*dx/A.mu_inf;
66
67     del_d=0.29*dx/(Re_x^.2);
68
69     A.d=d_th+del_d;
70
71     varname=strcat('T',num2str(i));
72     assignin('base',varname,A);
73 end

```

## Appendix F: Rossiter Mode Results

Table F.1: Comparison of Observed and Predicted Rossiter Modes for Mach 2.96

Test	Mode	Predicted (Hz)	Observed (Hz)	Difference (Hz)
1	2	1795.12	1926.24	131.12
	3	2820.91	2865.81	44.91
	4	3846.69	4013.38	166.70
	5	4872.48	5224.95	352.48
2	2	1791.07	2254.14	463.07
	3	2814.54	2965.08	150.54
	4	3838.01	4004.02	166.01
	5	4861.15	5258.96	397.48
3	2	1789.45	1818.89	29.45
	3	2811.99	2807.98	-4.01
	4	3834.53	3957.06	122.53
	5	4857.07	5202.14	345.07
4	2	1782.49	1780.99	-1.51
	3	2801.06	2770.12	-30.94
	4	3819.63	3943.25	123.63
	5	4838.19	5132.39	294.19

Table F.2: Comparison of Observed and Predicted Rossiter  
Modes for Mach 2.22

Test	Mode	Predicted (Hz)	Observed (Hz)	Difference (Hz)
2	1	721.50	627.01	-94.50
	2	1683.51	1575.01	-108.49
	3	2645.51	2579.02	-66.49
	4	3607.51	3557.03	-48.49
	5	4569.52	4651.03	81.52
	6	5531.52	5647.04	115.52
3	1	725.91	515.82	-210.09
	2	1693.79	1651.59	-42.21
	3	2661.68	2611.35	-50.32
	4	3629.56	3587.12	-42.44
	5	4597.44	4706.89	109.44
	6	5565.33	5674.65	109.33
4	1	722.54	517.08	-205.46
	2	1685.92	1595.85	-90.08
	3	2649.31	2578.62	-70.69
	4	3612.69	3569.39	-43.31
	5	4576.08	4624.16	48.08
	6	5539.46	5638.93	99.46

*Continued on next page*



Table F.2 – *Continued from previous page*

Test	Mode	Predicted (Hz)	Observed (Hz)	Difference (Hz)
5	1	727.50	543.01	-184.50
	2	1697.51	1683.01	-14.49
	3	2667.51	2607.02	-60.49
	4	3637.52	3643.03	5.52
	5	4607.52	4671.04	63.52
	6	5577.52	5755.05	177.52
6	1	728.78	521.55	-207.22
	2	1700.48	1696.96	-3.52
	3	2672.18	2664.36	-7.82
	4	3643.88	3631.77	-12.12
	5	4615.58	4783.17	167.58
	6	5587.29	5742.57	155.29
7	1	726.19	516.38	-209.81
	2	1694.45	1620.89	-73.55
	3	2662.70	2605.41	-57.30
	4	3630.96	3597.92	-33.04
	5	4599.21	4686.43	87.21
	6	5567.47	5670.94	103.47

Table F.3: Comparison of Observed and Predicted Rossiter Modes for Mach 1.84

Test	Mode	Predicted (Hz)	Observed (Hz)	Difference (Hz)
2	1	685.49	538.99	-146.51
	2	1599.49	1534.97	-64.51
	3	2513.48	2514.96	1.48
	4	3427.47	3374.94	-52.53
	5	4341.46	4402.93	61.46
	6	5255.46	5398.91	143.46
3	1	685.66	547.31	-138.34
	2	1599.87	1535.73	-64.13
	3	2514.08	2564.15	50.08
	4	3428.29	3376.57	-51.71
	5	4342.50	4396.99	54.50
	6	5256.70	5449.41	192.70
4	1	690.99	509.97	-181.01
	2	1612.30	1544.60	-67.70
	3	2533.61	2507.23	-26.39
	4	3454.93	3445.86	-9.07
	5	4376.24	4488.48	112.24
	6	5297.56	5459.11	161.56
5	1	691.50	527.01	-164.50
	2	1613.51	1595.01	-18.49
	3	2535.51	2607.02	71.51
	4	3457.51	3459.03	1.51
	5	4379.52	4455.03	75.52
	6	5301.52	5491.03	189.52

Table F.4: Comparison of Observed and Predicted Rossiter Modes for Mach 1.43

Test	Mode	Predicted (Hz)	Observed (Hz)	Difference (Hz)
1	1	673.44	538.88	-134.56
	2	1571.36	1518.73	-52.64
	3	2469.29	2250.57	-218.71
	4	3367.21	3246.42	-120.79
2	1	673.45	514.91	-158.55
	2	1571.39	1486.78	-84.61
	3	2469.33	2314.66	-154.67
	4	3367.27	3326.53	-40.73
3	1	658.09	484.17	-173.91
	2	1535.53	1423.07	-112.47
	3	2412.98	2185.96	-227.02
	4	3290.43	3124.86	-165.57

## **Appendix G: Detailed Drawings of Nozzle Blocks**

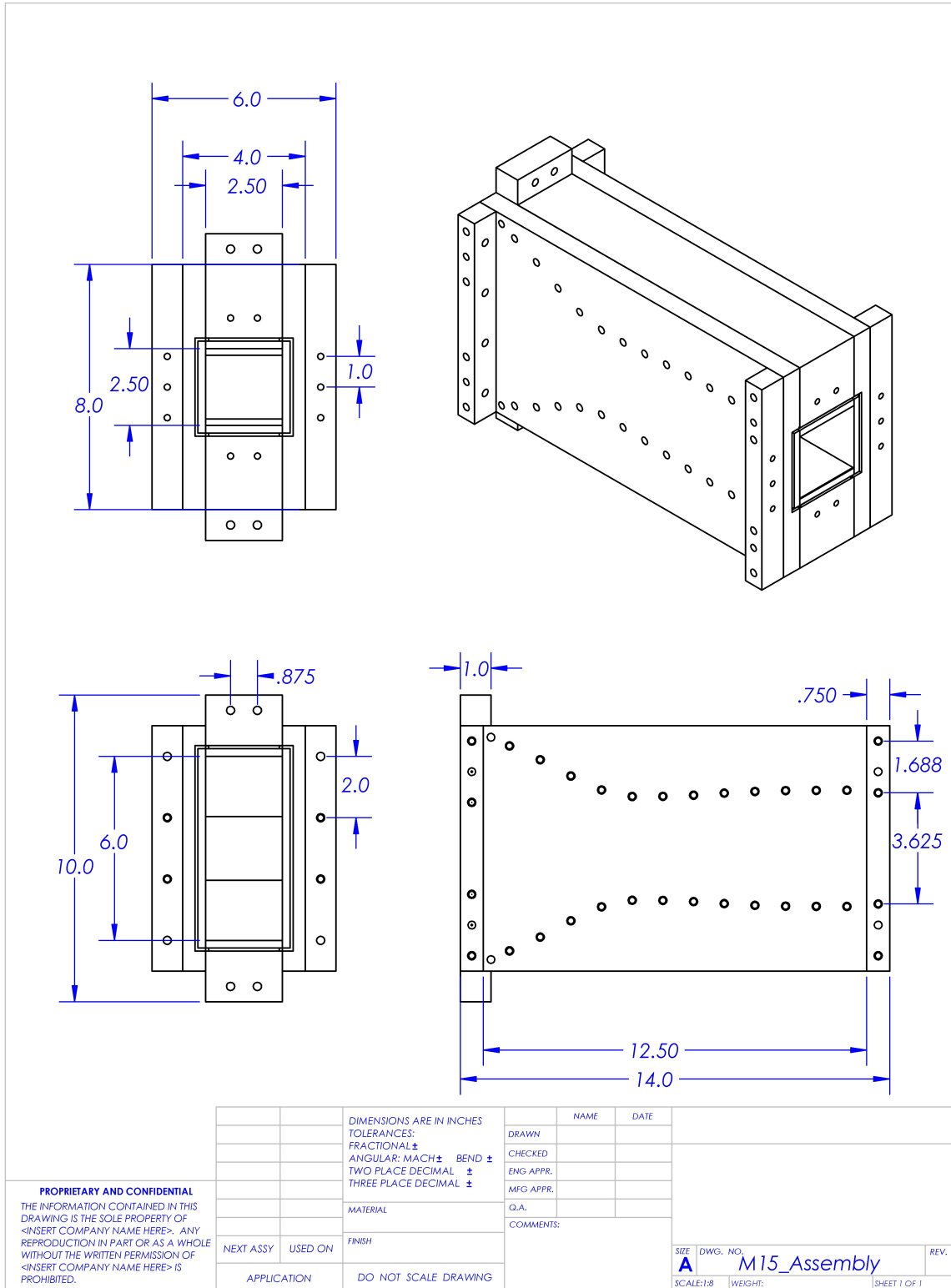


Figure G.1: Representative Drawing of Nozzle Block from Multiple Views (Mach 1.5)

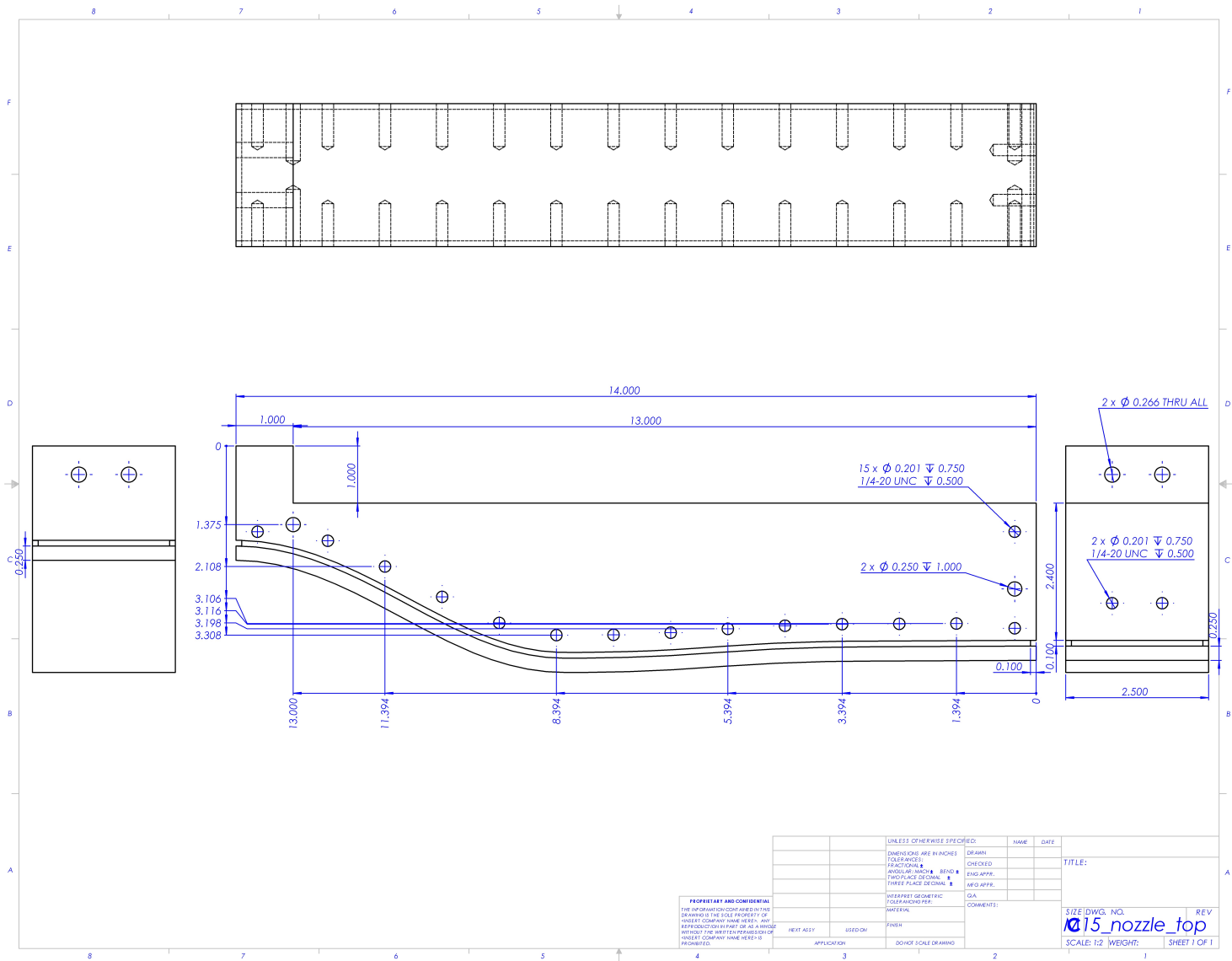


Figure G.2: Drawing of Mach 1.5 Nozzle Contour

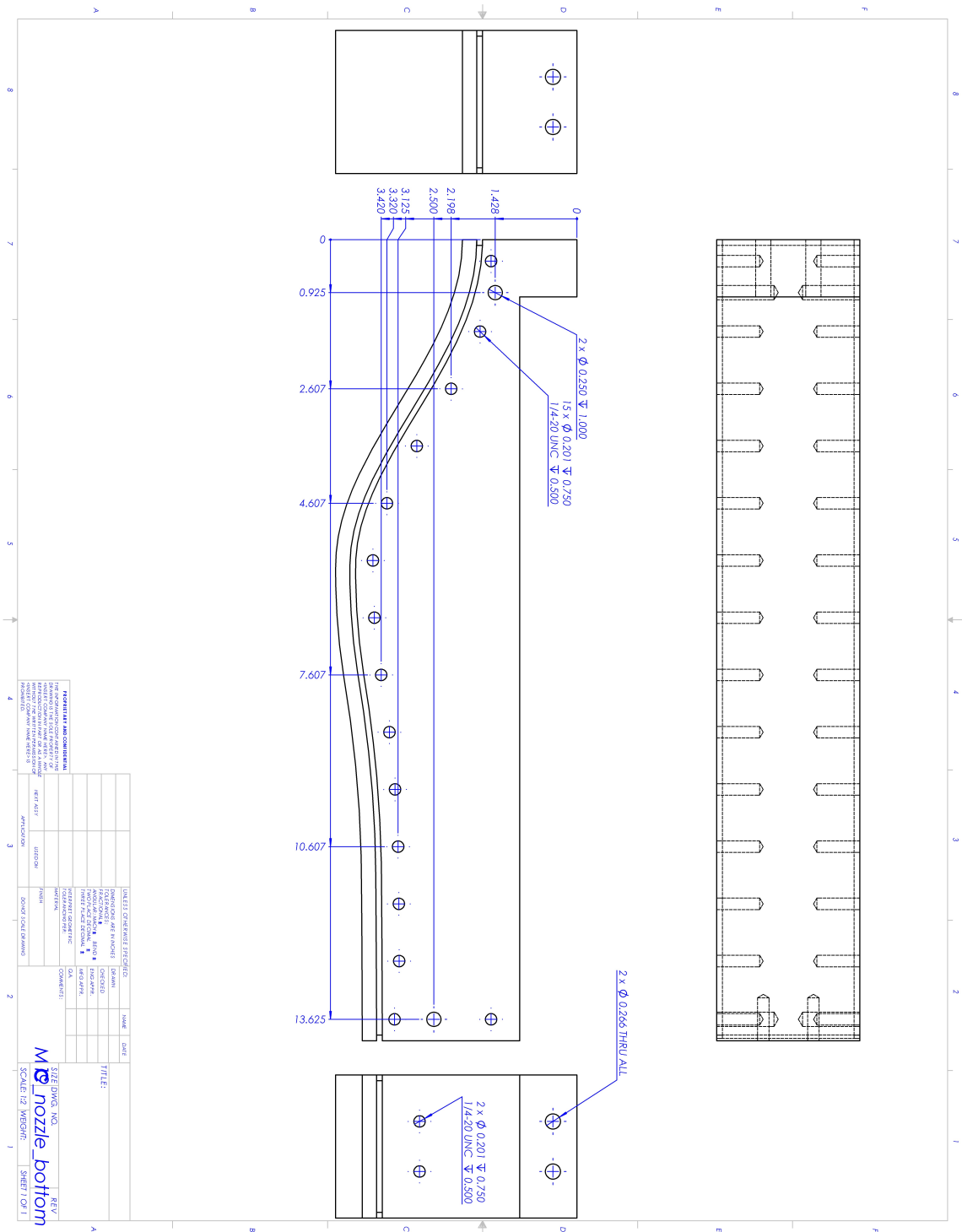


Figure G.3: Drawing of Mach 1.9 Nozzle Contour







## Appendix H: Trajectory Plotting Code

```
1 % Plots multiple trajectories without time stamps. Tuned for
   1.0 psia case.
2
3 close all; clear all; clc
4 check=exist('Mult_traj.mat','file');
5 if check~=0
6     load Mult_traj.mat
7 else
8     num_traj=input('Number of trajectories: ');
9     for i=1:num_traj
10         [files,path] = uigetfile('*','MultiSelect','on');
11         A=[];
12         if iscell(files)
13             ind_x=1;
14             ind_z=2;
15             ind_t=3;
16             for n = 1:length(files)
17                 data = importdata(fullfile(path,files{n}));
18                 % fullfile including path
19                 A(n,1:2)=data.data;
20                 time=sscanf(files{n},'%f_%f_m23.csv');
21                 tlen=length(sprintf('%f',abs(time)));
22                 if tlen==4||tlen==3
23                     A(n,ind_t)=time*0.3/2000;
24                 else
25                     A(n,ind_t)=time*3/2000;
26                 end
27             end
28         else
29             data = importdata(fullfile(path,files));
30             A=[A;data];
31             ind_x=find(A(1,2:4)==max(A(1,2:4)))+1;
32             ind_z=find(A(1,2:4)==min(A(1,2:4)))+1;
33             ind_y=find(A(1,2:4)==min(abs(A(1,2:4))))+1;
34             ind_t=1;
35             A(:,ind_z)=(A(:,ind_z)+4).*0.375;
36             A(:,ind_x)=(A(:,ind_x)-15).*0.375;
37             r=0.46875;
38             indc_x=find(A(:,ind_x)+r>=6.75,1,'first');
39             indc_z=find(A(:,ind_z)-r<=0,1,'first');
40             indc_y=find(abs(A(:,ind_y))+r>=0.75,1,'first');
```

```

41         if isempty(indc_x)==0 || isempty(indc_y)==0 ||
42            isempty(indc_z)==0
43             collision=[indc_x indc_y indc_z];
44             indt=find(collision==min(collision),1,'first');
45             A=A(1:collision(indt),:);
46         end
47         Vref=1826.72; %ft/s
48         Lref=0.03125; %ft/grid unit
49
50         A(:,1)=A(:,1)*Lref/Vref;
51         A(:,1)=A(:,1)-A(1,1);
52
53         ti=A(1,1);
54         tf=A(end,1);
55
56         A=[A(:,ind_x) A(:,ind_z) A(:,ind_t) A(:,ind_y)];
57
58     end
59     varname=strcat('T',num2str(i));
60     assignin('base',varname,A);
61 end
62 end
63
64 %% Objects
65 cav1=[-5.625:0.0375:0;1.5*ones(1,151)];
66 cav2=[0:.0375:6.75;zeros(1,181)];
67 cav3=[6.75:.0375:12.375;1.5*ones(1,151)];
68 cav=[cav1 cav2 cav3];
69 for i=1:length(num_traj)
70     varname=strcat('T',num2str(i));
71     assignin('base','A',eval(varname));
72
73     ymin1=[min(cav(2,:)) min(A(:,ind_z))];
74     ymin1=min(ymin1);
75     ymin2(i)=round(ymin1*4)/4-0.25;
76     ymax1=[max(cav(2,:)) max(A(:,ind_z))];
77     ymax1=max(ymax1);
78     ymax2(i)=round(ymax1*4)/4+0.25;
79
80 end
81
82 ymin=min(ymin2);
83 ymax=max(ymax2);
84

```

```

85 % r=0.46875;
86 % circ_x=-r:.001:r+0.001;
87 % circ_z=real(sqrt(r^2-(circ_x).^2));
88 % mcirc_z=-circ_z;
89 % circ_x=circ_x+A(end,ind_x);
90 % circ_z=circ_z+A(end,ind_z);
91 % mcirc_z=mcirc_z+A(end,ind_z);
92
93 %% Graph
94 scrsz=get(0,'ScreenSize');
95 figure('Position',[1 0 scrsz(3) 0.7*scrsz(4)])
96 set(gcf,'PaperPositionMode','auto')
97 hold on
98 plot(cav(1,:),cav(2,:),'-k','LineWidth',1.5)
99 plot(T1(:,ind_x),T1(:,ind_z),'-r','LineWidth',3.0)
100 plot(T2(:,ind_x),T2(:,ind_z),'-ob','LineWidth',1.5)
101 plot(T3(:,ind_x),T3(:,ind_z),'-g','MarkerSize',15,'
    LineWidth',1.5)
102 plot(T4(:,ind_x),T4(:,ind_z),'-*c','MarkerSize',7,'LineWidth
    ',1.5)
103 plot(T5(:,ind_x),T5(:,ind_z),'-dm','LineWidth',1.5)
104 plot(T6(:,ind_x),T6(:,ind_z),'-x','Color',[0.95 0.4 0],'
    MarkerSize',10,'LineWidth',1.5)
105 plot(T7(:,ind_x),T7(:,ind_z),'-+','Color',[.5 0 .9],'
    LineWidth',1.5)
106 plot(T8(:,ind_x),T8(:,ind_z),'->','Color',[0 0 .5],'
    LineWidth',1.5)
107 plot(T9(:,ind_x),T9(:,ind_z),'-<','Color',[0 .5 0],'
    LineWidth',1.5)
108 % for i=1:length(num_traj)
109 %     varname=strcat('T',num2str(i));
110 %     assignin('base','A',eval(varname));
111 %
112 %     plot(A(:,ind_x),A(:,ind_z),'-b')
113 % end
114 leg=legend('Cavity','Computational','P_t=1.45','P_t=1.12','
    P_t=1.05',...
115     'P_t=0.93','P_t=1.00','P_t=0.75','P_t=1.22','P_t=1.21'
    ,...
116     'Location',[0.1 0.5 0.1 0.1]);
117 set(leg,'FontSize',12);
118 set(gca,'ydir','reverse','Position',[0.048 0.004 0.942
    0.996])
119 xlim([-0.25 7.5])
120 ylim([ymin 2.25])
121 set(gca,'DataAspectRatio',[1 1 1],'YTick',-0.25:0.25:2.25)

```

```

122 grid on
123 xlabel('X Coordinate of Center of Mass','FontSize',12)
124 ylabel('Z Coordinate of Center of Mass','FontSize',12)
125
126 %% Save
127 save_graph=input('Save graph to file? (y/n) ','s');
128 if save_graph=='y'
129     shortname=strcat('M23_',num2str(num_traj),'_multitraj');
130     printdir='C:\Users\Justin\Documents\Thesis\My thesis\
        Figures';
131     printto=sprintf('%s\\%s.png',printdir,shortname);
132     print('-dpng',printto)
133     close all
134 end

```

## Appendix I: Heavy Mach Scaling Codes

### I.1 Drop\_analysis.m

```
1 % Analyzes drop test data from wind tunnel data. Computes
   flow conditions ,
2 % applies Heavy Mach Scaling , and averages scaled quantities
3
4 %% Input Data
5 close all; clear all; clc
6 M_nom=input('Nominal Mach Number (no decimals i.e.
   15,19,23,3): ');
7 switch M_nom
8     case 15
9         print('No data currently available for Mach 1.5')
10    case 19
11        print('No data currently available for Mach 1.9')
12    case 23
13        tests=[5 6]; %[3 5 6 7 9 11];
14        tests1=[13 15 18 19 22 23 24 25]; %[13 15:20 21
           22:24 25];
15    case {3,30}
16        print('See research of Flora for Mach 3.0 results')
17 end
18
19 % Filename form of Mach##_sphere_#.lvm (e.g. Mach23_sphere_7
   .lvm)
20 basename=strcat('C:\Users\Justin\Documents\Thesis\Results\
   Drop Tests\Mach',...
21     num2str(M_nom),'_sphere_');
22 tstart=3.5; %Determined from pressure traces , increased
   because of low pt
23
24 for i=1:length(tests)
25     filepath=strcat(basename,num2str(tests(i)),'.lvm');
26     A=importdata(filepath,'\t',23);
27
28     A=Flow_Con(filepath,A,tstart);
29
30     varname=strcat('T',num2str(i));
31     assignin('base',varname,A);
32
33 end
34
```

```

35 tstart1=3.8; %Determined from pressure traces , increased
    because of low pt
36 for i=1:length(tests1)
37     filepath=strcat(basename,num2str(tests1(i)),'.lvm');
38     A=importdata(filepath,'\t',23);
39
40     A=Flow_Con(filepath,A,tstart1);
41
42     varname=strcat('T',num2str(i+length(tests)));
43     assignin('base',varname,A);
44 end
45 %% Apply Scaling Laws
46 height=input('Altitude to scale to (ft): ');
47 lamda=input('Scaling Factor: ');
48 [T_scale,w,w,w,rho_scale,w,w,w]=ATMOS(height);
49 for i=1:(length(tests)+length(tests1))
50     varname=strcat('T',num2str(i));
51     assignin('base','A',eval(varname));
52
53     A=mass(A);
54     S=HMS(A,lamda,rho_scale,T_scale);
55
56     varname=strcat('T',num2str(i));
57     assignin('base',varname,A);
58     svarname=strcat('S',num2str(i));
59     assignin('base',svarname,S);
60 end
61
62 %% Average Scaled Quantities
63 Wt=[];
64 density=[];
65 qrat=[];
66 for i=1:(length(tests))
67     varname=strcat('S',num2str(i));
68     assignin('base','A',eval(varname));
69     Wt=[Wt; A.weight];
70     density=[density; A.denslb];
71     qrat=[qrat; A.qrat];
72 end
73 Wt_av=mean(Wt);
74 dens_av=mean(density);
75 qrat_av=mean(qrat);
76
77 Wt1=[];
78 density1=[];
79 qrat1=[];

```

```

80 for i=length(tests)+1:(length(tests)+length(tests1))
81     varname=strcat('S',num2str(i));
82     assignin('base','A',eval(varname));
83     Wt1=[Wt1; A.weight];
84     density1=[density1; A.denslb];
85     qrat1=[qrat1; A.qrat];
86 end
87 Wt_av1=mean(Wt1);
88 dens_av1=mean(density1);
89 qrat_av1=mean(qrat1);
90
91 %% print
92 for i=1:(length(tests)+length(tests1))
93     varname=strcat('S',num2str(i));
94     assignin('base','A',eval(varname));
95     fprintf('%1.3f & %3.1f & %3.1f & \\\n',A.qrat,A.
        weight,A.denslb)
96 end

```

## I.2 mass.m

```

1 % Function that determines mass and MOI based on filename
  % and number. Mass
2 % is a callout table determined from spreadsheet data about
  % model mass.
3
4 function [A]=mass(A)
5
6 test_num=sscanf(A.filename, '%*4s%*2f_sphere_%f.lvm');
7
8 m=[1:1:25;
9     7.575 7.6 7.36 7.181 ...
10    6.435 6.558 6.928 6.759 6.908 ...
11    6.667 6.667 6.679 6.581 6.649 6.869 ...
12    6.758 6.732 6.727 6.786 6.737 ...
13    6.695 6.684 6.714 6.654 6.617];
14 m(2,:)=m(2,:)*0.00220462262./32.17; %convert to slugs from
    grams
15 ind=find(m(1,:)==test_num,1,'first');
16
17 A.m=m(2,ind);
18
19 A.radius=15/16/2/12; % diameter to radius to feet (from in)
20
21 A.I=0.4*A.m*A.radius^2;

```

## I.3 ATMOS.m



```

1 %
  *****

2 %
3 % ATMOS.m
4 %
5 % Sub-routine that , when given an altitude , calculates the
  standard day
6 % conditions at that altitude using temperature , pressure ,
  and density
7 % ratios combined with sea level standard day conditions
8 %
9 % Author: C3C Justin Merrick , 18 Nov 09
10 %
11 % Input Variables:
12 %     h      = height above sea level (ft)
13 %
14 % Output Variables:
15 %     T      = Temperature (deg R)
16 %     theta  = Temperature Ratio
17 %     P      = Pressure (lbs/ft^2)
18 %     delta  = Pressure Ratio
19 %     rho    = Density (slugs/ft^3)
20 %     sigma  = Density Ratio
21 %     mu     = Coefficient of Viscosity (lb*sec)
22 %     a      = Speed of Sound (ft/s)
23 %
24 % Constants:
25 %     gamma  = 1.4 , characteristic of air
26 %     R      = 1716, gas constant for air ((ft*lb)/(slug*
  deg R))
27 %
28 % References:
29 %     ATMOS handout detailing equations to be used
30 %     MATLAB Fundamentals booklet to learn how to use loops
  , especially
31 %     elseif statements , and to detail fprintf commands
32 %
33 % Documentation:
34 %     C3C Phillips provided possible problem solutions when
  I was running
35 %     into calculation errors. C3C Gormley and I
  collaborated on how best
36 %     to input the failure conditions and what type of
  loops to use.

```

```

37 %
    ****

38 function [T,theta ,P, delta ,rho ,sigma ,a ,mu]=ATMOS(h)
    % Make ATMOS a function of input var. h
39 if h<=36089
    % Create theta ,delta loop
40     theta=1-6.875*10^(-6)*h;
        % theta calculation
41     delta=(1-6.875*10^(-6)*h)^(5.2561);
        % delta calculation
42 elseif 36089<h
    % Apply high altitude case
43     theta=.75189;
        % High altitude theta calculation
44     delta=.2234*exp(4.806e-5*(36089-h));
        % High altitude delta calculation
45 end
    % Close theta ,delta loop
46 sigma=delta / theta ;
    % Calculate sigma
47 T=theta *518.7;
    % Calculate T, 518.7 @ SL
48 P=delta *2116.8;
    % Calculate P, 2116.8 @ SL
49 rho=sigma*.002377;
    % Calculate rho, .002377 @ SL
50 mu=3.737e-7+5.967366e-10*(T-518.7);
    % Calculate mu
51 a=sqrt(1.4*1716*T);
    % Calculate a

```

#### I.4 HMS.m

```

1 % Function that calculates full-scale quantities based on
    model quantities
2 % using Heavy Mach Scaling
3
4 function [S]=HMS(A, lamda ,rho ,T)
5 S.filename=A.filename;
6 S.T_inf=T;
7 S.rho_inf=rho;
8 S.V_inf=A.V_inf*sqrt(T/A.T_inf);
9
10 S.q_inf=0.5*rho*S.V_inf^2;
11
12 S.qrat=A.q_inf/S.q_inf;

```

```

13
14 S.m=A.m*S.q_inf/A.q_inf/lamda^2;
15 S.I=A.I*S.q_inf/A.q_inf/lamda^4;
16
17 S.Mach_inf=A.Mach_inf;
18
19 S.weight=S.m*32.17;
20 Vol=4/3*pi*(A.radius/lamda)^3;
21
22 S.density=S.m/Vol;
23 S.denslb=S.weight/Vol;

```

## Appendix J: Cavity Analysis Code

```

1 % Analyzes FFT data and pressure data to produce spectra and
  Rossiter mode
2 % calculations/differences
3
4 %% Import data
5 close all; clear all; clc
6
7 M_nom=input('Nominal Mach Number (no decimals i.e.
  15,19,23,3): ');
8 save_var=input('Save pics? (y/n): ','s');
9 switch M_nom %Selection of tests based on test index
10     case 15
11         tests=[1 2 3];
12     case 19
13         tests=[2 3 4 5];
14     case 23
15         tests=[2 3 4 5 6 7];
16     case {3,30}
17         tests=[1 2 3 4];
18 end
19 % Filename in form of M##_cavity_FFT_#.lvm (e.g.
  M19_cavity_FFT_1.lvm)
20 basename_fft=strcat('C:\Users\Justin\Documents\Thesis\
  Results\Cavity\M',...
21     num2str(M_nom),'_cavity_FFT_');
22 % Filename in form of Mach##_cavity_#.lvm (e.g. M23_cavity_4
  .lvm)
23 basename=strcat('C:\Users\Justin\Documents\Thesis\Results\
  Cavity\Mach',...
24     num2str(M_nom),'_cavity_');
25 tstart=3.4; %Determined from observation of pressure traces
26
27 for i=1:length(tests)
28     spec=importdata(strcat(basename_fft,num2str(tests(i)),'.
  lvm'),'t',22);
29     filepath=strcat(basename,num2str(tests(i)),'.lvm');
30     A=importdata(filepath,'t',23);
31
32     A=Flow_Con(filepath,A,tstart);
33
34     p_spec=1.5741^2.*spec.data(:,2).^2; %Convert FFT data
  from V_rms to P
35     ind=find(spec.data(:,3)==200,1,'first');
```

```

36     A.spec=[p_spec(ind:end) spec.data(ind:end,3)];
37
38     varname=strcat('R',num2str(i));
39     assignin('base',varname,A);
40
41 end
42 clear A ind spec p_spec
43 %% Calculate SPL
44 for i=1:length(tests)
45     varname=strcat('R',num2str(i));
46     assignin('base','A',eval(varname));
47
48     %p_ref as limit of human hearing (psi)
49     prat=A.spec(:,1)./2.90075475e-9^2;
50     A.spl=10.*log10(prat);
51
52     modes=1:1:6;
53     A=Rossiter(A,modes,6.75/12);
54
55     assignin('base',varname,A);
56 end
57
58 %% Graph
59 figure
60 switch M_nom
61     case 15
62         plot(R1.spec(:,2),R1.spl,R2.spec(:,2),R2.spl,R3.spec
63             (:,2),R3.spl)
64         legend(strcat('P_{stag}=',num2str(R1.pt)),strcat('P_
65             {stag}=',num2str(R2.pt)),...
66             strcat('P_{stag}=',num2str(R3.pt)))
67     case 19
68         plot(R1.spec(:,2),R1.spl,R2.spec(:,2),R2.spl,R3.spec
69             (:,2),R3.spl,R4.spec(:,2),R4.spl)
70         legend(strcat('P_{stag}=',num2str(R1.pt)),strcat('P_
71             {stag}=',num2str(R2.pt)),...
72             strcat('P_{stag}=',num2str(R3.pt)),strcat('P_{
73             stag}=',num2str(R4.pt)))
74     case 23
75         plot(R1.spec(:,2),R1.spl,R2.spec(:,2),R2.spl,R3.spec
76             (:,2),R3.spl,R4.spec(:,2),R4.spl,...
77             R5.spec(:,2),R5.spl,R6.spec(:,2),R6.spl)
78         legend(strcat('P_{stag}=',num2str(R1.pt)),strcat('P_
79             {stag}=',num2str(R2.pt)),...
80             strcat('P_{stag}=',num2str(R3.pt)),strcat('P_{
81             stag}=',num2str(R4.pt)),...

```

```

74         strcat('P_{stag}= ', num2str(R5.pt)), strcat('P_{
           stag}= ', num2str(R6.pt)))
75     case {3,30}
76         plot(R1.spec(:,2), R1.spl, R2.spec(:,2), R2.spl, R3.spec
           (:,2), R3.spl, R4.spec(:,2), R4.spl)
77         legend(strcat('P_{stag}= ', num2str(R1.pt)), strcat('P_
           {stag}= ', num2str(R2.pt)), ...
78         strcat('P_{stag}= ', num2str(R3.pt)), strcat('P_{
           stag}= ', num2str(R4.pt)))
79     end
80     xlim([200 6400])
81     ylim([100 150])
82     % ylim([100 130]) % Mach 3
83     xlabel('Frequency (Hz)')
84     ylabel('SPL (dB)')
85     grid on
86
87     for i=1:length(tests)
88         varname=strcat('R', num2str(i));
89         assignin('base', 'A', eval(varname));
90
91         figure
92         hold on
93         set(gca, 'FontSize', 18, 'LineWidth', 2, 'YGrid', 'on')
94         plot(A.spec(:,2), A.spl, 'LineWidth', 2)
95         xlim([200 6400])
96         ylim([100 150])
97         % ylim([100 130]) % Mach 3
98         xlabel('Frequency (Hz)')
99         ylabel('SPL (dB)')
100        for j=1:length(A.Rfreq)
101            plot([A.Rfreq(j) A.Rfreq(j)], [100 150], '-k', '
                LineWidth', 2)
102        end
103        legend('Spectrum', 'Rossiter Modes', 'Location', 'Southwest
            ')
104        if save_var=='y'
105            saveas(gcf, strcat('m15_cavity', num2str(i), '.png'))
106        end
107    end
108
109    %% Rossiter Error
110    for i=1:length(tests)
111        varname=strcat('R', num2str(i));
112        assignin('base', 'A', eval(varname));
113

```

```

114     [pks,ind]=findpeaks(A.spl,'minpeakdistance',95,'npeaks',
        length(modes));
115     %Might need to change 3rd argument (95) to improve
        recognition of
116     %peaks, check by hand
117
118     for j=1:length(modes)
119         A.Rerr(j)=A.Rfreq(j)-A.spec(ind(j),2);
120     end
121     A.Rea=mean(A.Rerr);
122     A.Res=std(abs(A.Rerr));
123
124     varname=strcat('R',num2str(i));
125     assignin('base',varname,A);
126 end
127 for i=1:length(modes)
128     Tot_Rerr_avg(i)=0;
129     Rfreq_avg(i)=0;
130     for j=1:length(tests)
131         varname=strcat('R',num2str(j));
132         assignin('base','A',eval(varname));
133
134         Tot_Rerr_avg(i)=Tot_Rerr_avg(i)+A.Rerr(i);
135         Rfreq_avg(i)=Rfreq_avg(i)+A.Rfreq(i);
136     end
137 end
138 Tot_Rerr_avg=Tot_Rerr_avg./length(tests);
139 Rfreq_avg=Rfreq_avg./length(tests);
140 Percent_Rerr=Tot_Rerr_avg./Rfreq_avg.*100;

```

## Bibliography

- [1] Flora, T. J., *Freedrop Testing and CFD Simulation of Ice Models from a Cavity into Supersonic Flow*, Master's thesis, U.S. Air Force Institute of Technology, September 2012.
- [2] Rogers, E. and Davis, B., "A Note of Turbulent Boundary Layer Allowances in Supersonic Nozzle Design," Tech. Rep. C.P. No. 333, Ministry of Supply, 1957.
- [3] Hardy, R., Neumann, F., and Ruzicka, D., "Fighter aircraft," June 10 1997, US Patent 5,636,813.
- [4] Rockwell, D. and Naudascher, E., "Review - Self-Sustaining Oscillations of Flow Past Cavities," *Transactions of the ASME*, Vol. 100, 1978, pp. 152–165.
- [5] Zhang, J., Morishita, E., Okunuki, T., and Itoh, H., "Experimental and Computational Investigation of Supersonic Cavity Flows," *10th International Space Planes and Hypersonic Systems and Technologies Conference*, AIAA 2001-1755, 2001.
- [6] Cattafesta, L., Williams, D., Rowley, C., and Alvi, F., "Review of Active Control of Flow-Induced Cavity Resonance," *33rd AIAA Fluid Dynamics Conference*, AIAA 2003-3567, 2003.
- [7] Heller, H. H., Holmes, G., and Covert, E. E., "Flow-Induced Pressure Oscillations in Shallow Cavities," Tech. Rep. TR AD880496, Air Force Flight Dynamics Laboratory, 1970.
- [8] Dix, R. and Bauer, R., "Engineering Model Predictions of Aeroacoustic Amplitudes in a Weapons Cavity," *31st AIAA Aerospace Sciences Meeting*, AIAA-93-0858, 1993.
- [9] Deslandes, R. M. and Donauer, S., "Scaled-Drop-Tests: WYSIWYG or not?" *48th AIAA Aerospace Sciences Meeting*, AIAA 2010-681, 2010.
- [10] Marshall, J. C., *Analytical Evaluation of the Limitations of the Various Scaling Laws for Freedrop Store Separation Testing*, ARO, Inc. AEDC Division.
- [11] Johnson, R. A., Stanek, M. J., and Grove, J. E., "Store Separation Trajectory Deviations Due to Unsteady Weapons Bay Aerodynamics," *46th AIAA Aerospace Sciences Meeting*, AIAA 2008-188, 2008.
- [12] Coley, C. J. and Lofthouse, A. J., "Correlation of Weapon Bay Resonance and Store Unsteady Force and Moment Loading," *50th AIAA Aerospace Sciences Meeting*, AIAA 2012-0415, 2012.



- [13] Cenko, A., Deslandes, R., Dillenius, M., and Stanek, M., “Unsteady Weapon Bay Aerodynamics - Urban Legend of Flight Clearance Nightmare,” *46th AIAA Aerospace Sciences Meeting*, AIAA 2008-189, 2008.
- [14] Blazek, J., *Computational Fluid Dynamics: Principles and Applications*, Elsevier, 2005.
- [15] Nichols, R. H. and Westmoreland, S., “Comparison of Computational Dynamics Approaches for Simulating Weapons Bay Flows,” *Journal of Aircraft*, Vol. 44, No. 3, 2007, pp. 1019–1024.
- [16] Nichols, R. H., “A Comparison of Hybrid RANS/LES Turbulence Models for a Generic Weapons Bay With and Without a Spoiler,” *26th AIAA Applied Aerodynamics Conference*, AIAA 2008-6229, 2008.
- [17] Rizzetta, D. P. and Visbal, M. R., “Large-Eddy Simulation of Supersonic Cavity Flowfields Including Flow Control,” *AIAA Journal*, Vol. 41, No. 8, August 2003, pp. 1452–1462.
- [18] Rokita, T. and Arieli, R., “Different Approaches for Simulating the Flow inside and near a Weapons Bay,” *30th AIAA Applied Aerodynamics Conference*, 2012-3339, 2012.
- [19] Meakin, R., *Handbook of Grid Generation*, chap. 11, CRC Press, 2005.
- [20] Kim, N. and Chan, W. M., “Automation of Hole-Cutting for Overset Grids Using the X-rays Approach,” M/s 258-2, NASA Ames Research Center.
- [21] Nichols, R. H. and Buning, P. G., *User’s Manual for OVERFLOW 2.1*, NASA, 2nd ed., August 2008.
- [22] Kraft, N. D., “Non-Repeatability of Store Separation Trajectories from Internal Weapon Bays due to Unsteady Cavity Flow effects - Lessons Learned from a 2D Investigation,” *49th AIAA Aerospace Sciences Meeting*, AIAA 2011-1238, 2011.
- [23] Pope, S. B., *Turbulent Flows*, Cambridge University Press, 2000.
- [24] Ferri, A., “Application of the Method of Characteristics to Supersonic Rotational Flow,” Tech. Rep. ADB23344, NASA Langley Research Center, 1946.
- [25] Crown, J. C. and Heybey, W. H., “Supersonic Nozzle Design,” Nol memorandum 10594, Naval Ordnance Laboratory, apr 1950.
- [26] McCabe, A., “Design of a Supersonic Nozzle,” Tech. Rep. Reports and Memoranda No. 3440, Ministry of Aviation, 1967.
- [27] Anderson, J. D., *Modern Compressible Flow: With Historical Perspective*, McGraw-Hill, 2003.

- [28] Kageyama, A. and Sato, T., “The ‘Yin-Yang Grid’: An Overset Grid in Spherical Geometry,” *Geochem. Geophys. Geosyst.*, 5(Q09005), 2004.
- [29] Bjorge, S. T., Reeder, M. F., Subramanian, C., Crafton, J., and Fonov, S., “Flow Around an Object Projected from a Cavity into a Supersonic Freestream,” *AIAA Journal*, Vol. 43, No. 7, 2005, pp. 1465–1475.

REPORT DOCUMENTATION PAGE					Form Approved OMB No. 0704-0188	
<p>The public reporting burden for this collection of information is estimated to average 1 hour per response, including the time for reviewing instructions, searching existing data sources, gathering and maintaining the data needed, and completing and reviewing the collection of information. Send comments regarding this burden estimate or any other aspect of this collection of information, including suggestions for reducing this burden to Department of Defense, Washington Headquarters Services, Directorate for Information Operations and Reports (0704-0188), 1215 Jefferson Davis Highway, Suite 1204, Arlington, VA 22202-4302. Respondents should be aware that notwithstanding any other provision of law, no person shall be subject to any penalty for failing to comply with a collection of information if it does not display a currently valid OMB control number. PLEASE DO NOT RETURN YOUR FORM TO THE ABOVE ADDRESS.</p>						
1. REPORT DATE (DD-MM-YYYY)		2. REPORT TYPE		3. DATES COVERED (From — To)		
27-03-2014		Master's Thesis		Oct 2012-Mar 2014		
4. TITLE AND SUBTITLE  Influence of Mach Number and Dynamic Pressure on Cavity Tones and Freedrop Trajectories				5a. CONTRACT NUMBER		
				5b. GRANT NUMBER		
				5c. PROGRAM ELEMENT NUMBER		
6. AUTHOR(S)  Merrick, Justin D., Second Lieutenant, USAF				5d. PROJECT NUMBER  12Y128		
				5e. TASK NUMBER		
				5f. WORK UNIT NUMBER		
7. PERFORMING ORGANIZATION NAME(S) AND ADDRESS(ES) Air Force Institute of Technology Graduate School of Engineering and Management (AFIT/EN) 2950 Hobson Way WPAFB, OH 45433-7765				8. PERFORMING ORGANIZATION REPORT NUMBER  AFIT-ENY-14-M-36		
9. SPONSORING / MONITORING AGENCY NAME(S) AND ADDRESS(ES) AFRL/RQVI 2145 5th St WPAFB, OH 45433 POC: Mr. Rudy Johnson (937) 255 3037, rudy.johnson@wpafb.af.mil				10. SPONSOR/MONITOR'S ACRONYM(S)  AFRL/RQVI		
				11. SPONSOR/MONITOR'S REPORT NUMBER(S)		
12. DISTRIBUTION / AVAILABILITY STATEMENT DISTRIBUTION STATEMENT A: APPROVED FOR PUBLIC RELEASE; DISTRIBUTION UNLIMITED						
13. SUPPLEMENTARY NOTES This work is declared a work of the U.S. Government and is not subject to copyright protection in the United States.						
14. ABSTRACT Weapons release at supersonic speeds from an internal weapons bay is a highly desirable capability. To ensure a successful release at multiple Mach numbers, the aerodynamic environment must be well-understood and repeatable, with a robust system for safe testing of store separation. For this reason, experimental methods were used to investigate the characteristics of a scaled WICS bay with a length-to-depth ratio of 4.5 at multiple Mach numbers and stagnation pressures. Three new nozzles were designed, manufactured, and characterized for the AFIT small supersonic tunnel, yielding freestream Mach numbers of 2.22, 1.84, and 1.43. In addition, a control valve was reconfigured to achieve stagnation pressures as low as 1.0 psia. These nozzles were then used in conjunction with piezoresistive pressure transducers and high-speed Schlieren photography to capture the time-varying pressure signal and spectra of the cavity. Resonant frequencies from these tests matched very well with analytically predicted results for the Mach 2.3 and Mach 1.9 nozzles. The Mach 1.5 nozzle posed some difficulties for the configuration tested due to shocks reflecting into the cavity. The Mach 2.3 nozzle was utilized in freedrop testing of a 1:20 scaled sphere and compared to computational simulations. The computational solution was obtained using the OVERFLOW solver with incorporated 6DOF motion and the DDES/SST hybrid turbulence model. Analysis of the Schlieren video generated by the experimental tests allowed direct comparison of computational and experimental trajectories. Measured trajectories compared closely to computational trajectories, especially for the lowest stagnation pressure settings, where heavy Mach scaling yielded operationally relevant results, despite the small scale of the tests.						
15. SUBJECT TERMS Store Separation, Cavity Flow, Freedrop Testing, CFD, Rossiter Modes, Frequency Analysis, Dynamic Scaling, Nozzle Design						
16. SECURITY CLASSIFICATION OF:			17. LIMITATION OF ABSTRACT	18. NUMBER OF PAGES	19a. NAME OF RESPONSIBLE PERSON	
a. REPORT	b. ABSTRACT	c. THIS PAGE			Dr. Mark F. Reeder (ENY)	
U	U	U	UU	159	19b. TELEPHONE NUMBER (include area code) (937) 255-3636 x4530 Mark.Reeder@afit.edu	